



January 2016

# Integration Of Multispectral Camera Systems For Enhanced Visualization Biological Studies Using UAS

Subin Shahukhal

Follow this and additional works at: <https://commons.und.edu/theses>

---

## Recommended Citation

Shahukhal, Subin, "Integration Of Multispectral Camera Systems For Enhanced Visualization Biological Studies Using UAS" (2016). *Theses and Dissertations*. 1961.  
<https://commons.und.edu/theses/1961>

This Thesis is brought to you for free and open access by the Theses, Dissertations, and Senior Projects at UND Scholarly Commons. It has been accepted for inclusion in Theses and Dissertations by an authorized administrator of UND Scholarly Commons. For more information, please contact [zeinebyousif@library.und.edu](mailto:zeinebyousif@library.und.edu).

INTEGRATION OF MULTISPECTRAL CAMERA SYSTEMS FOR  
ENHANCED VISUALIZATION BIOLOGICAL STUDIES USING UAS

By

Subin Shahukhal

Bachelor of Science, North Dakota State University, 2012

A Thesis

Submitted to the Graduate Faculty

of the

University of North Dakota

in partial fulfillment of the requirements

for the degree of

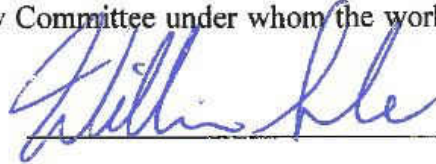
Master of Science

Grand Forks, North Dakota

May

2016

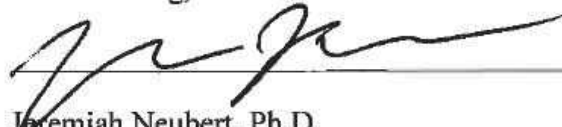
This thesis, submitted by Subin Shahukhal in partial fulfillment for the requirements for the Degree of Master of Science from the University of North Dakota, has been read by the Faculty Advisory Committee under whom the work has been done and is hereby approved.



William Semke, Ph.D.

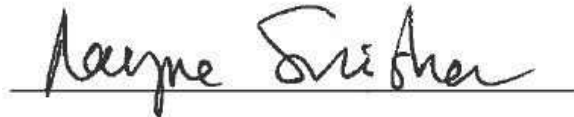


Clement Tang, Ph.D.



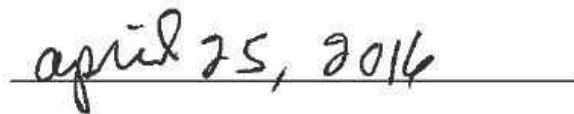
Jeremiah Neubert, Ph.D.

This thesis is being submitted by the appointed advisory committee as having met all of the requirements of the School of Graduate Studies at the University of North Dakota and is hereby approved.



Dr. Wayne Swisher

Dean of the School of Graduate Studies



Date

## PERMISSION

Title            Integration of Multispectral Camera Systems for Enhanced Visualization  
                    Biological Studies using UAS

Department    Mechanical Engineering

Degree         Master of Science

In presenting this thesis in partial fulfillment of the requirements for a graduate degree from the University Of North Dakota, I agree that the library of this University shall make it freely available for inspection. I further agree that permission for extensive copying for scholarly purposes may be granted by the professor who supervised my thesis work or, in his absence, by the Chairperson of the department or the dean of the School of Graduate Studies. It is understood that any copying or publication or other use of this thesis or part thereof for financial gain shall not be allowed without my written permission. It is also understood that due recognition shall be given to me and to the University of North Dakota in any scholarly use which may be made of any material in my thesis.

Name: Subin Shahukhal

Date: May 5, 2016

## TABLE OF CONTENTS

LIST OF FIGURES .....	vi
LIST OF TABLES .....	xi
ACKNOWLEDGEMENTS .....	xii
ABSTRACT .....	xiii
CHAPTER	
I. INTRODUCTION .....	1
II. SYSTEM DESCRIPTION .....	11
Payload .....	11
Tetracam ADC Lite Multispectral Camera .....	13
FLIR Photon 320 Infrared Camera .....	14
Odroid-U3 Single Board Computer .....	15
Sabrent USB-AVCPT 2.0 Video/Audio Capture & Converter .....	16
Lithium Ion Batteries .....	16
DC-DC Step Down Voltage Converter .....	17
III. SYSTEM PERFORMANCE CAPABILITIES .....	19
Resolution .....	19
Object Size Detection .....	22
Power Budget and Flight Time .....	23
IV. CAMERA ALIGNMENT .....	26
Mounting Plate Deflection Analysis .....	27
Mechanical Alignment .....	32
Target Board .....	33
Tuning Method .....	34
Image Registration .....	37

Affine Transformation and Image Warping .....	38
Camera Calibration .....	43
Tetracam ADC Lite Calibration.....	47
FLIR Photon 320 Infrared Camera Calibration .....	50
Straight Line Test for Undistorted Flir Photon 320 Image .....	56
V. SYSTEM INTEGRATION AND DATA COLLECTION.....	60
System Integration .....	60
Camera Capture Test.....	66
Data Collection .....	68
Tetracam Spectral Calibration Image .....	69
Continuous Capture Configuration .....	70
Payload Operation Set up.....	72
Data Retrieval .....	72
VI. POST PROCESSING .....	73
Raw Image Processing.....	73
Spectral Image Analysis .....	74
Normalized Difference Vegetation Index (NDVI) .....	75
Spectral False Color Combinations .....	79
Normalized Difference Ratio of Image bands .....	81
Registration of Infrared Image on NDVI.....	83
VII. RESULTS & DISCUSSION .....	85
VIII. CONCLUSIONS & RECOMMENDATIONS.....	107
APPENDICES .....	111
Appendix A.....	112
Appendix B .....	119
Appendix C .....	121
Appendix D.....	126
REFERENCES .....	130

## LIST OF FIGURES

Figure	Page
1. Relation of canopy temperature with NDVI and PRI [19]. .....	4
2. Spatially co-registered image showing moss health and temperature [21].....	5
3. Stacking of several layers of spectral images for each pixel showing sampled spectral information for soil water and vegetation [29]. .....	9
4. Spectral signature of the healthy and unhealthy vegetation [32].....	10
5. Schematics of a Payload System.....	12
6. Standalone UAS payload for the integrated multispectral imaging system .....	12
7. Tetracam ADC Lite multispectral camera [22] .....	13
8. FLIR Photon 320 infrared camera [23].....	14
9. Odroid U3 single board computer [37].....	15
10. Sabrent USB-AVCPT 2.0 Video/Audio Capture & Converter .....	16
11. Tenenergy 7.4V 2600mAh Li-Ion Battery .....	17
12. DC-DC step-down voltage regulator [39].....	18
13. <i>a)</i> Actual CCD sensor array of the camera [42] .....	20
14. Camera model for the image formation and showing relation between the FOV and the sensor size .....	21
15. The relation between the flight time, aircraft speed (10m/s to 50m/s) and elevation with respective ground resolution to cover the area of 0.5×0.5 miles for Tetracam ADC Lite. ....	24
16. The relation between the flight time, aircraft speed (10m/s to 50m/s) and elevation with respective ground resolution to cover the area of 0.5×0.5 miles for FLIR Photon 320 infrared camera. ....	25
17. Alignment of two-camera system side by side in parallel, <i>a</i> represents the offset section in the field of view and <i>b</i> represents the overlap section between two cameras. ....	26

18. The offset in the field of the view due to the deflection or shift of the sensor angle in the single camera.....	27
19. Deflection points at the camera edges on the mounting plate .....	29
20. FEA model for deflection of 0.19-inch mounting plate.....	30
21. The net deflection of the both FLIR Photon 320 and Tetracam ADC lite on different mounting plate thickness with 1g, 3g and 5g accelerations. ....	31
22. The net combined offset from both Tetracam ADC Lite and Flir Photon 320 for 1g, 3g and 5g acceleration with mounting plates with different thickness at 500ft elevation.....	32
23. Fixed stable camera system setup for tuning purpose .....	33
24. Target board for tuning the camera alignment.....	34
25. Experimental setup for the tuning of the camera system in the lab environment. ....	35
26. The overlaid images on top of another with MATLAB software showing the alignment of vertical straight line of the target board.....	36
27. Control points (landmarks) selection for computing affine transformation matrix .....	40
28. Forward warping algorithm illustration [48] .....	41
29. Inverse warping algorithm illustration [48] .....	41
30. FLIR Photon 320 image of target board <i>a)</i> original image <i>b)</i> warped image using affine transformation matrix.....	42
31. Overlaying of Tetracam image and warped image of the FLIR Photon 320.....	42
32. Target board showing reference points for measuring pixel offset .....	43
33. Pinhole camera model [53].....	44
34. Calibration images used for the Tetracam ADC lite camera calibration .....	47
35. A plot showing the distortion model of the Tetracam ADC lite.....	49
36. Image <i>a)</i> and <i>c)</i> are distorted image <i>b)</i> and <i>d)</i> are undistorted image of Tetracam ADC lite multispectral camera .....	50
37. Calibration Checkerboard pattern made with aluminum foil sheet and paper.....	51
38. Image of the checkerboard at ambient temperature (left).....	52



39. FLIR Photon 320 checkerboard image showing the corner extraction performance during camera calibration process. ....	53
40. FLIR Photon 320 Complete Distortion Model .....	55
41. <i>a)</i> Original FLIR Photon 320 image <i>b)</i> Rectified image from the camera calibration parameters .....	56
42. <i>a)</i> Original image from the FLIR Photon 320.....	56
43. Edge detected FLIR Photon 320 infrared images .....	57
44. Block diagram showing the physical connection of the equipment in the integrated payload. ....	61
45. 15-Pin Flat edge Multi I/O connector located inside the Tetracam ADC lite. ....	62
46. Diagram of GPIO Pins of the Odroid U3 single board computer [37] .....	63
47. Circuit diagram of the voltage divider [65]. ....	63
48. Integration of the camera system using GPIO pins of single board computer and Multi I/O pins of Tetracam ADC lite.....	64
49. Flow chart of operation of integrated camera systems .....	65
50. Capture time experiment images. ....	67
51. Teflon tag calibration images <i>a)</i> highly saturated image <i>b)</i> less saturated image.....	70
52. Preview of Tetracam ADC lite configuration menu [22] .....	71
53. Aircraft ground area coverage with flight speed [22].....	71
54. Snapshot of the Index Tools menu of the Pixel Wrench 2 software showing calibrate button and raw image processing options [22].....	73
55. Separation of Multispectral image from Tetracam ADC lite <i>a)</i> Infrared band image <i>b)</i> Near Infrared band image <i>c)</i> Red band image and <i>d)</i> Green band image.....	75
56. Spectral reflectance signature of the healthy and unhealthy vegetation in visible through near infrared spectrum [32].....	76
57. Color mapped NDVI using separated band images in Figure 60 .....	77
58. False color combination image (R, G, B) = (IR, NIR, Green) at 74 °F .....	79
59. False color combination image (R, G, B) = (IR, NIR, Red) at 74 °F.....	80
60. False color combination image (R, G, B) = (IR, Red, Green) at 74 °F.....	80

61. Normalized Difference band ratio of (IR-NIR) / (IR+NIR) at 74 °F .....	81
62. Normalized Difference band ratio of (IR-Red) / (IR+Red) at 74 °F .....	82
63. Normalized Difference band ratio of (IR-Green) / (IR+Green) at 74 °F .....	82
64. Adding segmented infrared on top of NDVI .....	83
65. Warm-blooded target in front of the vegetation at 50 °F .....	86
66. Warm-blooded target in front of the vegetation at 74 °F .....	86
67. Warm-blooded target in front of the vegetation at 85 °F .....	87
68. Warm-blooded target in front of the vegetation at 92 °F .....	87
69. Warm-blooded target partially behind the vegetation at 50 °F .....	88
70. Warm-blooded target partially behind the vegetation at 74 °F .....	88
71. Warm-blooded target partially behind the vegetation at 85 °F .....	89
72. Warm-blooded target partially behind the vegetation at 92 °F .....	89
73. Warm-blooded target hiding behind the vegetation at 50 °F .....	90
74. Warm-blooded target hiding behind the vegetation at 74 °F .....	90
75. Warm-blooded target hiding behind the vegetation at 85 °F .....	90
76. Warm-blooded target hiding behind the vegetation at 92 °F .....	91
77. False color combination for the warm-blooded target in front of the vegetation.....	92
78. False color combination for the warm-blooded target hiding behind the vegetation.....	93
79. Normalized band ratios for the warm-blooded target in front of the vegetation.....	95
80. Normalized band ratio for the warm-blooded target hiding behind the vegetation.....	96
81. Bar graph representing visibility ranking for the warm-blooded target in front of vegetation.....	99
82. Bar graph representing visibility ranking for the warm-blooded target partially behind the vegetation.....	99
83. Bar graph representing visibility ranking for the warm-blooded target hiding behind vegetation.....	100

84. Registration of segmented infrared image on top of NDVI for warm-blooded target in front of vegetation <i>a)</i> At 50 °F and <i>b)</i> At 74 °F .....	101
85. Registration of segmented infrared image on top of NDVI for warm-blooded target in front of vegetation <i>a)</i> At 85 °F and <i>b)</i> At 92 °F.....	101
86. Registration of segmented infrared image on top of NDVI for warm-blooded target partially covered by vegetation <i>a)</i> At 50 °F and <i>b)</i> At 74 °F .....	102
87. Registration of segmented infrared image on top of NDVI for warm-blooded target partially covered by vegetation <i>a)</i> At 85 °F and <i>b)</i> At 92 °F .....	103
88. Registration of segmented infrared image on top of NDVI for warm-blooded target hiding behind the vegetation <i>a)</i> At 50 °F and <i>b)</i> At 74 °F .....	103
89. Registration of segmented infrared image on top of NDVI for warm-blooded target hiding behind the vegetation <i>a)</i> At 85 °F and <i>b)</i> At 92 °F .....	104
90. Bar graph representing the ranking of the segmented warm-blooded target registered on top of NDVI .....	106

## LIST OF TABLES

Table	Page
1. UAS elevation, Ground resolution and FOV for the Tetracam ADC Lite multispectral camera. ....	22
2. UAS elevation, Ground resolution and FOV for the FLIR Photon 320 infrared camera. ....	22
3. Power budget for the individual components in the payload.....	23
4. Pixel offsets at control points of the circular pattern for comparing Tetracam image and warped Flir image.....	43
5. Tetracam ADC lite camera calibration results containing estimated camera parameters, uncertainty on parameter estimation with three times standard deviation and coefficient of variation. ....	48
6. Thermal properties of aluminum and paper [58] .....	51
7. FLIR Photon 320 infrared camera calibration results containing estimated camera parameters, uncertainty of parameter estimation with three times standard deviation and coefficient of variation. ....	54
8. Coefficient of determination ( $r^2$ ) of the line test.....	58
9. Ranking rubric for visibility of warm-blooded target.....	98
10. Ranking rubric for registration of segmented infrared image on top of NDVI.....	105

## ACKNOWLEDGEMENTS

Firstly, I would like to thank my academic advisor, Dr. William Semke, for giving me the opportunity to pursue this project as well as his support and guidance throughout my graduate career at the University of North Dakota. I would like to thank my committee member, Dr. Clement Tang, for his advice and support. I would also like to thank my other committee member, Dr. Jeremiah Neubert, for inspiring me to work in computer vision and image analysis related research field.

This research was supported in part by the UND Office of Research and Economic Development grant, “Developing Unmanned Aircraft Systems for Wildlife Ecology Studies at UND”. Educational Licenses of software used were supported by the UND Department of Mechanical Engineering.

Finally, I would like to thank my parents, Surya Man and Ganga Maya, my brother Shushil Shahukhal and my friends for supporting and believing in me. Without them, this wouldn't have been possible.

## ABSTRACT

The purpose of this research is to enhance visualization of warm-blooded animals and analyze the vegetation in which they are located using a camera system mounted on Unmanned Aircraft System (UAS). The results are coherently displayed in a single image at the same spatial location so that biologists will have accurate animal counts along with vegetation conditions. Application of aerial imagery has been used to analyze the vegetation health and determining the number of the animals by the wildlife service. However, a major obstacle of the research is to combine the two imaging systems to obtain the same spatial image with enhanced visualization. The two camera systems used in this research are the Tetracam ADC lite multispectral and the FLIR Photon 320 infrared camera. These two camera systems each have a different lens, field of view and sensor array size. The project involves the alignment of the two cameras to pixel level for the spectral image analysis. The spectral image analysis provides both vegetation information, such as Normalized Difference Vegetation Index (NDVI), along with enhanced visualization of warm-blooded targets. The system was miniaturized for the standalone payload for aerospace applications including UAS.

The FLIR Photon 320 was used to capture the infrared image and a Tetracam ADC lite multispectral camera was used to capture the near infrared, red and green spectral band images. A laboratory experimental setup was designed to mechanically align the two camera systems to get close identical spatial imagery. Spatial registration of the two images was performed using reverse image warping method by finding affine transformation

matrix using point correspondences. Both camera systems were calibrated using Camera Calibration Toolbox for Matlab to reduce any distortion due to the lenses. A single board computer is used to capture and store the image data from FLIR Photon 320 infrared camera while the Tetracam image data is stored internally on board. The image capture time was set by continuous timed delay triggering within the Tetracam camera. The single board computer follows the Tetracam signals and matches the FLIR Photon 320 still image acquisition time with the Tetracam ADC lite.

Once the images are captured and stored by the camera systems, the files are downloaded and image processing is conducted. The data was analyzed to calculate the NDVI to observe the plant health. The infrared spectral band was used to identify the warm-blooded animals. In addition, various false color combinations of spectral bands and normalized difference ratios are processed to observe the visual enhancement capabilities on the vegetation and warm-blooded animal. It was determined that detected warm-blooded animal in the infrared band registered on top of NDVI image to show the vegetation health in a single image produced effective results. The combined image data from the FLIR Photon 320 and Tetracam ADC lite produced meaningful vegetation and animal information in the single image. This enhanced the capacity to identify and count animals while simultaneously characterize the vegetation environment, which is highly desired in ecosystem studies

## CHAPTER I

### INTRODUCTION

The purpose of this study is to integrate the multispectral imaging systems for enhanced visualization biological studies using Unmanned Aircraft System (UAS). This study makes us the use of remote sensing technology that merges with the spectral detection of the biological targets. UAS has been widely used in many remote-sensing applications due to its cost effective, less labor intensive and high-resolution data. The recent developments of the miniaturized sensors, direct georeferencing tools, and control algorithms for UAS have given the scientist and researchers to broaden up the application of UAS in hazardous areas such as wildfire, toxic areas where human intervention is not feasible [1-4].

On the successful operation of the UAS for remote sensing, it is necessary to consider the certain factors before the data capture. Area coverage, flight speed, flight time, remote network issue, data capture and storage all factors play an important role in the data capture feasibility [5]. The preliminary studies are also needed to select sensor for its size, weight, resolution and data storage mechanism. The quality of data captured for the remote sensing application is highly affected by the resolution of the sensor. The resolution study predicts how much spatial resolution can be obtained from the sensor to study the interested targets from the certain elevation of the UAS [6, 7]. Onboard processing and huge data storage is still the hardware challenge that limits UAS from several intensive processing



related applications. Besides these limitations, UAS offers the benefits of extensively cheap and reliable remote data collection.

Application of the UAS for biological studies such as wildlife survey and precision agriculture is a new emerging technology in recent years. Traditionally biologists rely on the visual aid to detect and quantify the animals [7-11]. This approach is heavily labor intensive, has chances of miscounting and inability to detect animals in dense vegetation and nocturnal periods [8]. Visual band camera has been used most often for the surveillance of the wildlife using UAS. Another technology including an infrared sensor in UAS gave new improvement to the traditional approach of surveillance. Infrared imaging technology enhanced the data collection of the warm-blooded target based upon the temperature difference between target and the environment. This technology improved the data collection at night, when most animals are active and even detect the animals in dense vegetation during the daylight [7-11]. The use of the remote sensing with UAS has extended the ease of the data collection process in wildlife survey with the limited intrusion of wildlife [9-11].

Many research has been done to detect and count the animals using remote sensing technology with the aid of Unmanned Aerial Vehicles (UAVs). Gemert et al. showed the use of the UAV for automatic localization and counting of animals. He successfully evaluated the efficiency of different high-speed detection methods [12]. Chretien et al. used the UAV with visible and thermal infrared imagery for detection of multispecies of animals. The project was aimed to detect bison, fallow deer, gray wolves and elks. The study was successful to detect bison and elk without errors [13].

The recent development of the inexpensive, ultra-light multispectral cameras with near infrared and visible bands have added the capabilities of determining the vegetation condition remotely using UAS [14]. Many research has been done in precision agriculture using the UAS. Stagakis et al. used the UAV with six narrow spectral bands in the visible and near infrared bands data to analyze the water stress status and predict the effect of stress on citrus fruit. The structural, chlorophyll and photochemical indices were extracted from the aerial spectral images to track the water stress. The result demonstrated that the Photochemical Reflectance Index (PRI) successfully tracked down water stress before it was detected by Normalized Difference Vegetation Index (NDVI) [15]. Panigada et al. showed the use of hyperspectral data captured from UAV for vegetation stress detection and use of PRI and solar induced chlorophyll for early detection of vegetation stress due to ozone exposure and water deficiency [16]. Baldeck et al. studied the variation of the plant community in African savanna due to the landscape scale variation using the airborne multispectral data. The data was captured over the large variation of different topology and vegetation was mapped using spectral reflectance and structural characteristics [17]. Sanchez et al. used the UAV with six different spectral and visible cameras to acquire images for early specific weed management study [18].

In past, some research work is done using the infrared and multispectral imaging system as a single payload for remote sensing in vegetation monitoring. In most of the study, the two sensors were used independently without physical alignment and controlled timed data collection. The multispectral camera containing near infrared, red and green were used to monitor the healthy vegetation and infrared camera was used to detect environment and vegetation temperature. In 2009 Berni et al. used the thermal infrared and

multispectral camera with 6 bands in a single UAV payload to detect the vegetation health and its relation with the canopy temperature. He was able to detect the relationship between canopy temperature with respect to NDVI and PRI index with the precise integration of two imaging system shown in Figure. 1 [19].

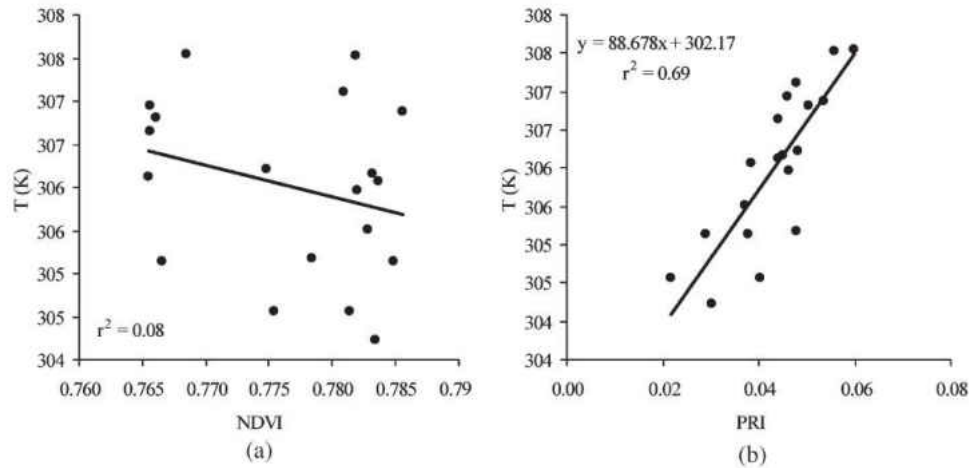


Figure 1. Relation of canopy temperature with NDVI and PRI [19].

In 2012 Bending et al. integrated the infrared with the Tetracam Mini MCA 4 band multispectral imaging system to study the NDVI and response temperature of four different type of sugar beet in the city of Bonn in the west of Germany [20]. In 2014 Turner et al. integrated the visible multispectral and thermal infrared sensor for UAV payload using the spatial co-registration method for the study of moss health and temperature shown in Figure 2. The study was successful to co-register the images from the different sensor with a root mean squared error of 1.78 pixels. The images from different sensor were initially geo-referenced separately. To improve the spatial co-registration the 30 cm diameter metal disks were manually located to use as Ground Central Points (GCPs). Later on, the GCPs were used as checkpoints for co-registration accuracy [21].

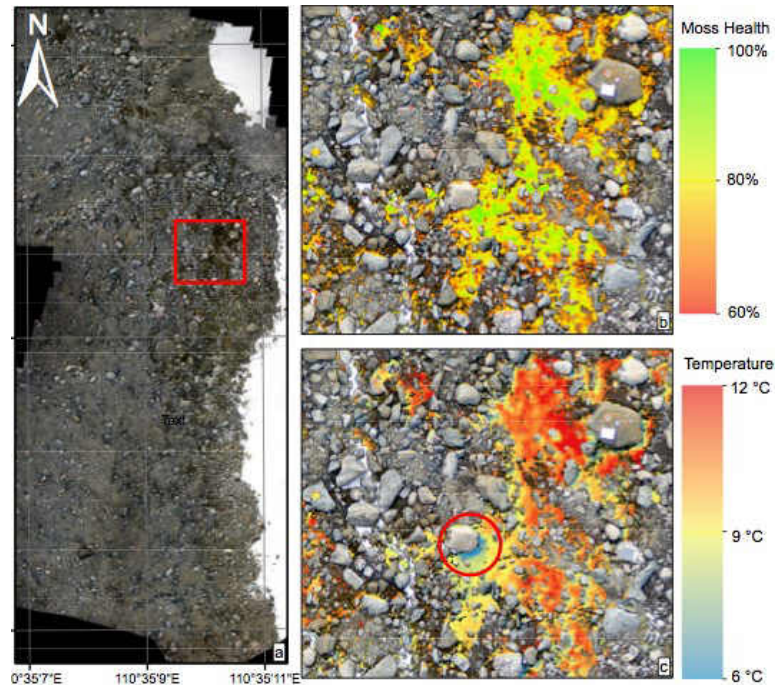


Figure 2. Spatially co-registered image showing moss health and temperature [21]

The UAS payload system used in this research consists of two cameras; one is the Tetracam ADC lite multispectral camera and the other one is the FLIR Photon 320 infrared camera integrated compactly in a single payload. Tetracam multispectral camera can capture near infrared, red and green band image and FLIR Photon 320 can capture infrared band imagery [22, 23].

The main reason for integrating the two-camera system is due to the absence of infrared, near infrared, red and green band image in a single imaging system. The multispectral cameras available up to date have the visible to near infrared spectral bands in a single system [22]. They don't contain the infrared band in the same single camera system, which is essential to enhance the visualization of warm-blooded animals in the wildlife survey in the absence of visible lights [8]. The absence of the infrared band in single multispectral camera system has limited the precise spatial data collection for use in

biological as well as ecological studies in the single application of UAS in the past [19, 20]. The Landsat 8 satellite launched on February 11, 2013 by the NASA contains 9 spectral bands including infrared as well as near infrared and visible bands [24]. The spatial resolution of this satellite images are very low, 30 meters for the visible and near infrared and 100m for the infrared bands and satellites have large revisit period [19, 24]. Remote sensing is highly dependent on the accurate production of the images, interpretation and analysis of the imagery [7, 25]. The low resolution makes the satellite images impractical for remote sensing in the vegetation monitoring and in wildlife surveying [19]. UAS overcomes this problem by low elevation flight with a desirable spatial resolution [1-7]. For the application of the agricultural and vegetation study, the currently available multispectral camera with NIR, Red and Green bands is sufficient to predict the healthy vegetation. In addition including the infrared band to the currently available multispectral imaging system will elevate the future studies on the plant-animal relation in wildlife ecosystem.

Construction of the multispectral camera to capture a wide range of electromagnetic bands by mounting a single lens is very difficult to achieve. Electromagnetic waves have different characteristics on different types of materials [7]. In general, a visible camera lens is made of glass. Glass is transparent to visual wave spectrum. However, the type of glass lens used in generally visible cameras cannot be used for optics in an infrared camera, as they do not transmit infrared wavelengths greatly [26]. On the other hand, materials that are transparent to infrared are often opaque to visible light [26]. So the optical lens used for the construction of the cameras itself have certain limitations on the electromagnetic waves. Infrared camera lenses are typically made of silicon (Si) and germanium (Ge)

materials. Mostly Si is used for MWIR (medium wavelength IR) camera systems, whereas Ge is used in LW (long wavelength) camera [26]. Since a single lens is unable to pass all electromagnetic spectrum through it, this limits the ability to acquire spectral images in a single unit. In addition, the infrared camera uses a microbolometer sensor for image formation which is different than CMOS sensor of the visible to near infrared multispectral camera.

There are many obstacles in the construction of single multispectral imaging system including infrared, near infrared and visible bands. This research focuses on the methods of combining the two imaging systems externally to produce spatially aligned images in pixel level by camera alignment, timed data capture and image processing. In order to successfully integrate the two imaging system, the images from both cameras must align to the pixel level such that each corresponding pixel in the different band of images must cover the same field of view, must have same environment information at the same location. The precise time controlled data collection from the Tetracam ADC lite is one of the major issues from the past experiences which affects the integration [27]. The feature-based alignment using machine vision application won't accomplish the registration of these two images with high accuracy since the object detected by one of the spectral band might not be detected by the other bands at all-time [28]. So the spatial alignment of two images was performed heavily relying on the physical camera alignment and corrected through digital image processing. The time controlled data capture problem was solved using the Tetracam ADC lite as a master and FLIR Photon 320 as a slave configuration. In this way, Tetracam and FLIR Photon capture the image with the same scene coherently without any significant time difference.

After the successful integration of the two imaging system. The pair of images from two imaging system is tested for enhancing the visualization of the warm-blooded target through spectral image analysis. For enhancing the visualization of targets using spectral image analysis we need to understand the spectral signature of the interested targets. In nature the different materials absorb, radiate and reflect energy through different wavelength of electromagnetic spectrum depending upon its physical and chemical makeup [7, 29]. The reflectance of the material can be traced to a different wavelength, which makes up its spectral signature [7, 29]. The spectral signature shows the relationship between the material reflectance magnitudes with respect to the wavelengths of electromagnetic spectrum. It helps us to identify reflectance variation of a different object present in the area of interest with respect to spectral bands.

The multispectral image contains multiple layers of images over different wavelengths of electromagnetic bands in a single scene. All the individual images corresponding to specific bands are stacked up to create the array of images. The example of a multispectral image with several layers and spectral signature of the soil, water and vegetation is shown in Figure 3.

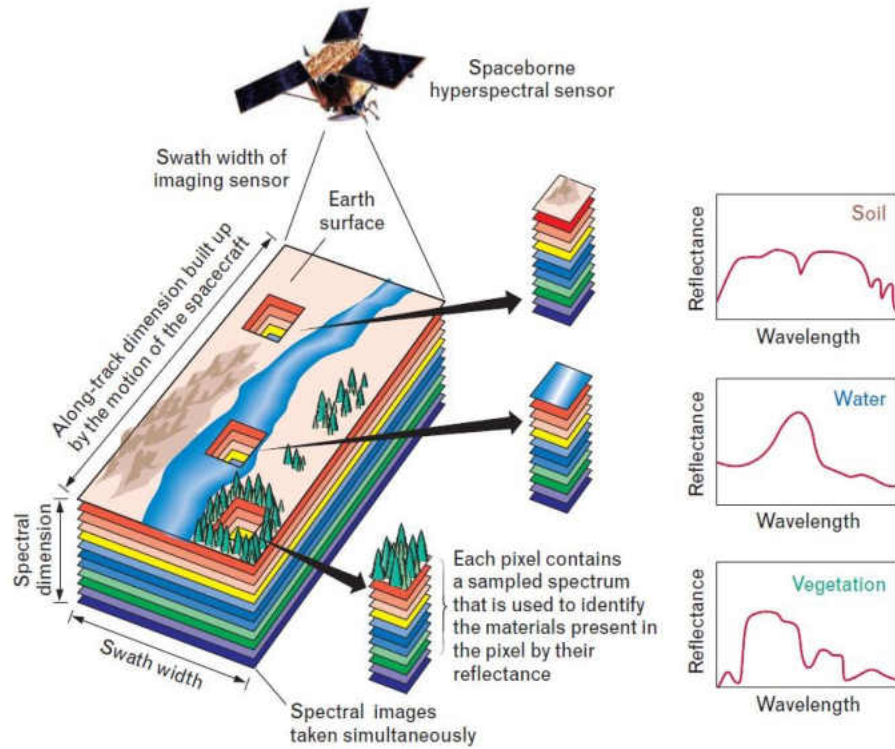


Figure 3. Stacking of several layers of spectral images for each pixel showing sampled spectral information for soil water and vegetation [29].

The prior knowledge of the environment, behavior, size and spectral response of the targeted object is essential for the visualization [8]. To understand the detection ability of the sensor we need to understand the spectral behavior of the objects. These different phenomena of the object to different electromagnetic bands enable us to detect and classify the target object based upon spectral response. The target object may highly absorb some electromagnetic waves and highly reflects others depending on its nature. Plants are a very good example to show the variation of the spectral behavior. Figure 4 shows the spectral signature of the healthy and unhealthy plants. Healthy green leaves highly absorb the red band wave for photosynthesis process and highly reflect the near infrared band. Whereas the stressed plant cannot absorb the red band but absorbs the near infrared band [7, 30, 31].



With this certain characteristics, we can differentiate the healthy green plant from the stressed plant with the aid of spectral image analysis only using near infrared and red band images. With the benefit of having near infrared, red and green bands in the same camera. We can estimate the vegetation index such as Normalized Difference Vegetation Index (NDVI), which is a widely used method for determining the vegetation health [7, 31-32].

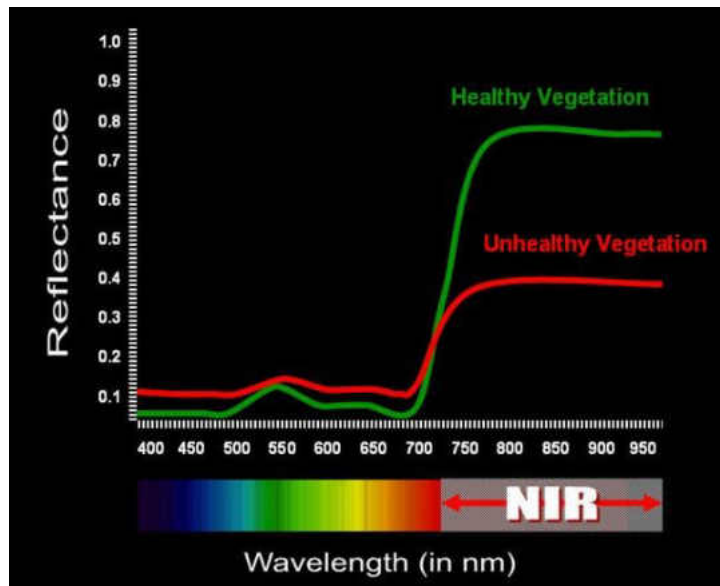


Figure 4. Spectral signature of the healthy and unhealthy vegetation [32]

This thesis will put emphasis on the method of integrating multispectral and infrared imaging system. It will explain the payload sensors and its abilities, methodology for the timed controlled data collection from both cameras. It illustrates the collection of the raw image data, post-processing of images to prepare spatially aligned images in pixel level for false color combinations, overlapping and spectral image analysis. It shows the experimentation of the several possible spectral manipulations between image pair to observe the visualization enhancement. Finally, it sums up the conclusions based on the observation of the results obtained from spectrally combined imagery.

## CHAPTER II

### SYSTEM DESCRIPTION

#### Payload

The payload for the integrated camera system consists of the Tetracam ADC Lite multispectral camera and FLIR Photon 320 infrared camera. It has an Odroid U3 single board computer to capture the still infrared images from FLIR Photon 320 through Sabrent USB-AVCPT frame grabber. Three 7.4 volt lithium-ion batteries are used to power up the two cameras as well as single board computer system. The payload was miniaturized for size and weight to fit in a small UAVs. The payload is developed to function as a single standalone independent data capturing system. The multispectral camera has the ability to store the images in its own CF card installed inside the camera whereas the output of the FLIR Photon 320 infrared camera is an analog video. Figure 5 shows the schematics of the physical connection of the equipment to form a single standalone payload. A Sabrent USB-AVCPT frame grabber interfaces with the FLIR Photon 320 and single board computer through USB port and RCA cable to perform the data capture process. The Tetracam ADC lite and the Odroid U3 single board computer are connected through Multi I/O pins and GPIO pins for sending logic signals during data capture process. The FLIR Photon 320 can be operated in a range of 5-24 Volt DC power supply and Tetracam ADC lite multispectral camera required 5-12 V voltage to operate. The 5V DC-DC step-down voltage regulator is used to reduce the 7.4 V from the lithium ion battery to match up with Odroid U3 maximum

voltage rating of 5 V. The description of the individual equipment and parts are described sequentially in the following sections. Figure 6 shows the actual final integrated payload.

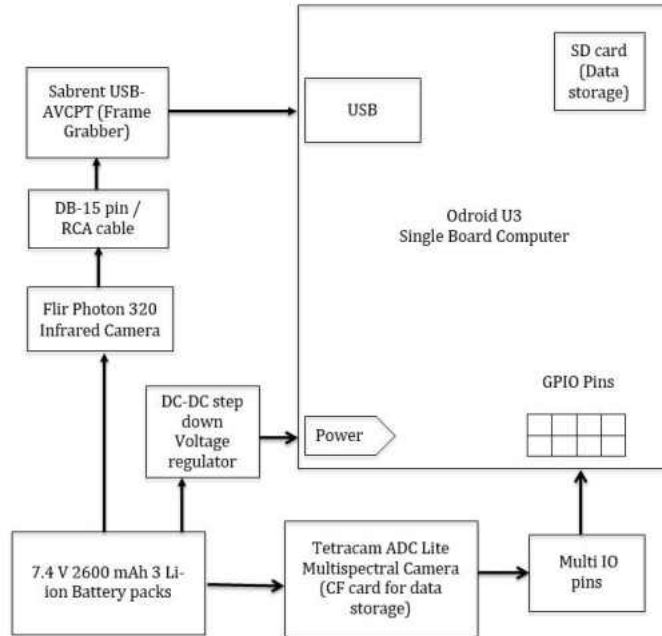


Figure 5. Schematics of a Payload System

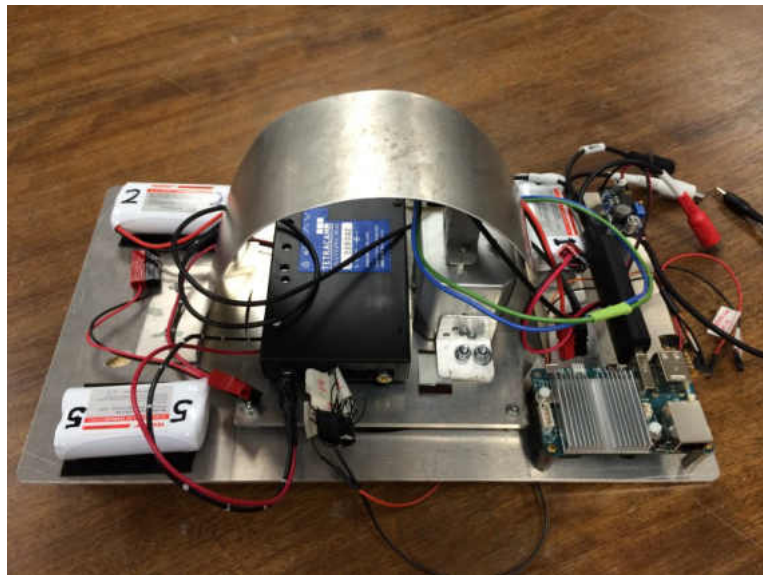


Figure 6. Standalone UAS payload for the integrated multispectral imaging system

### *Tetracam ADC Lite Multispectral Camera*

Tetracam ADC lite is the lightweight agricultural digital camera designed by Tetracam Inc. specifically to use in small UAV application. It is widely used imaging system in precision agriculture application. It has a fixed 8 mm focal length lens with single CMOS sensor that can capture visible light with wavelengths longer than 520nm and near infrared (NIR) up to 920nm [22]. The captured Red, Green and NIR image band has wavelength approximately equal to TM2 (520nm- 600nm), TM3 (630nm-690nm) and TM4 (760nm-900nm) of Landsat images [33, 34]. The each pixel size of the CCD array is 3.2 micron with 2048x1536 pixels in the horizontal and vertical direction which forms the sensor size of 6.59x4.9mm. The operating voltage of the camera is 5.0-12 VDC with an average power rating of 6-Watts [22]. This camera can capture and save the image in three different formats RAW 8 bit, RAW 10 bit and DCM 10. The fastest data capture cycle is RAW 8 bit format with approximately 3 seconds per single image. RAW 10 bit format takes 4 seconds and DCM 10 format takes 7 seconds [33].



Figure 7. Tetracam ADC Lite multispectral camera [22]

### *FLIR Photon 320 Infrared Camera*

FLIR Photon 320 is the lightweight longwave infrared (LWIR) camera designed by FLIR Systems, Inc. It uses uncooled microbolometer sensor made up of vanadium oxide ( $\text{VO}_x$ ) which detects the electric resistance changes due to temperature. Each single microbolometer represents individual pixels to form the sensor array [35]. FLIR Photon can capture infrared spectral band ranging from  $7.5\mu\text{m}$  to  $13\mu\text{m}$  [36]. This camera displays the infrared analog video with 30 frames per second (fps) [23]. FLIR Photon 320 was chosen amongst other infrared cameras because of its small size and lightweight. This lightweight and small size feature provide the opportunity to mount on the small UAVs. It has 19 mm fixed focal length lens with 36 degrees horizontal field of view. It has sensor array of  $320 \times 240$  pixels with each pixel size of  $38 \times 38$  microns resulting sensor size of  $12.160\text{mm} \times 9.12\text{mm}$ . This camera has DB 15 interface for analog video out and power in. It can be operated in the voltage range of 5-24 volts and has an average power rating of 1.65 Watts [23].



Figure 8. FLIR Photon 320 infrared camera [23]

### *Odroid-U3 Single Board Computer*

Odroid U3 is the single board computer manufactured by Hardkernel Co. Ltd. It has 1.7GHz A9 Quad-core processor with 2GB low power DDR2 memory [37]. As comparing with the other available single board computers, from the performance over price perspective, this one is the most efficient product available in the market. After several unsuccessful attempts to grab still images through Sabrent USB-AVCPT frame grabber using Beaglebone Black single board computer with processor (1GHz ARM Coretex-A8) and memory of (DDR3 512 MB), Odroid U3 single board computer was chosen because of its high processing speed of 1.7GHz Quad-core and high memory of 2GB. This miniature computer can be run with lightweight Linux operating system and can be used in multiple applications [37]. It is small in size 83 x 48 mm and has lightweight 48g. It also includes a heat sink, which adds benefit to dissipate the heat generated during operation.



Figure 9. Odroid U3 single board computer [37]

### *Sabrent USB-AVCPT 2.0 Video/Audio Capture & Converter*

Sabrent USB-AVCPT is a video capture device, which is used to interface between the FLIR Photon 320 infrared camera's RCA cables to the USB port of the single board computer. This device helps to capture the analog video from the FLIR Photon 320 infrared camera through single board computer by USB interface. It contains multiple inputs including two audio, one composite video, and one S-Video. The Odroid U3 single board computer operates on a Linux operating system. This device is compatible with both Windows and Linux operating system. In addition, it is very inexpensive frame grabber available in the market with a USB interface, which can operate in the Linux operating system. [38].



Figure 10. Sabrent USB-AVCPT 2.0 Video/Audio Capture & Converter

### *Lithium Ion Batteries*

The three batteries that are used in the payload is the Lithium-ion battery from Tenergy with 7.4 V and 2600 mAh. Each piece of equipment in the payload is powered by a separate individual battery. This battery is selected due to its small size and sufficient

power content to run the onboard equipment during minimal flight time. These batteries have continuous discharge current of 2.6 A and maximum discharge current of 5.9 A. The size of the lead wire is 22 American Wire Gauge (AWG). Special attention should be given to the continuous discharge current magnitude and lead wire gauge of the battery to make sure the supply of current is enough to run the equipment smoothly.



Figure 11. Tenergy 7.4V 2600mAh Li-Ion Battery

### *DC-DC Step Down Voltage Converter*

The single board computer Odroid U3 has a maximum rated input voltage of the 5V while the lithium ion batteries used in payload have the voltage rating of 7.4 volts. The DC-DC step down voltage converter is used to lower down the voltage from 7.4 volts to 5 volts. It has one input and one output terminal section. Input terminals can accept maximum voltage rating up to 35 V [39]. The output voltage can be reduced to the desirable amount by turning the knob on the blue potentiometer with the flat screwdriver gently while monitoring the output voltage using a voltmeter. Once the desirable 5V is obtained in the output terminals the knob can be sealed with glue to reduce the disturbances in the knob.





Figure 12. DC-DC step-down voltage regulator [39]

## CHAPTER III

### SYSTEM PERFORMANCE CAPABILITIES

#### Resolution

The remote sensing application is highly influenced by the resolution of the collected images [7, 40]. High ground resolution is recommended to identify a target precisely. Sensor resolution also limits the range of flight elevation for UAS. The size of the object of interest acts as a constraint for the ground resolution. In this research, we are interested in identifying the small warm-blooded animal including small mammals, e.g. rabbit and deer. The average body length of brush rabbit is 12 inch [41]. To identify these animals we need at most 12 inch/pixel spatial resolutions from the imaging sensors. On the other hand, we also wanted to increase the field of the view from imaging system for maximum area coverage to minimize the number of passes and flight time. The two camera systems used in the research has different sensor size, resolution and Field of View (FOV). From the camera information, we know that the FLIR Photon 320 infrared camera has lower resolution than the Tetracam ADC Lite multispectral camera. So, we constrained the spatial resolution of the FLIR Photon 320 infrared camera to capture the target.

Spatial resolution is generally expressed as the ground dimension of an individual pixel [7]. Which means how big of an area is mapped with the single pixel of the sensor array. It is generally measured in meter/pixel or inch/pixel. The lower spatial resolution gives the better information of the target since more pixels will be used to grab the same information from the target object. To better understand the resolution of the camera

system we need to look at the main components of the camera such as CCD array size, sensor size, pixel size and number of pixel in the array. Figure 13 shows the actual sensor of camera and grid of sensor array with pixel orientation.

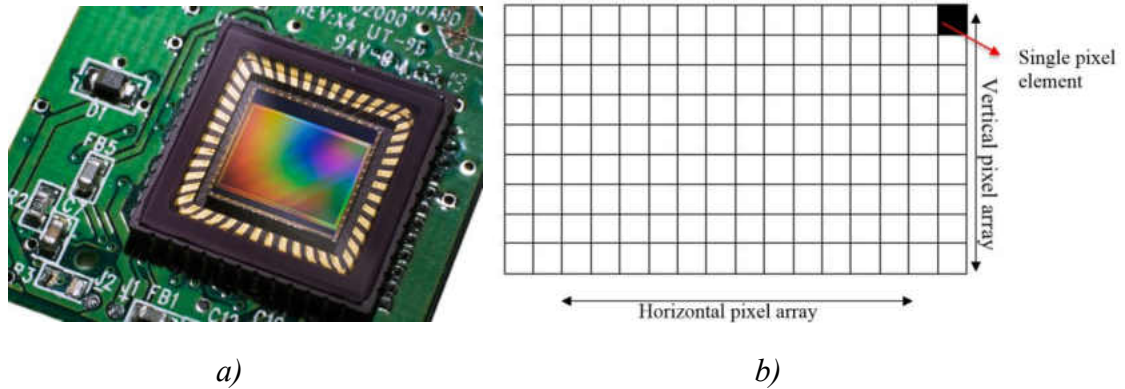


Figure 13. *a)* Actual CCD sensor array of the camera [42]. *b)* Graphical representation of the sensor array and single pixel element.

The sensor array is the grid of individual pixels. Sensor size is the vertical and horizontal dimension of the actual sensor of the camera. Pixels are the small square cells in the camera sensor, which forms the whole sensor array. The size of the each individual pixel is called pixel size [7], usually it is measured in microns. The larger the sensor size dimension gives more room for placing a higher number of pixels in the sensor array. A higher number of pixels will give the good information of the image since more pixels will be used to store the information of the image.

The information from the sensor size, sensor array, aspect ratio and focal length of the camera is used to calculate the field of view and the ground resolution. Using the basic pinhole camera model containing the single objective lens we can relate sensor size, object distance or elevation of UAVs, field of view and focal length of camera lens [43]. The

diagram of the image formation through the lens with the sensor array is shown in Figure 14.

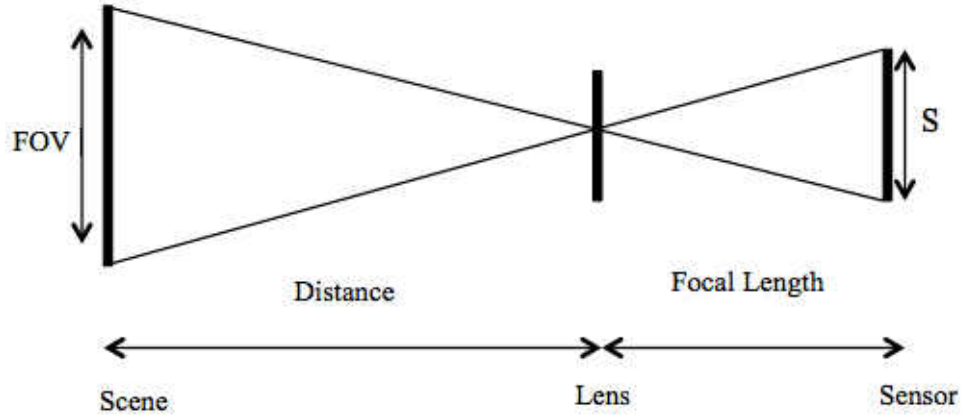


Figure 14. Camera model for the image formation and showing relation between the FOV to the sensor size

With the given sensor size, focal length and elevation we can calculate the FOV in both horizontal and vertical direction which will make up the area covered by the image taken at that condition. In addition using the FOV dimension we can calculate the ground resolution by dividing with the respective pixel numbers in array size [40, 43].

$$\text{Sensor size} \times \text{Elevation} = \text{FOV} \times \text{focal length of camera} \quad (1)$$

$$\text{Ground Resolution} \\ \text{Horizontal resolution} = \text{FOV (H)} / \text{Horizontal pixel number} \quad (2)$$

$$\text{Vertical resolution} = \text{FOV (V)} / \text{Vertical pixel number} \quad (3)$$

Using Equation 2 or 3 we can calculate the ground resolution. The resolution study was carried out for different elevation ranging from 100 ft. to 500 ft. The minimum size of the target object 12 inches is used as the constraint for determining the maximum elevation for the UAS. The calculated values of the ground resolution, field of view (FOV) with

respected to UAV elevation for the Tetracam ADC Lite and FLIR Photon 320 is shown in the Tables 1 and 2.

Table 1. UAS elevation, Ground resolution, and FOV for the Tetracam ADC Lite multispectral camera.

Elevation (ft.)	Ground Resolution (inch/pixel)	Field of View (Width x Height)
100	0.48	82 ft. x 61.5 ft.
200	0.96	163 ft. x 123 ft.
300	1.44	245 ft. x 185 ft.
400	1.91	327 ft. x 246 ft.
500	2.40	409 ft. x 308 ft.

Table 2. UAS elevation, Ground resolution, and FOV for the FLIR Photon 320 infrared camera.

Elevation (ft.)	Ground Resolution (inch/pixel)	Field of View (Width x Height)
100	2.4	65 ft. x 51 ft.
200	4.8	130 ft. x 102 ft.
300	7.2	194 ft. x 154 ft.
400	9.6	259 ft. x 205 ft.
500	12	324 ft. x 256 ft.

### Object Size Detection

From Table 1 and 2, we can see that the spatial resolution of the FLIR Photon 320 is very high approximately 5 times of the Tetracam ADC lite multispectral camera. So we will be using the FLIR Photon 320 infrared camera's ground resolution as a constraint for the size detection. The elevation of 100ft to 500ft for the FLIR Photon 320 has the resolution of the 2.4 inches/pixel to 12 inch/pixel, which is a good approximation for the identification of the small warm-blooded animals with an average length of 12 inches. Flying UAS at lower altitude will enhance the ground resolution but increases the time of flight for same area coverage. On the other hand flying at high altitude will also cause the errors in the direct geo-referencing due to small errors in measurement of attitude angles [27].

## Power Budget and Flight Time

The payload has three main components two cameras and one single board computer each having different power ratings. The time for successful operation of components was calculated from the mili Ampere hour (mAh) ratings of the battery used and power consumption of individual components. The battery life for the individual equipment is shown in Table 3. The maximum time limit for proper running of the payload was estimated based upon the power consumption by each piece of the equipment in the payload. The highest power-consuming device was used as the constraint for the flight time. From power budget information we can decide the maximum flight time and later on decide the elevation needed to cover the targeted field of interest in a given flight time.

Table 3. Power budget for the individual components in the payload.

Components	Power Consumption	Battery life
Odroid U3	10 W	1 hr. 20 min
Tetracam ADC lite	6 W	2 hr. 15 min
FLIR Photon 320	1.65 W	8 hr. 10 min

From the Table 3, we can see that Odroid U3 has the minimum run time with the chosen battery. So, the maximum flight time will be based upon the battery life of the Odroid U3, which is 1 hour 20 minutes. The area covered by the imaging system is dependent on the altitude, FOV image width and speed of the UAS. These four parameters can be related with the given Equation 4 [40].

$$S (\text{Area}) = T \times V \times W \quad (4)$$

Where  $T$  = Flight time

$V$  = Speed over ground

$W$  = Ground image width

The relationship between the flight time, aircraft speed and flight altitude with a respective ground resolution to cover the arbitrary test area of 0.5 x 0.5 miles square area is shown in Figure 15 and Figure 16.

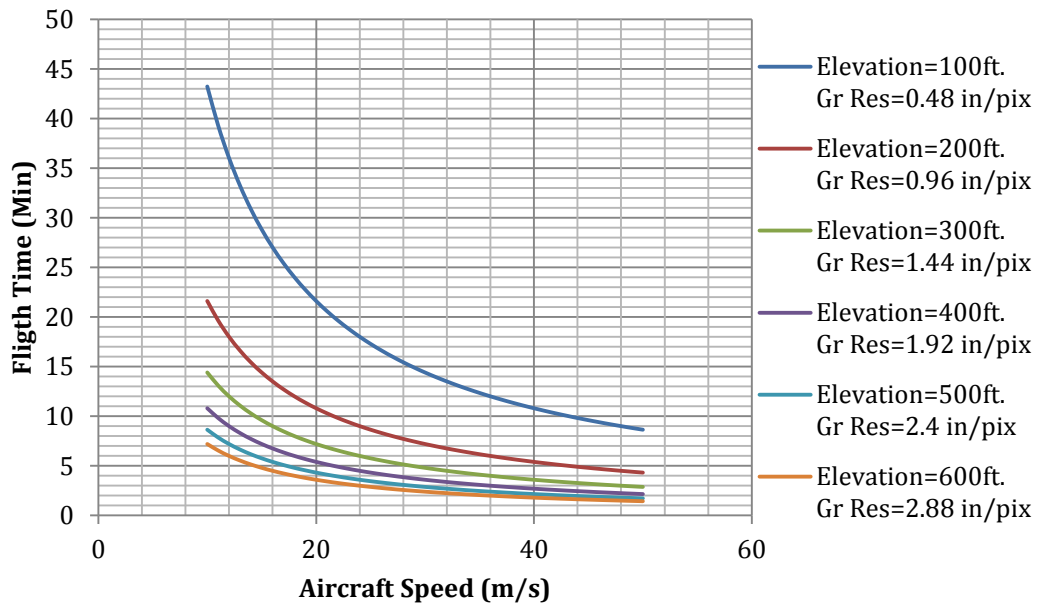


Figure 15. The relation between the flight time, aircraft speed (10m/s to 50m/s) and elevation with a respective ground resolution to cover the area of 0.5 by 0.5 miles for Tetracam ADC Lite.

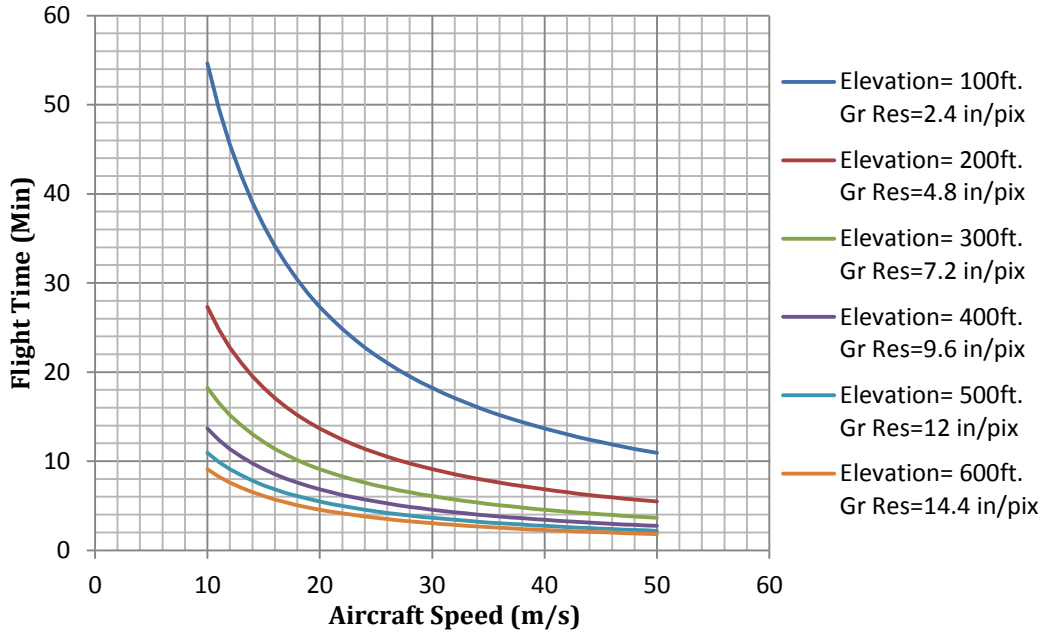


Figure 16. The relation between the flight time, aircraft speed (10m/s to 50m/s) and elevation with a respective ground resolution to cover the area of 0.5 by 0.5 miles for FLIR Photon 320 infrared camera.

From Figure 15 and 16 we can see that the flight time can be minimized by increasing the flight speed and elevation of the UAV to cover the specific area of interest. We also need to consider the minimum resolution needed for object size detection when trading off with UAV elevation. In addition, we also need to consider the data capture rate of the imaging system so that we can get the sufficient area overlap between timed interval images. In general, the recommended area overlap is around 60% for end lap and 30% for the side lap [44]. The data capture rate is discussed in Continuous Capture Configuration of Tetracam section in Chapter V.



CHAPTER IV  
CAMERA ALIGNMENT

The FLIR Photon 320 infrared and Tetracam multispectral camera each have a different field of view at the same elevation due to difference in focal length, sensor size and FOV angle. In many UAV applications, the two imaging sensors are placed side by side in the parallel orientation shown in Figure 17. When the cameras were aligned in such an orientation there will be constant offset between the captured images at the top and bottom edges.

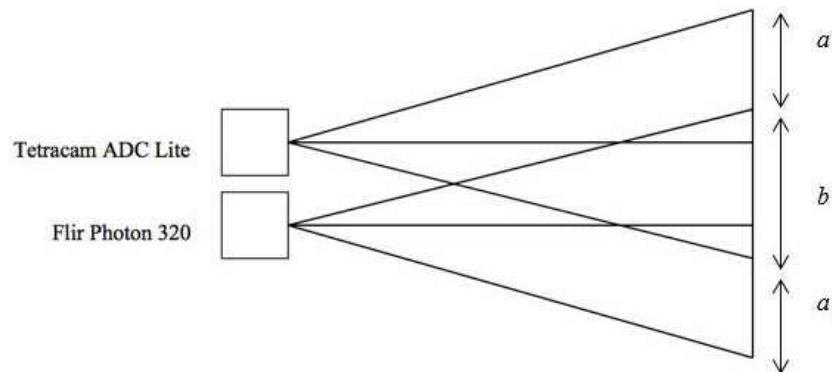


Figure 17. Alignment of two-camera system side by side in parallel,  $a$  represents the offset section in the field of view and  $b$  represents the overlap section between two cameras.

On the other hand deflection on the mounting structure exists due to the non-uniform distribution of weights from the two cameras. The deflection will be high at the middle of the mounting plate and low at the far edges of the camera. This will create a slight angular shift on the camera and its sensor, which creates a large shift in the field of view offset in the ground depending on the elevation. So, the study of deflection analysis

of the mounting plate and its effect in the offset of the field of view was needed to precisely tune the alignment.

### Mounting Plate Deflection Analysis

Both the Tetracam ADC lite and the FLIR Photon 320 Infrared (IR) camera are mounted on top of the aluminum plate of the payload. The deflection of the mounting plate due to the weight of the both camera plays a vital role in the shifting of the field of view on the ground with respect to the elevation. The weights of the two cameras are also different Tetracam multispectral camera weighs 200gm and FLIR Photon 320 infrared camera weigh 97 gm [22, 23] so, the deflection will be different at the edges of the individual camera system. This deflection will cause the shift in the original field of the view from both cameras as shown in Figure 18 for the single camera system.

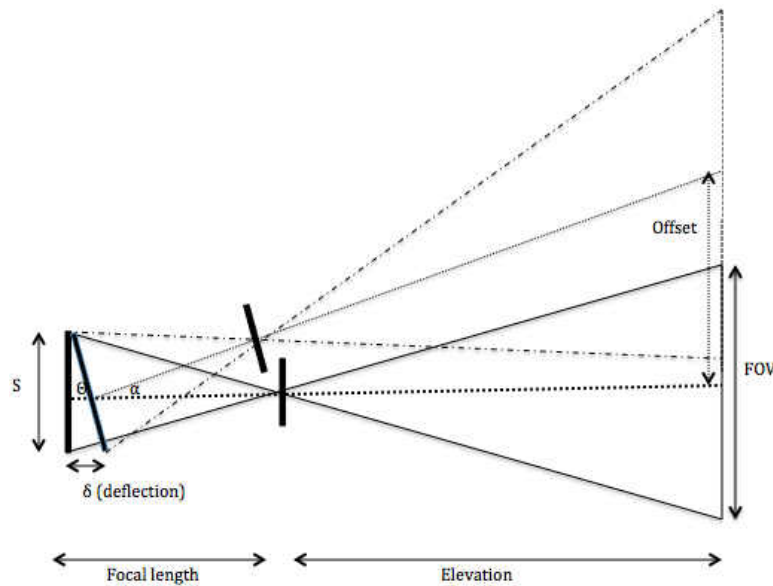


Figure 18. The offset in the field of the view due to the deflection or shift of the sensor angle in the single camera.

From the diagram shown in Figure 18, we can compute the field of view shift from the center of the image at the ground level from given elevation of the UAV and sensor deflection.

$$\theta = \alpha \quad (5)$$

$$\tan(\theta) = (\delta/S) \quad (6)$$

$$\tan(\alpha) = \text{offset/elevation} \quad (7)$$

$$\text{FOV offset} = (\delta/S) \times \text{elevation} \quad (8)$$

As we can observe from the Equation 8 even if the deflection is small, at high elevation it will significantly increase the offset in the field of the view. So we need to minimize the deflection of the mounting plate as well as fly the UAV at the lower desired altitude to minimize offset in the field of view. The estimation of the deflection of the mounting plate due to the weights of the two cameras is computed using finite element method. The point loads were added at the places where the two camera rests on the mounting plate. The application forces are applied for 1g, 3g and 5g acceleration. Fixed supports were applied at the four screw holes at the corners of the mounting plate for zero deflection boundary conditions. The camera sensor net deflection is computed by taking the difference in deflection between the camera edges. The deflection points at the camera edges are shown in Figure 19.

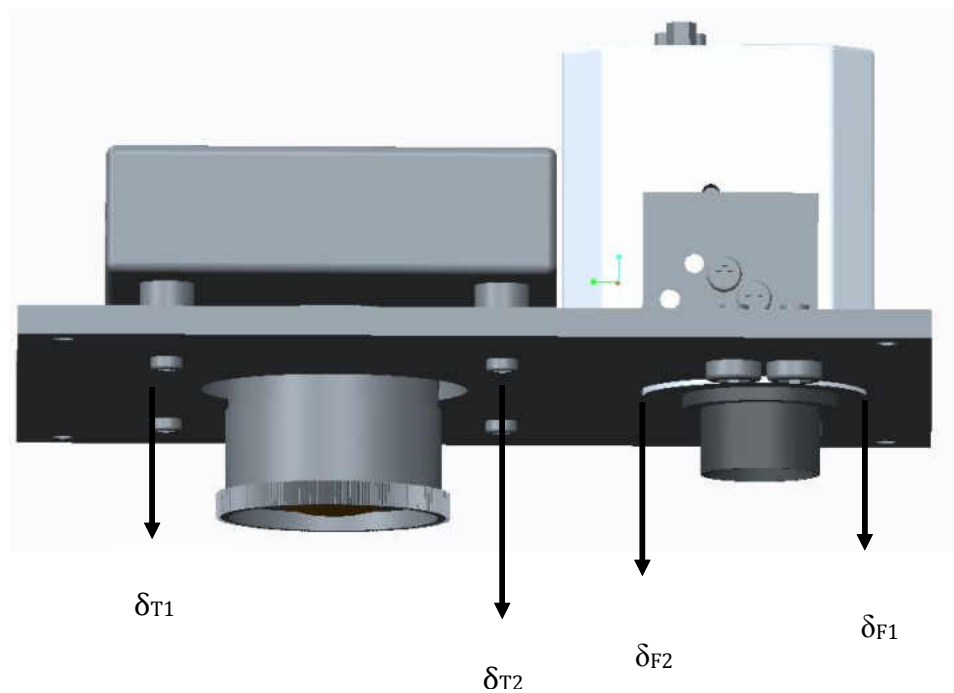


Figure 19. Deflection points at the camera edge on the mounting plate

$$\text{Net Displacement for Tetracam ADC Lite } (\delta T) = \delta_{T2} - \delta_{T1} \quad (9)$$

$$\text{Net Displacement for Flir Photon 320 } (\delta F) = \delta_{F2} - \delta_{F1} \quad (10)$$

After analyzing the deflection on effective points of the mounting plate. The net deflection of the sensor is estimated by taking the difference between the high deflection point and low deflection point shown in Figure 19 using Equation 9 and 10. The system is designed for the Super Hauler UAS platform with a payload capacity of 13.6 kilograms (30 pounds) [27]. We have certain freedom on weight limits so, the thickness of the mounting plate was increased to decrease the deflection. We can build the mounting plate using reinforcement or modify the structure to optimize the weight while reducing the deflection, it will be included in future works. In the present study, the deflection is reduced by increasing the thickness of the mounting plate. The analysis was run for aluminum plates with the standard thickness of 0.08, 0.1, 0.125, 0.16 and 0.19 inch. The thickness of the

mounting plate was kept increasing until the deflection was within acceptable limits. Figure 20 shows finite element analysis result of the deflection of the 0.19-inch mounting plate for 5g acceleration.

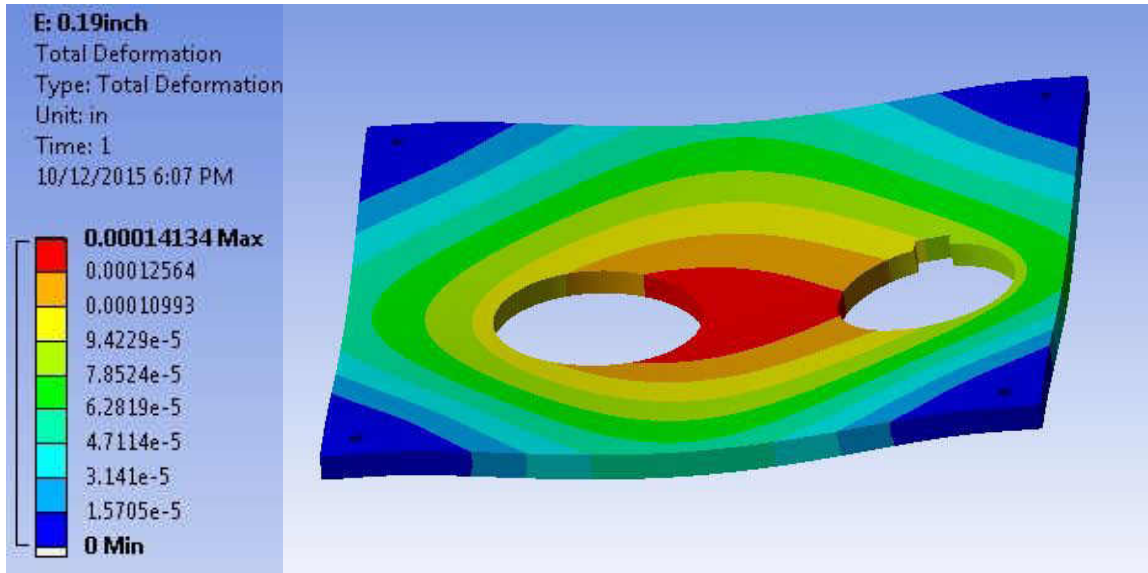


Figure 20. FEA model for deflection of 0.19-inch mounting plate

From Figure 20 we can see that the deflection is high at the middle of the mounting plate. The deflection is not symmetrical from the center in the horizontal direction of the mounting plate as shown in Figure 20 so, the Tetracam ADC lite and FLIR Photon 320 will experience different deflections at the camera edges. The net deflection for tested plate thickness is shown in Figure 21.

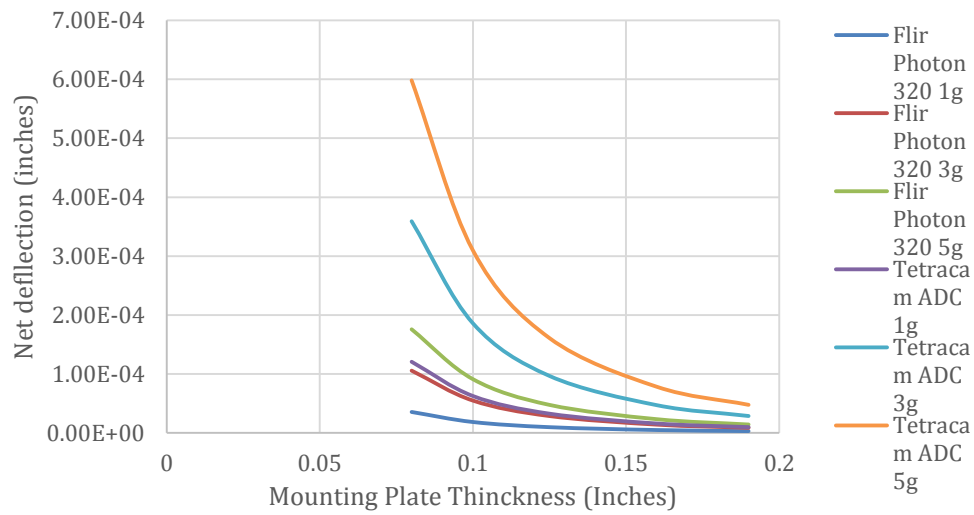


Figure 21. The net deflection of the both FLIR Photon 320 and Tetracam ADC lite on different mounting plate thickness with 1g, 3g and 5g accelerations.

From the Figure 21, we can observe that the net deflection of 0.19-inch is minimum and doesn't have a huge variation in deflection with respect to tested acceleration on both camera edge. Since the two camera FOV shifts in opposite direction the combined offset in FOV is calculated by taking the sum of individual FOV shift. The combined FOV offset is shown in Figure 22 for the 500ft elevation.

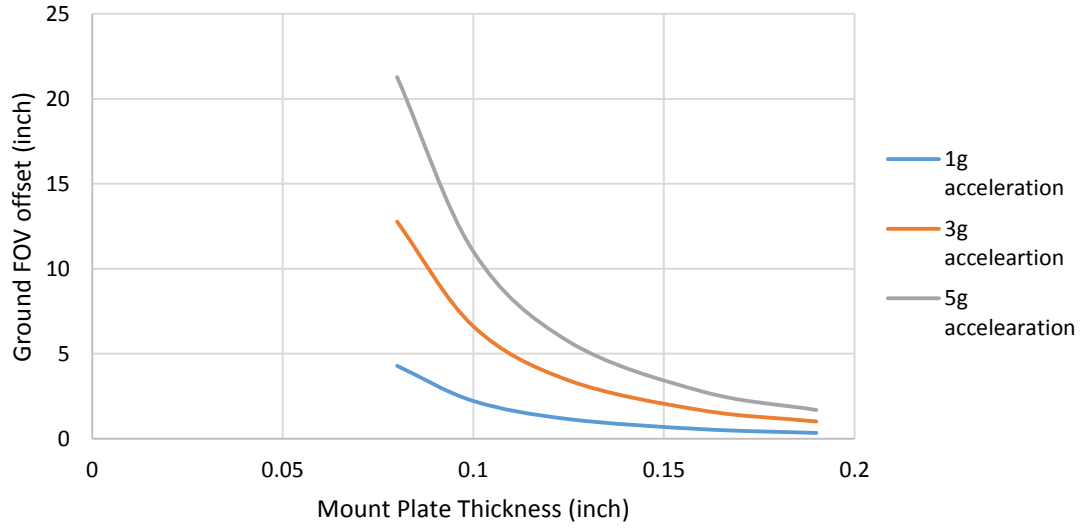


Figure 22. The net combined offset from both Tetracam ADC Lite and FLIR Photon 320 for 1g, 3g and 5g acceleration with mounting plates with different thickness at 500ft elevation.

From the Figure 22, we can observe that the FOV offset caused by the 0.08-inch thick plate at 5g acceleration is very high i.e. 21.28 inch. Large FOV offset makes it more difficult to overlap the two images and tends to misalign spatial information in single overlapped image. The 0.19-inch plate has less than 2 inches offset in FOV for maximum estimated 5g acceleration for the UAVs. So, the 0.19-inch plate was chosen for the construction of mounting plate.

### Mechanical Alignment

After mounting the two cameras side by side vertically on the mounting plate as shown in Figure 17. There is also chances of generating offset in the X direction when tightening the mounting screws of the cameras. This may lead to the skewed image when slightly over tightening the one screw with respect to other. Offset for the field of view in the Y direction is expected since the cameras were mounted with some distance in the

vertical direction. The mechanical alignment was performed to quantify and correct the actual and pixel level offset between two images for the X direction. The same scene was captured from both cameras and the central reference line of the target is selected to apply the correction method. For the tuning purpose, the mounting plate was attached to the wooden box and then fixed into the camera tripod for stable data capture method in a lab environment as shown in Figure 23.



Figure 23. Fixed stable camera system setup for tuning purpose

#### *Target Board*

Tetracam can capture images as a regular visual camera does, but for the FLIR Photon 320, a thermal gradient is needed to distinctly view the objects. So, we need the target that can be viewed by both Tetracam ADC Lite and FLIR Photon 320. To overcome this challenge the target board was designed with 48-inch  $\times$  48-inch square plywood board shown in Figure 24. The circular crosshair target pattern was painted on a white board with black enamel. To make the board visible to the infrared camera, heating wire is wrapped around the circumference of the board as well as at the intersection paths of the paints with the help of the holding screws.





Figure 24. Target board for tuning the camera alignment. Black markings are the enamel paint and the gray heating wire is wrapped around the path of the painted enamel.

#### *Tuning Method*

The tuning of the mechanical alignment was performed for a distance of 12 ft. and 100 ft. The target board was set up at a known distance. The heating wires wrapped around the target board was connected to the power outlet of 110V AC source. The Sabrent USB frame grabber was connected to the host laptop through USB port and RCA cable to view the analog video of the scene. The camera tripod was adjusted to cover the scene of the target board aligning the center of the target board to the image center. The distance between camera lens and target board was measured by using a measuring tape. Figure 25 shows the experimental setup for the demonstration of tuning process carried out in a lab environment.



Figure 25. Experimental setup for the tuning of the camera system in the lab environment.

A free version of Movavi Video Editor Software, which came along with the purchase of the Sabrent frame grabber, was used to view the analog video from both cameras. The camera tripod was set up to cover the FOV of target board aligning the center of the target at the center of the image. After aligning the field of view coverage, the trigger button was pressed at the top left corner of Tetracam ADC lite to capture the images from Tetracam ADC lite. Without disturbing the set up the still image of the analog video from the FLIR Photon 320 was taken. The two images obtained from Tetracam ADC lite and FLIR Photon 320 for the same scene are used to estimate the pixel offset for the vertical central line of the target in the X direction.

The size of Tetracam ADC lite image is  $2048 \times 1536$  and the size of the still image of FLIR Photon 320 obtained from the Movavi software is  $640 \times 480$ . For the test purpose, the image dimension the FLIR Photon 320 image was upsampled by 3.2 scale factor to

match up the with the size of Tetracam image. The images with the same size now can be overlaid on top of another to check the alignment offsets on images choosing a center line of the target board as a reference point. The MATLAB software was used to overlay the one image on top of another. Figure 26 shows the alignment of the vertical center line of the target board when overlaid Tetracam ADC lite image on top of FLIR Photon 320 infrared camera image. The center line of the target is used as the reference line since it will experience less distortion effect from the lens.

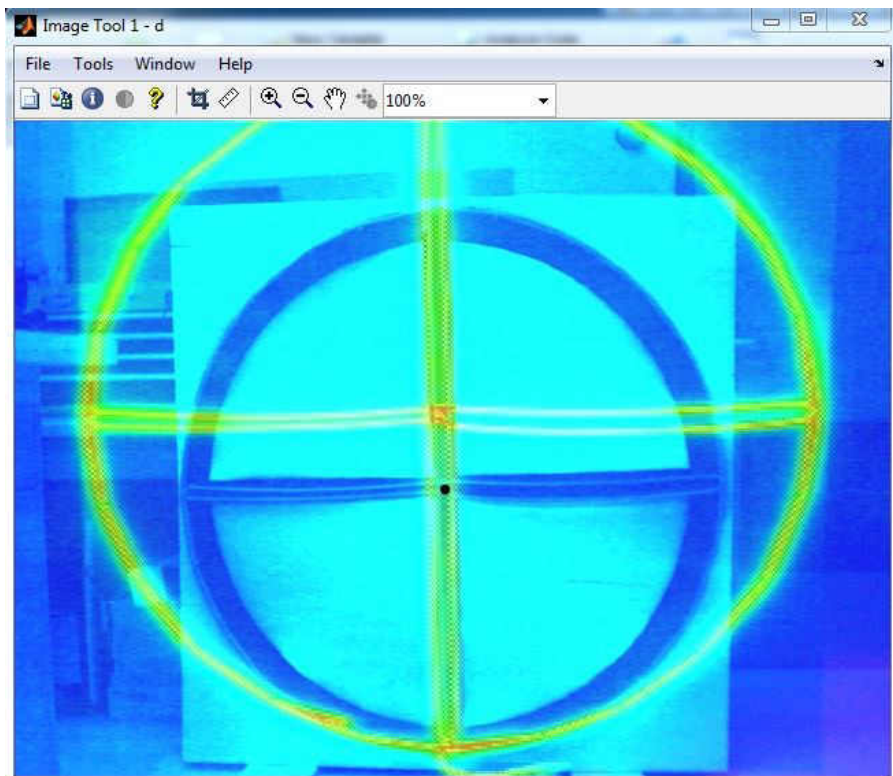


Figure 26. The overlaid images on top of another with MATLAB software showing the alignment of the vertical straight line of the target board.

The screws holding the FLIR Photon 320 camera were tightened up and loosened to a point when the vertical central line overlaps perfectly. The MATLAB image tool window was used to observe the alignment error while tuning. Which gives us the option to locate pixel points of the interested object in terms of X and Y coordinates inside the image.

## Image Registration

Image registration is a process of aligning two images by determining a spatial transformation which relates position in one image to the corresponding position in another image [45]. One image is treated as a reference image and geometric transformation is applied to another image to map with the previous image. In most practice images are taken at different time, different viewpoints and with different sensors [46]. Image registration is a crucial step to any image analysis for interpreting results from the difference between images. Image registration is mostly used in remote sensing, medical imagery and computer vision applications [46].

The mechanical alignment done in the previous section doesn't align two images spatially for the whole field of view. The field of view is dependent on the lens parameters such as focal length and angle of the view. The more the angle of view, the field of view is larger. The Tetracam ADC lite has the angle of view of  $45^\circ$  and focal length of 8 mm whereas FLIR Photon 320 has the angular field of view of  $36^\circ$  and focal length of 19mm. Both cameras create its own field of view, which doesn't cover the same portion of the environment. In order to perform the spectral image analysis, the pixel location in each of the image from the both camera must correlate with the same element in the scene. In this study, the image registration process was carried out in two steps using MATLAB software. At the first step, the affine transformation relation between two images is computed and in the second step, one image is warped to another image using the computed affine transformation matrix.

### *Affine Transformation and Image Warping*

The affine transformation is a linear transformation, which maps an object from an affine space to another; it preserves the straight lines and parallelism but changes the size, orientation and position of the object [48]. The set of affine transformation consists of various operations, a translation which shifts the object position, scaling operation, which scales up or down the original image, the shearing and rotational operation, which rotates the object [47, 48]. And the whole set of transformation is generated by a combination of all transformation which is affine transformation. The affine transformation matrix consists of 6 parameters.

$$T = \begin{bmatrix} a_{11} & a_{12} & T_x \\ a_{21} & a_{22} & T_y \end{bmatrix}$$

Where  $a_{11}$ ,  $a_{12}$ ,  $a_{21}$  and  $a_{22}$  are composed of scaling, shear and rotational parameters,  $T_x$  and  $T_y$  represents the translation between corresponding points [47]. Since the size of affine transformation matrix is  $2 \times 3$  and image points are 2D vector, we cannot implement the matrix multiplication. The problem is extended to 3 dimensions by use of homogeneous coordinate system [48]. It relies on adding a dimension to the working space to be able to perform transformations using matrices. To convert the Cartesian coordinates to homogeneous coordinate system a third component 1 is added to every image points and row of  $[0 \ 0 \ 1]$  to the affine transformation matrix.

$$X = \begin{bmatrix} x \\ y \end{bmatrix} \longrightarrow X_h = \begin{bmatrix} x \\ y \\ 1 \end{bmatrix}$$

$$T = \begin{bmatrix} a_{11} & a_{12} & T_x \\ a_{21} & a_{22} & T_y \end{bmatrix} \longrightarrow T_h = \begin{bmatrix} a_{11} & a_{12} & T_x \\ a_{21} & a_{22} & T_y \\ 0 & 0 & 1 \end{bmatrix}$$

Let the source image point is represented by column vector  $X$  and the target image point be represented by column vector  $X'$ . The geometric transformation relation can be represented by the Equation 11.

$$\begin{bmatrix} x' \\ y' \\ 1 \end{bmatrix} = \begin{bmatrix} a_{11} & a_{12} & T_x \\ a_{21} & a_{22} & T_y \\ 0 & 0 & 1 \end{bmatrix} \begin{bmatrix} x \\ y \\ 1 \end{bmatrix} \quad (11)$$

We have 6 unknown parameters so we need 3-point correspondence or similar landmarks in source and target images in order to solve for transformation matrix. Using the 3-point correspondence  $(x_1, y_1)$   $(x'_1, y'_1)$ ,  $(x_2, y_2)$   $(x'_2, y'_2)$  and  $(x_3, y_3)$   $(x'_3, y'_3)$  to solve affine transformation matrix we get.

$$\begin{bmatrix} x'_1 \\ y'_1 \\ x'_2 \\ y'_2 \\ x'_3 \\ y'_3 \end{bmatrix} = \begin{bmatrix} x_1 & y_1 & 1 & 0 & 0 & 0 \\ 0 & 0 & 0 & x_1 & y_1 & 1 \\ x_2 & y_2 & 1 & 0 & 0 & 0 \\ 0 & 0 & 0 & x_2 & y_2 & 1 \\ x_3 & y_3 & 1 & 0 & 0 & 0 \\ 0 & 0 & 0 & x_3 & y_3 & 1 \end{bmatrix} \begin{bmatrix} a_{11} \\ a_{12} \\ T_x \\ a_{21} \\ a_{22} \\ T_y \end{bmatrix} \quad (12)$$

In general, 3 pairs of the landmarks are sufficient for solving the transformation matrix. The choice of the landmarks is crucial for the determination of affine transform. In order to increase the alignment accuracy globally more than 3 landmarks were chosen to get the overdetermined system and solved using the linear least square error method in MATLAB. Figure 27 shows the selection of control points in two images to solve the affine transformation.

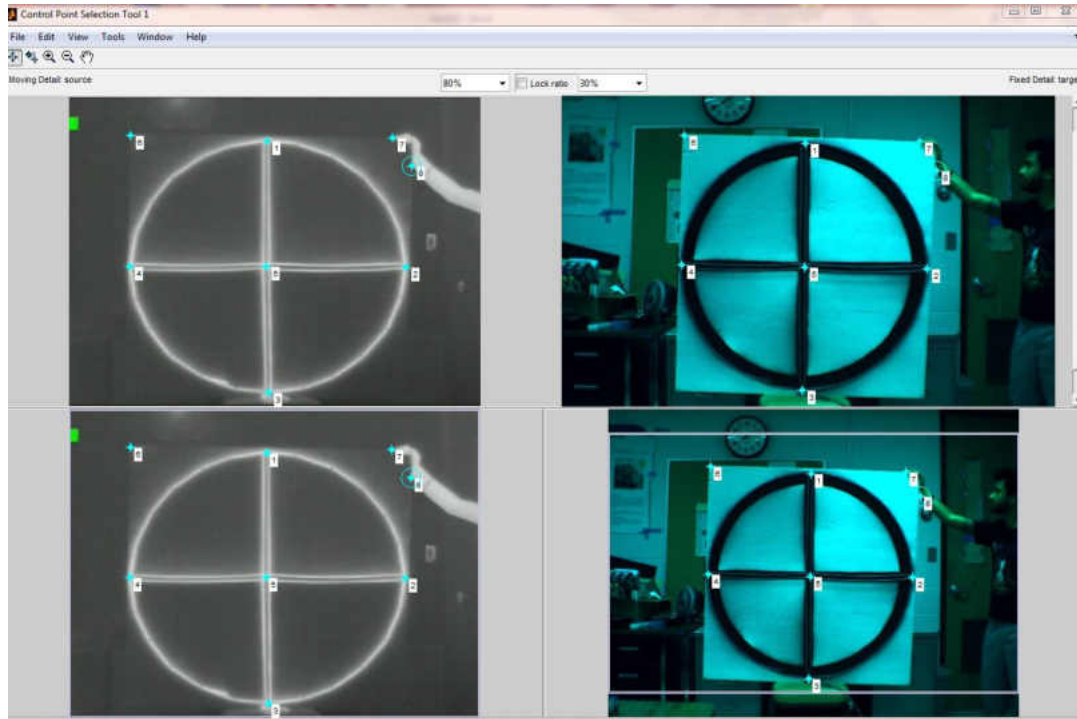


Figure 27. Control points (landmarks) selection for computing affine transformation matrix. Image at left is a source image and image at right side is target image

After estimating the affine transformation matrix from the point correspondences, the source image is mapped to the target image through image warping method implemented in MATLAB software. Image warping is a process of moving each pixel location from one image to the other image determined by the transformation matrix [48]. There are two types of image warping method one is forward warping and another is inverse warping. In forward warping process, for any source Image  $I(x)$  the new image  $I'(x')$  is generated by copying each pixel of the source image to its corresponding location [48] determined by  $[X'] = [T] [X]$ .

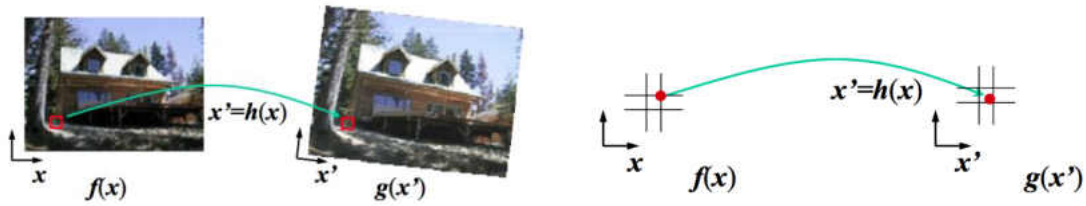


Figure 28. Forward warping algorithm illustration [48]

Although the forward warping is generic it suffers from different limitations such as generation of cracks and holes while magnifying the warped image [48]. If warped image coordinate has a non-integer value, correcting it by rounding off to nearest coordinate or using splatting process to distribute its value to nearest four neighbors will further lead to blurring and aliasing [48]. So, we used the inverse warping method to eliminate these issues. In inverse warping process, every pixel ( $x'$ ) in destination image  $I'(x')$  is sampled from its corresponding location  $[X]$  defined by  $[X] = [T^{-1}] [X']$  in source image  $I(x)$  [48].

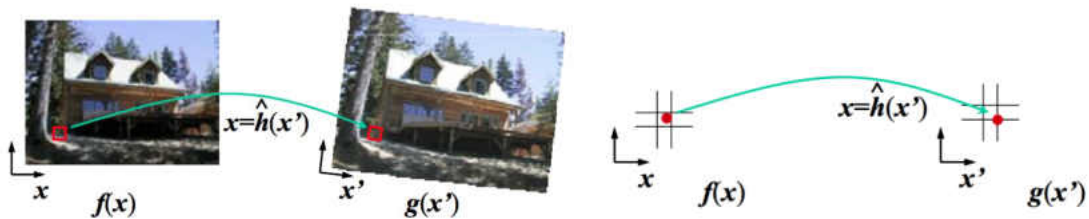


Figure 29. Inverse warping algorithm illustration [48]

If there are non-integer pixel locations the interpolation is carried out to resample that pixel from its neighboring pixels. Figure 30 shows the FLIR Photon 320 original and warped image using the affine transformation matrix obtained from point correspondences.



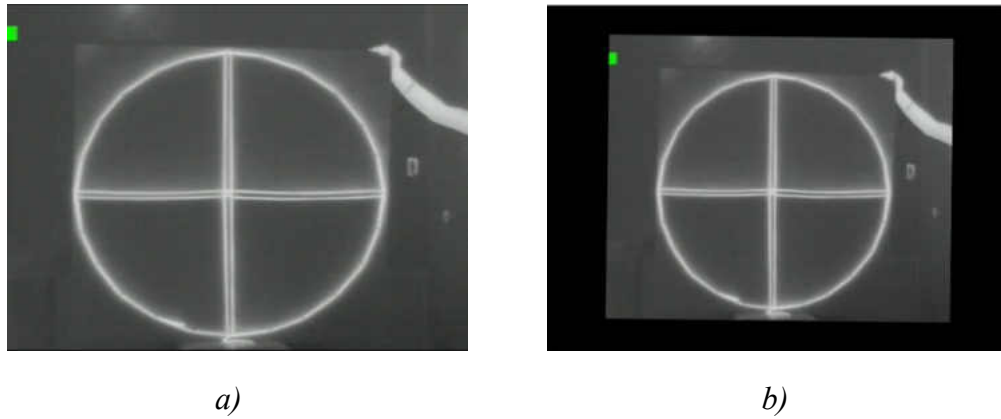


Figure 30. FLIR Photon 320 image of target board *a)* original image *b)* warped image using affine transformation matrix.

The warped FLIR Photon 320 image was overlaid on top of Tetracam ADC Lite image to check the registration process shown in Figure 31.

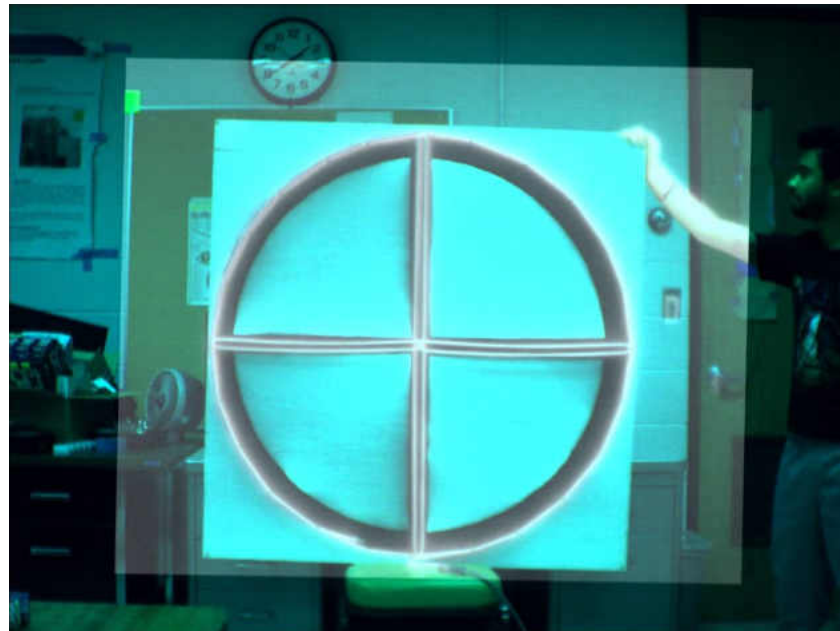


Figure 31. Overlaying of Tetracam image and warped image of the FLIR Photon 320.

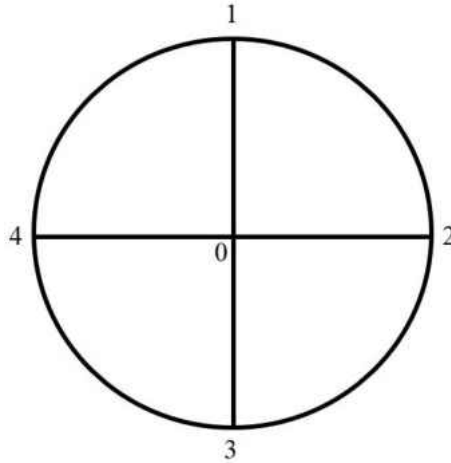


Figure 32. Target board showing reference points for measuring pixel offset

The alignment performed by the image registration was verified for the selected landmarks as shown in Figure 32. O represents the center of the circular pattern, 1, 2, 3 and 4 represents the top, right, bottom and left edge points of the circular pattern. The pixels offset in reference points of the registered image is shown in Table 4.

Table 4. Pixel offsets at control points of the circular pattern for comparing Tetracam image and warped FLIR image.

Control Points	Tetracam Image	Warped FLIR Image	Pixel offset
Center point O	(1006, 832)	(1008, 826)	(0, 2)
Edge point 1	(1010, 314)	(1010, 314)	(2, 6)
Edge point 2	(1518, 836)	(1518, 836)	(2, 2)
Edge point 3	(1000, 1346)	(1000, 1346)	(4, 2)
Edge point 4	(498, 826)	(498, 824)	(0, 5)

### Camera Calibration

The camera calibration is the process of estimating the internal camera geometrics and lens characteristics [48]. In the machine vision application, the camera calibration is very essential for the precision. The wide-angle lenses used in the cameras have some sort

of the distortion due to the poor lens quality and misalignment of the lens with respect to the camera sensor [48, 49]. Mainly there are two types of image distortion coming out from the camera which are radial and tangential distortion.

We want to minimize the image alignment error due to the distortion of the image scene. The camera calibration is a widely used method to find the intrinsic and extrinsic camera parameters along with distortion coefficients which give us the opportunity to rectify the distorted camera images [48-52]. In this study, camera calibration was performed using pre-built camera calibration toolbox for MATLAB developed by Bouguet [49].

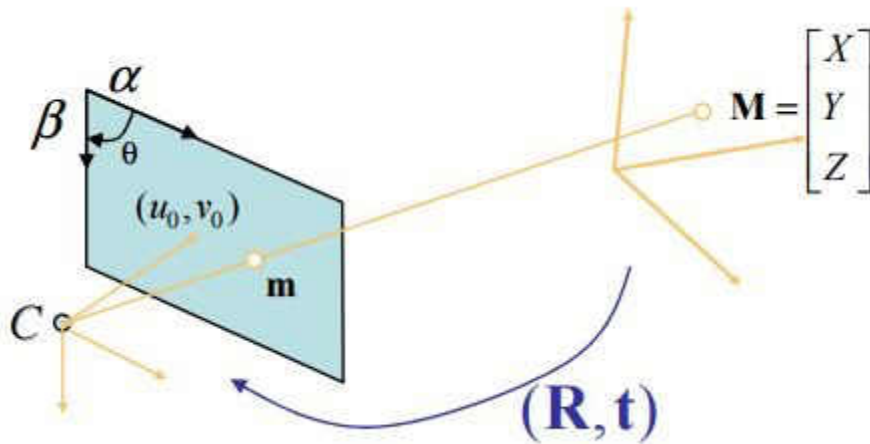


Figure 33. Pinhole camera model [53].

Camera calibration uses the pinhole model based upon the principle of collinearity, where each 3D point of the object in the world space is projected to the image plane using perspective transformation [50]. In Figure 33  $M$  represents the coordinate of a 3D point in the world coordinate space,  $m$  is the image point of  $M$  mapped into the image plane.  $C$  represents the center of camera reference frame.  $u_0$  and  $v_0$  represents the center of image

plane. The mapping of object point  $M$  in 3D world coordinate to its corresponding image point  $m$  in the image plane can be related as

$$m = K [R \ t] M \quad (13)$$

$$\begin{bmatrix} u \\ v \\ 1 \end{bmatrix} = \begin{bmatrix} f_x & \alpha_c & u_0 \\ 0 & f_y & v_0 \\ 0 & 0 & 1 \end{bmatrix} \begin{bmatrix} r_{11} & r_{12} & r_{13} & t_1 \\ r_{21} & r_{22} & r_{23} & t_2 \\ r_{31} & r_{32} & r_{33} & t_3 \end{bmatrix} \begin{bmatrix} X \\ Y \\ Z \\ 1 \end{bmatrix} \quad (14)$$

Where  $[R \ t]$  is an extrinsic parameter which consists of rotation and translation vector that transforms object point  $M$  to the camera reference frame.  $[K]$  is the intrinsic camera matrix which contains focal lengths  $(f_x, f_y)$ , principal points  $(u_0, v_0)$  expressed in pixel dimension and skew coefficient  $\alpha_c$ . Intrinsic matrix  $[K]$  projects the object from camera reference frame to the image plane [50].

The pinhole camera model is solved by Direct Linear Transformation (DLT) method developed by Abdel- Aziz and Karara [54]. The pinhole camera model ignores the radial and tangential distortion induced by lens [50-52]. The camera model used in the camera calibration toolbox for MATLAB is derived by adding radial and tangential distortion component induced by camera lens to the pinhole model [52]. The camera calibration toolbox for MATLAB uses the similar nonlinear camera model used by Heikkil and Silven including radial and tangential distortion parameters [49].

Let  $P$  be the point in camera center coordinate denoted by  $\begin{bmatrix} X_c \\ Y_c \\ Z_c \end{bmatrix}$  then the normalized

pinhole image projection can be represented as  $x_n = \begin{bmatrix} X_c/Z_c \\ Y_c/Z_c \end{bmatrix} = \begin{bmatrix} x \\ y \end{bmatrix}$  having origin at the principal point. Including the radial and tangential distortion model as proposed in [55-57]

to the normalized point coordinate we have distorted points denoted by Equation 16 and 17.

$$\text{Let } r^2 = x^2 + y^2 \quad (15)$$

$$x' = x[1 + k_1 r^2 + k_2 r^4 + k_3 r^6] + 2k_4 xy + k_5(r^2 + 2x^2) \quad (16)$$

$$y' = y[1 + k_1 r^2 + k_2 r^4 + k_3 r^6] + k_4(r^2 + 2y^2) + 2k_5 xy \quad (17)$$

Where  $k_1, k_2$  and  $k_3$  are the radial and  $k_4, k_5$  are tangential distortion coefficients.  $x$  and  $y$  are distortion free pixel location in normalized image coordinates while  $x'$  and  $y'$  are distorted normalized coordinates.  $x$  and  $y$  are dimensionless parameters measured from the principal point. Once the distortion model is implemented the final distorted image pixel coordinates  $u'$  and  $v'$  can be represented as Equation 18 [49].

$$\begin{bmatrix} u' \\ v' \\ 1 \end{bmatrix} = [K] \begin{bmatrix} x' \\ y' \\ 1 \end{bmatrix} \quad (18)$$

This nonlinear camera model is solved using a least-square method by applying the iterative algorithm and the solution is optimized using Levenberg- Marquardt optimization method [50]. The parameters obtained from the linear pin-hole camera model, solved by DLT in the first phase of the camera calibration are used as the initial values for the iteration [50].

In the calibration process, several images (around 20 images) of the checkerboard pattern were taken at different orientations and locations. The images of the checkerboard pattern were loaded to the camera calibration toolbox for MATLAB and the corner extraction were performed for all of the captured images. After the corner extraction, the

camera was calibrated. The output of the camera calibration toolbox for MATLAB result consists of camera's lens focal length ( $f_c$ ), principal point ( $c_c$ ) in pixel unit, skew coefficient ( $\alpha_c$ ) defining the angle between x and y pixel, image distortion coefficients ( $k_c$ ) with estimated uncertainties and reprojection error ( $err$ ) [49]. These parameters allow calibration toolbox to visualize the distortion model and to correct the distortion [49]. The Camera calibration toolbox for MATLAB offers a function that allows the undistortion of the distorted images in batch using the parameters obtained from the camera calibration process.

#### *Tetracam ADC Lite Calibration*

Camera calibration of the Tetracam ADC lite is similar to the calibration of the general camera with visible bands. The images obtained from the Tetracam are very distinct and have good contrast at the edges of the checkerboard pattern. Several images of a checkerboard pattern in different orientations and locations were taken from the Tetracam ADC lite. The images were color processed using Pixel Wrench 2 software to convert RAW image to the JPG format. The color processed images were used as the input images for the calibration process.



Figure 34. Calibration images used for the Tetracam ADC lite camera calibration

The results obtained from the calibration of the Tetracam ADC lite with uncertainties is listed in Table 5.

Table 5. Tetracam ADC lite camera calibration results containing estimated camera parameters, uncertainty on parameter estimation with three times standard deviation and coefficient of variation.

Camera Parameters	Estimated Value	Uncertainty ( $\pm 3\sigma$ )	Coefficient of Variation (%)
Focal Length ( $f_c$ )	(1947.38415, 1949.11323)	$\pm$ (2.34114, 2.21427)	0.04%, 0.04%
Principal Point (cc)	(978.74104, 775.70159)	$\pm$ (2.41585, 3.57717)	0.08%, 0.15%
Skew Coefficient ( $\alpha$ )	0.00000	$\pm$ 0.00000	0%
Distortion Coefficient ( $k_c$ )	(-0.20925, 0.20271, 0.00203 0.00201, 0.00000)	$\pm$ (0.01850, 0.017086, 0.00100 0.00075, 0.00000)	2.95%, 2.81%, 16.42%, 16.58%, 0%
Reprojection error (err)	0.34381 0.33906		

As we can observe in Table 5 the uncertainty of the estimation of the focal length, principal point and distortion coefficient is significantly low with a small coefficient of variations. Since the variability of the estimated parameters is low, we can accept the estimated parameter with high confidence. Figure 35 shows the visualization of the distortion in the Tetracam image.

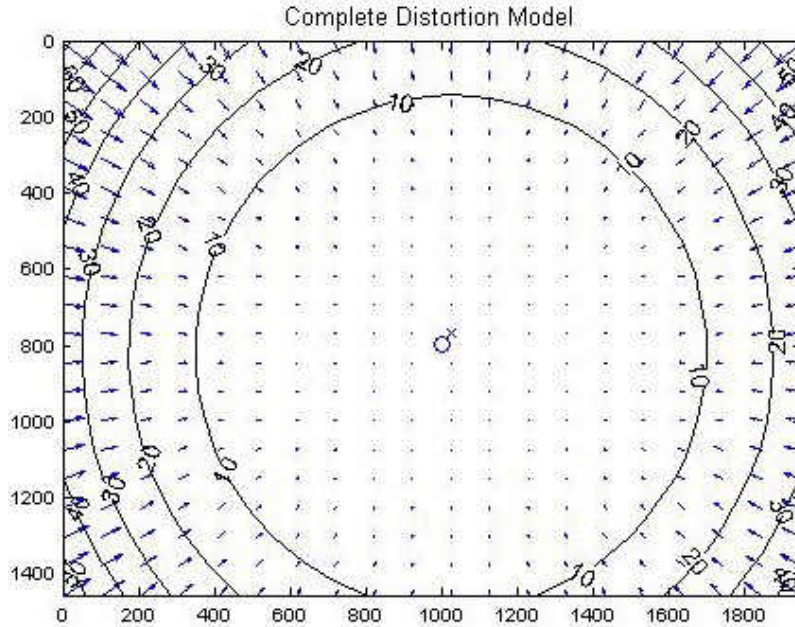


Figure 35. A plot showing the distortion model of the Tetracam ADC lite. Arrows in the model represent the direction and magnitude of the distortion across the image plane

The plot in Figure 35 shows the complete distortion model composed of radial and tangential distortion on each pixel of the image. The camera lens shows the barrel distortion effect. Each arrow in the distortion model represents the direction and effective displacement of a pixel induced by the lens distortion. This causes the distorted image to expose inaccurate representation of the real scene. The points in the corner of the model are displaced by as much as 50 pixels. The cross in the model represents the center of the image and circle indicates the location of the principal point. Figure 36 compares how the distorted image has the curved line representation for the straight line in the real world at the picture *a)*, as compared to rectified image at *b)*. Distorted image *c)* shows the slightly more scene in the image than the rectified image in image *d)*.





a)



b)



c)



d)

Figure 36. Image a) and c) are distorted image b) and d) are undistorted image of Tetracam ADC lite multispectral camera

### *FLIR Photon 320 Infrared Camera Calibration*

The checkerboard pattern made of paper only has visual contrast but the infrared camera works on the principal of thermal radiation [26]. In this research, we used the aluminum sheet and paper to construct the checkerboard pattern shown in Figure 37. Aluminum sheets were attached on the top of the black squares of the checkerboard pattern. Our main goal is to create the thermal gradient on the edges of the square grids of the checkerboard. The main reasoning is based upon the large difference in the thermal

properties of the paper and aluminum shown in Table 6. The object with higher temperature emits high magnitude of the infrared radiation than the cold objects, which helps to identify the hot and cold objects in the image. Also, the infrared radiation is dependent upon the emissivity of the materials. The materials surface with high emissivity emits higher infrared radiation than others for same temperature [26]. In this research, we are not focused on quantifying the amount of radiation of materials. We will be using any one of the thermal properties listed in Table 6, which will provide the better image with a thermal gradient, and makes a checkerboard pattern visible. The thermal properties of the aluminum and paper are shown in Table 6.

Table 6. Thermal properties of aluminum and paper [58]

Material	Thermal Conductivity (W/ mK)	Emissivity ( $\epsilon$ )
Aluminum	205	0.04
Paper	0.05	0.93



Figure 37. Calibration Checkerboard pattern made with aluminum foil sheet and paper

When images of checkerboard made with aluminum and paper were taken at the same temperature. There were very few distinct recognizable checkerboard patterns. It was very hard to predict any changes at the edges of the square boxes. In this case, the

emissivity property was not sufficient to create high contrast image. So, we planned to move on to use the thermal conductivity properties to see if it gives us the distinct image. As shown in Table 6 the thermal conductivity of the aluminum is 205 W/mK which is significantly higher than the thermal conductivity of paper i.e. 0.05W/mK. So aluminum square sheet will gain or lose heat faster than the paper and changes its temperature faster than paper.

To obtain the temperature difference with the ambient air the checkerboard was kept inside the refrigerator to lower down the temperature. After 30 minutes the checkerboard pattern was taken out of the refrigerator. The aluminum square pattern started to gain the heat energy from the ambient air faster than the paper. When observed through the FLIR Photon 320 video display the more distinct pattern was identified than the previous method. Several images of the checkerboard pattern were captured in different locations and orientations before the temperature gradient decreases. Figure 38 shows the images taken using emissivity property at ambient temperature and thermal conductivity properties of the materials.

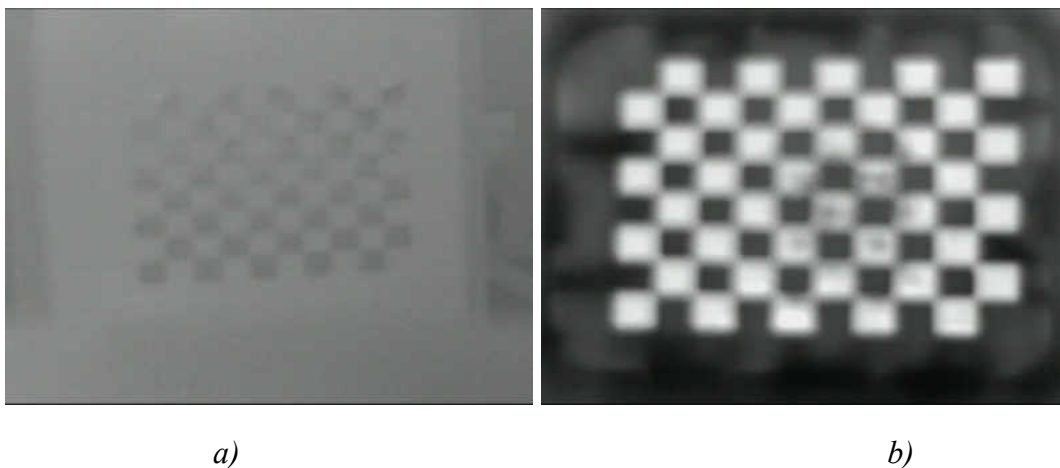


Figure 38. Image of the checkerboard at ambient temperature (left). Image of the checkerboard at ambient temperature after sitting 30 minutes in the refrigerator (right)

The images of the refrigerated checkerboard pattern at ambient air were input in the Camera Calibration Toolbox for MATLAB. The corner extraction was possible but the detected corners were not located precisely with the real chessboard pattern corners. Corner detection is a crucial step to obtain the precise calibration parameters. Since the corners were not located with high precision the estimated camera parameters have high uncertainties. Figure 39 shows the corner extraction picture with automated detection of the number of squares in the checkerboard pattern.

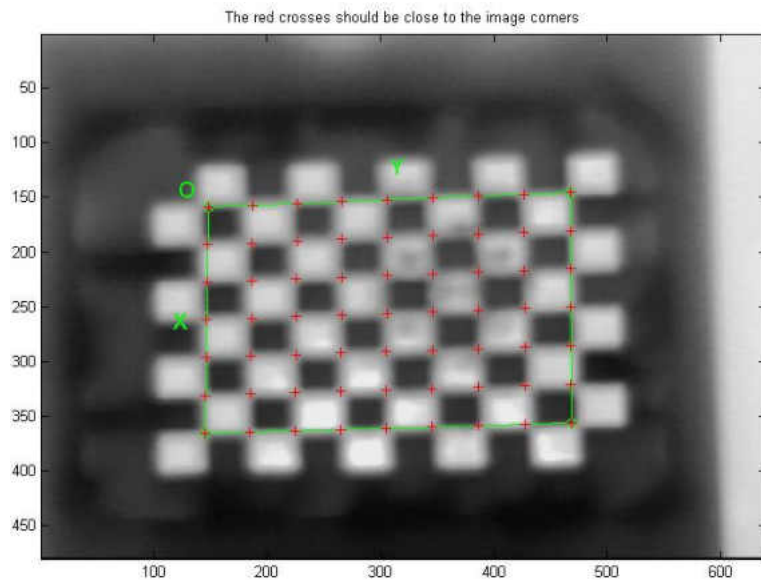


Figure 39. FLIR Photon 320 checkerboard image showing the corner extraction performance during camera calibration process.

The camera calibration output results obtained from the infrared images is shown in Table 7.

Table 7. FLIR Photon 320 infrared camera calibration results containing estimated camera parameters, the uncertainty of parameter estimation with three times standard deviation and coefficient of variation.

Camera Parameters	Estimated Value	Uncertainty ( $\pm 3\sigma$ )	Coefficient of Variation (%)
Focal Length ( $f_c$ )	(1022.26695, 899.11938)	$\pm$ (79.41889, 76.50663)	2.58%, 2.83%
Principal Point ( $c_c$ )	(304.79702, 210.99281)	$\pm$ (66.80182, 29.39096)	7.30%, 4.64%
Skew Coefficient ( $\alpha$ )	0.00000	$\pm$ 0.00000	0%
Distortion Coefficient ( $k_c$ )	(-0.08119, 1.47336, -0.00922, 0.00407, 0.00000)	$\pm$ (0.19456, 2.46594, 0.01441, 0.01563, 0.00000)	79.87%, 55.79%, 52.09%, 128%, 0%
Reprojection pixel error (err)	1.56967, 1.51396		

The uncertainty in the estimation of the focal length and principal point for the FLIR Photon 320 is very high as compared to the uncertainty obtained in the calibration of the Tetracam. The coefficient of variation is very high for the estimation of the distortion coefficients which ranges from 55.79% to 128%. The camera calibration toolbox for MATLAB algorithm was able to detect the number of squares perfectly but the images didn't have high contrast to precisely detect the corners of the checkerboard pattern as shown in Figure 39.

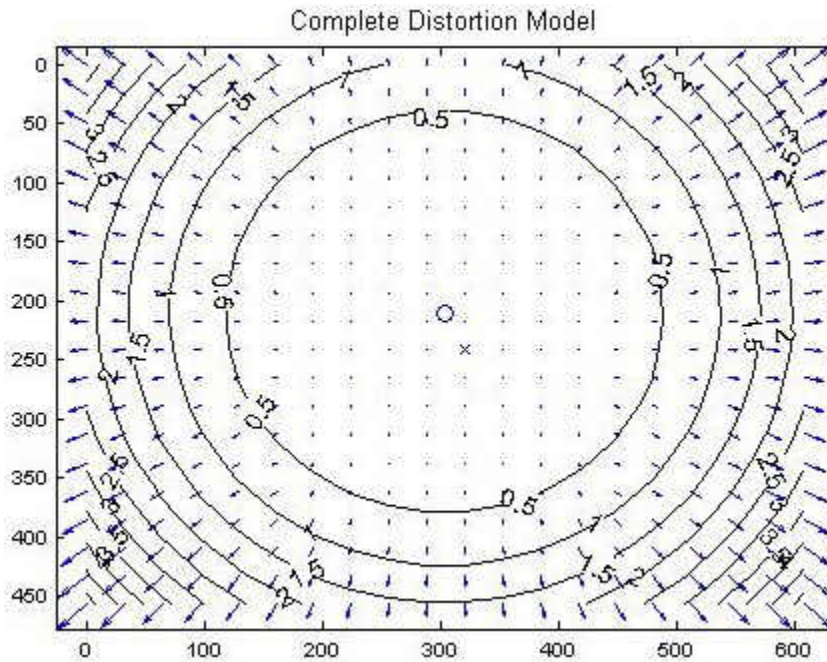


Figure 40. FLIR Photon 320 Complete Distortion Model

The complete distortion model of the FLIR Photon 320 in Figure 40 shows the camera lens seemed to have pincushion distortion. The points in the corner of the model are displaced by as much as 5 pixels away from the center of the image. The cross in the model represents the center of the image and circle represents the estimated location of principle points. The center points and principal points have large offsets. Overall the distortion model shows the parameters obtained from the calibration has huge offsets and uncertainties as compared to the Tetracam calibration parameters. Due to the large uncertainties in the estimated parameters, a further test is performed to check the undistortion performance from the obtained camera parameters.

The original distorted and undistorted image output from the camera calibration toolbox for MATLAB were compared to see the performance of the rectification. The original distorted image *a)* shown in Figure 41 seemed better than the rectified image *b)*.

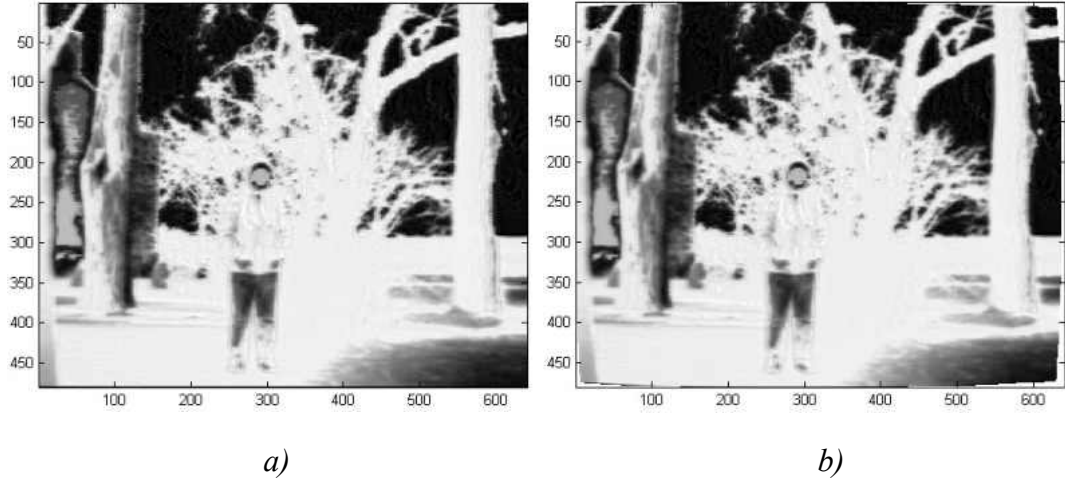


Figure 41. *a)* Original FLIR Photon 320 image *b)* Rectified image from the camera calibration parameters

*Straight Line Test for Undistorted FLIR Photon 320 Image*

The straight line test was performed on the FLIR Photon’s original distorted and undistorted image output from camera calibration toolbox for MATLAB. The image of the board wrapped with heating wire in a square configuration was used for the test. Figure 42 shows the original distorted and undistorted image output from camera calibration toolbox for MATLAB for FLIR Photon 320.

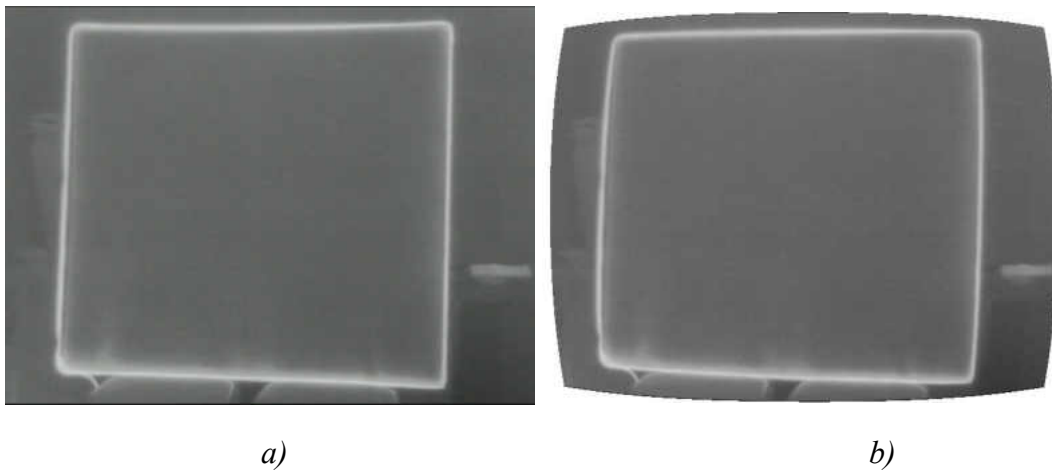


Figure 42. *a)* Original image from the FLIR Photon 320. *b)* Undistorted FLIR Photon 320 infrared image from Camera Calibration Toolbox for MATLAB

The straight lines of the heating wire in square configuration were made reference lines to predict the undistortion performance. The straight line test was carried out using linear least square error fitting of the line. Initially, straight line of the heating wire was segmented as white and rest of the image as black using Canny edge detection method [59] implemented in MATLAB. Figure 43 shows the edge detected images with heating wire lines in the white color.

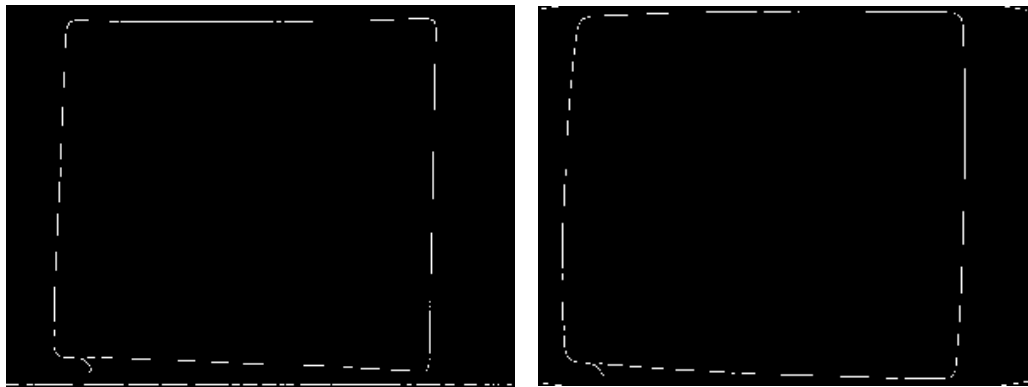


Figure 43. Edge detected FLIR Photon 320 infrared images

The two corner points of the heating wire lines in the image were selected to perform the line test. At first, the equation of the line was computed using the coordinates of the two selected corner points. The line equation was used to get the new values of the Y coordinates based upon the original X coordinates. The coefficient of determination ( $r^2$ ) was computed using the new and old Y coordinates to test the goodness of fit for the line. The line test was performed for all four lines of the square and compared with the original distorted images from FLIR Photon 320 camera. The coefficient of determination ( $r^2$ ) for the line test is shown in Table 8.



Table 8. Coefficient of determination ( $r^2$ ) of the line test

Lines	Original Distorted Image	Undistorted Image from Camera Calibration Toolbox
Top	0.6518	0.5625
Right	0.9808	0.6662
Bottom	0.9865	0.9534
Left	0.9831	0.8898

From Table 8 we can see that the coefficient of determination ( $r^2$ ) of the original distorted image on the right, bottom and left is higher than 0.98 close to 1 which concludes the line is straight and predicts the linear model with a good fit. Whereas the coefficient of determination ( $r^2$ ) of the undistorted image at the right line is 0.6662, this indicates the line fit is not good. The left and the bottom line have  $r^2$  of 0.8898 and 0.9534 which is less than original distorted image. In the top line, the distorted original image has  $r^2$  of 0.6518 which is still greater than the undistorted image  $r^2$  of 0.5625. This both line fit represents a poor fitting but the applied undistortion seems to reduce the fit.

These observations show that the distortion corrected image obtained from the camera calibration toolbox for MATLAB for FLIR Photon 320 is not as good as the original distorted image. The correction applied from camera calibration toolbox for Matlab didn't improve the rectification performance. The undistortion performance should have been better if highly contrast images were captured and used for calibration. The absence of high contrast edges at the checkerboard pattern caused bad corner extraction and high uncertainty in the estimation of the camera parameters. So the rectification process for the FLIR Photon 320 infrared images is excluded in this project. There are other recommended methods for improving the camera calibration which can be applied to the calibration method.

The center calibration method using circular or ring calibration pattern can be tested for FLIR Photon 320 in future work to improve the calibration instead of using the square checkerboard pattern. The precise localization of control points is essential for improving the camera calibration. Even small error in estimating the control points may lead to imprecise calibration [60-62]. The iterative control point refinement method can be used to detect the control points more precisely as proposed by Datta et al [60]. This approach improves the control point estimation by performing undistortion and unprojection of calibrated images to the canonical plane. The parameters obtained from the camera calibration is used as an initial parameter for the iteration. The plane is then used to localize the calibration pattern control points and recompute the camera parameters in an iterative refinement until convergence [60]. The undistortion of the FLIR Photon 320 image is excluded in this research and will be considered for the future work. However, the undistortion of the Tetracam images was performed.

## CHAPTER V

### SYSTEM INTEGRATION AND DATA COLLECTION

#### System Integration

The Tetracam ADC lite multispectral camera can capture the images and store in the CompactFlash (CF) storage card. It offers three image formats RAW 8 bit, RAW 10 bit and DCM 10 [22]. The full capture, process and storage time is different for all three image formats. RAW 8 bit is the fastest data capture format with average 3 seconds per image. On the other hand, for the same image format, the Tetracam ADC lite multispectral camera tends to vary time in the data capture process [22]. FLIR Photon 320 displays real time analog video [23]. It doesn't have a storage feature in its own system. One of the solution to acquire images from the FLIR Photon 320 infrared camera is to take the still images from the video. The Sabrent USB Video capture device makes it possible to connect the analog video from FLIR Photon 320 to the Odroid U3 single board computer through USB and RCA interface. FFMPEG software installed in Odroid U3 Linux Operating System helps to capture real-time still images.

The time for capturing the images from the FLIR Photon 320 is extremely quick due to its low resolution and small data size JPEG format. The basic concept of integration of two cameras is taking the images from the Tetracam by triggering the camera and at the same time taking still images from the FLIR Photon 320.

Individual operation of the two cameras has a serious issue in time lapse due to the fluctuation of the Tetracam ADC lite data capture process. The small time lapse between two camera's operations will make a huge effect on the capture of the same scene since the images are taken from the moving UAS. For obtaining quality data, we need to capture the images from both cameras at same exact time and location. To overcome this timing issue the two cameras are integrated using Tetracam ADC lite as the master and FLIR Photon 320 as a slave configuration. The block diagram of the connection of the components in the payload is shown in Figure 44.

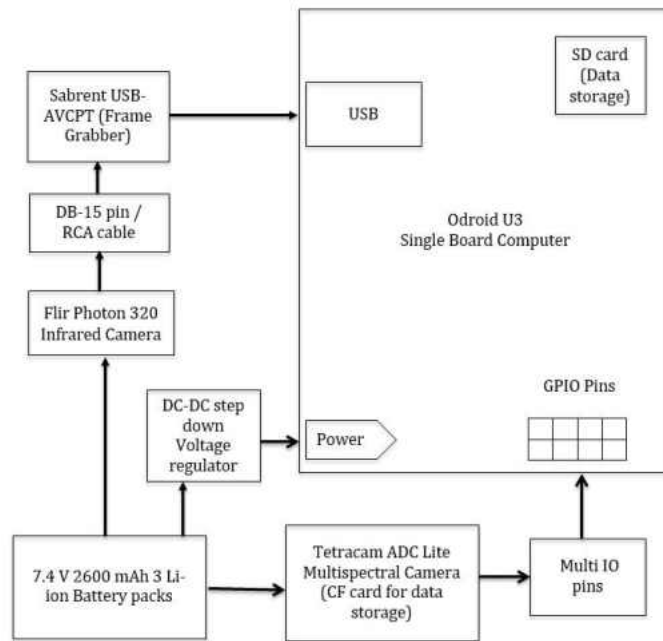


Figure 44. Block diagram showing the physical connection of the equipment in the integrated payload.

The Tetracam ADC lite offers an internal 15-Pin flat edge Multi I/O connector for the external control of the device shown in Figure 45. Pin 9 of the Multi I/O pin responses high logic of 3.3V when the camera is triggered and keeps maintaining 3.3 Volt until the data is fully stored. In the ideal state the Pin 9 voltage remains at 0 Volt [63]. This feature

offers a good opportunity to monitor the Tetracam ADC Lite's operational status. This logic was used to send Tetracam ADC lite status signal to the single board computer.

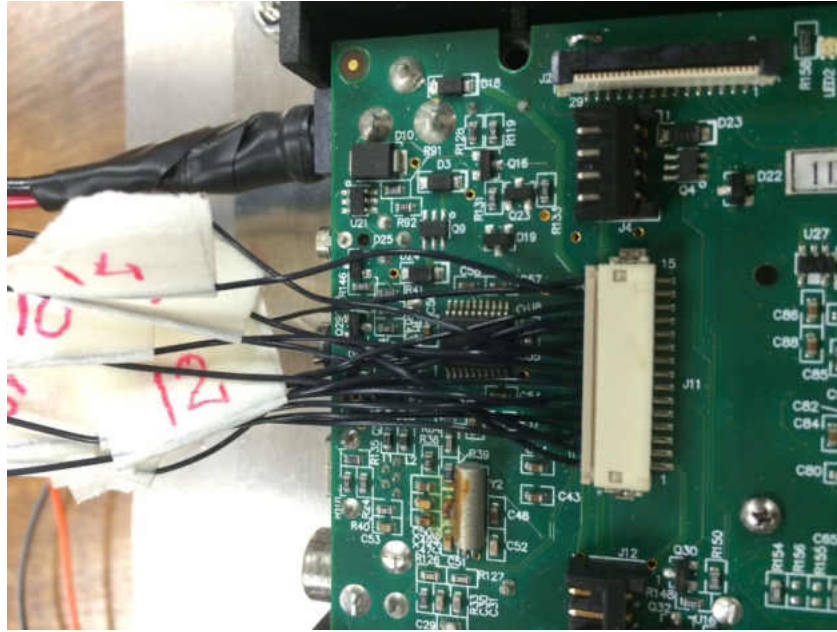


Figure 45. 15-Pin Flat edge Multi I/O connector located inside the Tetracam ADC lite.

The single board computer Odroid U3 offers 3 General Purpose Input Output (GPIO) pins along with 1.8V, 5V outputs and one ground as shown in Figure 46 [37]. GPIO pins can be configured as input and also as output. It can read the value of the one digital signal. When configuring GPIO as an input it converts voltage being delivered to the pin as a logical interpretation of 0 and 1. When it receives the high voltage relatively greater than ground it reads logic 1 and when a voltage is equal to ground it reads logic 0 [64]. One of the GPIO (#204) was used to input the signal from Pin 9 of the Tetracam ADC lite. These GPIO pins can be configured or controlled to relate the logic to specific tasks.

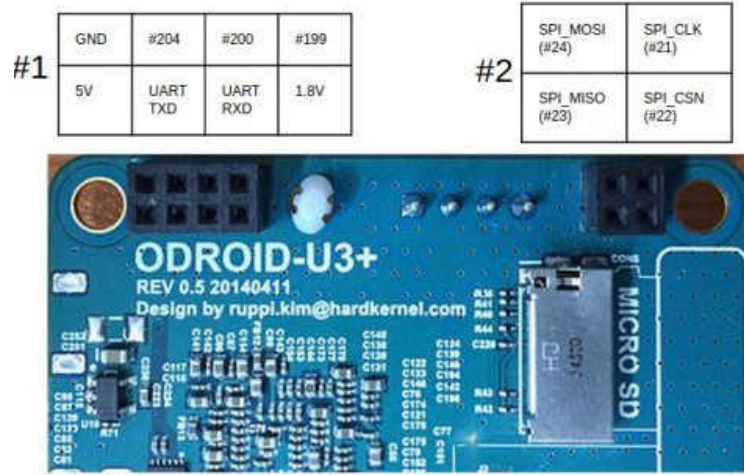


Figure 46. Diagram of GPIO Pins of the Odroid U3 single board computer [37]

The maximum rated input voltage for the GPIO pins of the Odroid U3 is 1.8 V. In triggered mode The Tetracam delivers 3.3V, which is higher than the maximum rated voltage and can destroy the Odroid U3 chip. So, a voltage divider was used to reduce the output voltage from the Tetracam Multi I/O pin 9. Two 10K ohm resistor is used to build the voltage divider to lower down the input voltage from 3.3V into half i.e. 1.65V. This will help to maintain safe operation of the single board computer without damaging the Odroid U3 chip. Figure 47 shows the schematics of the voltage divider that was used to reduce the voltage of the Multi I/O pin 9.

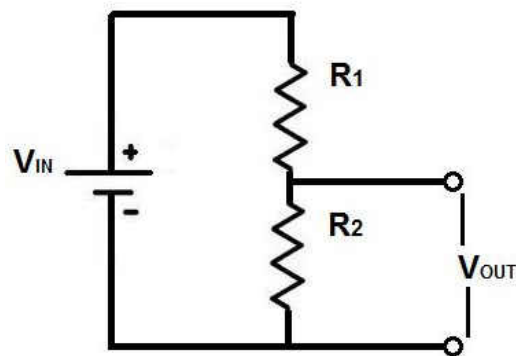


Figure 47. Circuit diagram of the voltage divider [65].

$$V_{out} = V_{in} \left( \frac{R_2}{R_1 + R_2} \right) \quad (19)$$

Figure 48 shows the connection of the Tetracam ADC lite Multi I/O pin and the GPIO pins through a small breadboard for the test integration. The next step was to define the logic to configure the GPIO pins to follow the signal of the Tetracam ADC lite Multi I/O pin. The Linux shell script was written inside single board computer to interpret the logic of GPIO pin 204 to control the FFMPEG software command for capturing the FLIR Photon 320 still images.

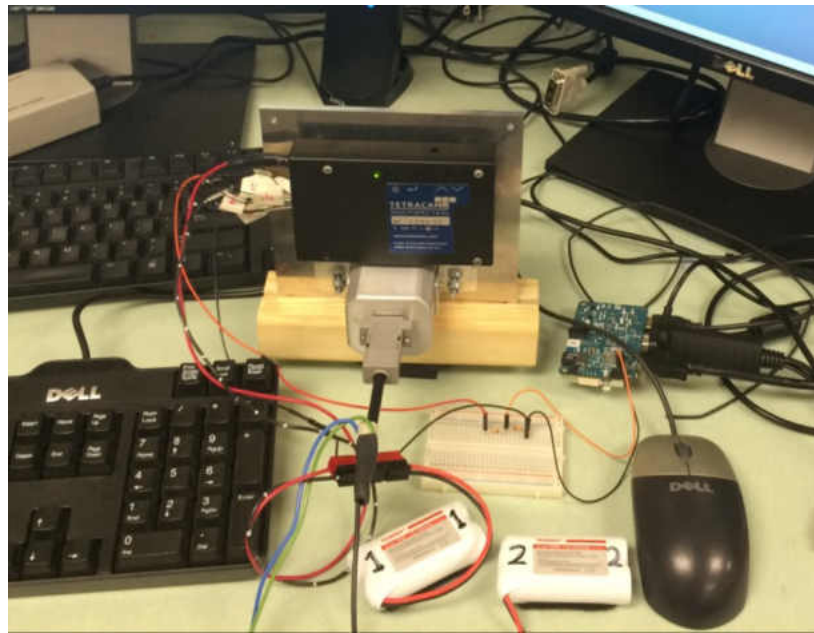


Figure 48. Integration of the camera system using GPIO pins of single board computer and Multi I/O pins of Tetracam ADC lite.

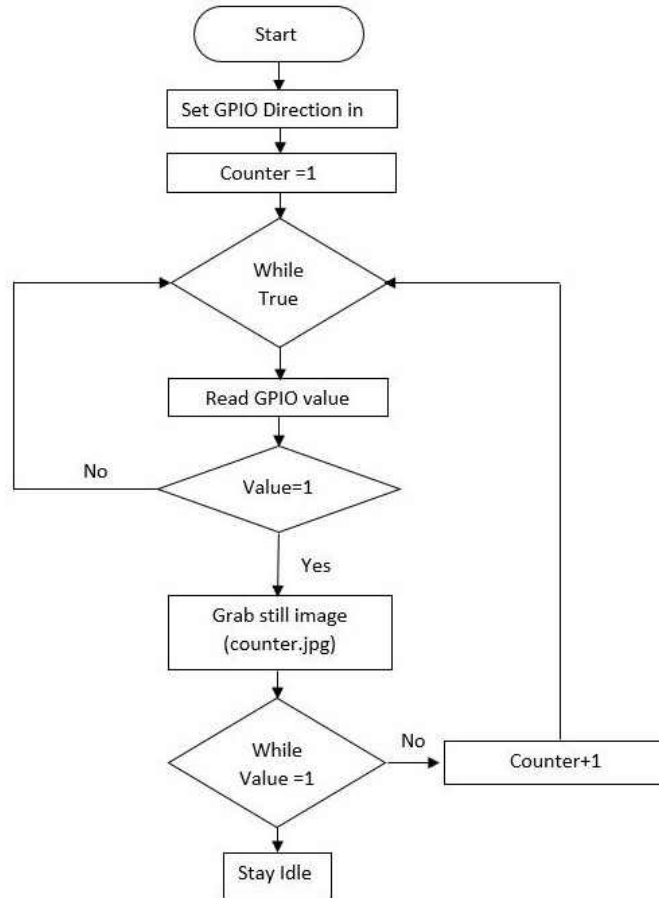


Figure 49. Flow chart of operation of integrated camera systems

Figure 49 displays the logical flow of the data capture process for the integrated camera system. At first, the GPIO direction of the Odroid U3 is set to (In) mode. The counter is specified with an initial value of 1 which is later used for the naming convention of captured images. After the initial set up the program executes in an infinite loop. It keeps on reading the GPIO values constantly in a loop. Whenever Tetracam ADC lite is triggered to capture the image, the Multi I/O pin 9 gets logic high with 3.3 V. The Tetracam ADC lite Multi I/O Pin 9 passes the high logic to the GPIO pin 204 of single board computer. The script reads value 1 and instantly grabs still image from the FLIR Photon 320 infrared camera. After capturing a single still image it stays idle until the Tetracam data capture process is finished. After finishing Tetracam image capture process, the value goes to 0.



Then the counter is incremented by 1 and waits for another cycle. This data capture cycle repeats every time whenever the Tetracam ADC lite is triggered. The script will continue in an infinite loop and stays idle after the Tetracam ADC lite stops triggering.

### Camera Capture Test

The camera capture test was performed to verify if the two cameras are taking the images at the same time. The test was performed using the pendulum as a moving target. The pendulum was designed with the heating wire and metal weight tied up at the end of the heating wire. The heating wire was connected to the AC voltage supply for heating. Initially, the static image was taken to compare the alignment of the images when the pendulum was not moving. The autonomous image capture mode was set up with a 5-second time delay between consecutive images. The pendulum was pulled to swing itself and the images were captured with autonomous time delay operation of the integrated camera system. At the static position of the pendulum, the image from the Tetracam multispectral camera and the FLIR Photon 320 infrared camera was aligned. While the pendulum was swinging several images were captured and tested for the alignment. Figure 50 shows the comparison of the images taken from the integrated camera system with the autonomous operation. In Figure 50, image *a*) is the static images and Image *b*), *c*) and *d*) are the images when the pendulum was moving. Image *b*) was captured at 10 seconds and the pendulum was moving to left direction, Image *c*) was captured at 20 seconds, pendulum moving to left direction and image *d*) was captured at 25 seconds with pendulum moving to left direction after the initialization of continuous capture mode. Image *b* has offset of (5,4) which corresponds to 5 pixels in the X direction and 4 pixels in the Y direction. The pixel offset is changed to (2,6) in image *c* and (8,2) in image *d*). The time stamp for the

images captured has the same time in seconds units but this test concludes that there is a small time lag between the Tetracam multispectral and FLIR Photon 320 infrared camera capture time. The FLIR Photon 320 had the delay with respect to the Tetracam. The exact delay time was not quantified in this experiment. More experiments are needed to be performed to quantify the exact time lag between two cameras. At this point, it can be assumed that there is a fraction of seconds delay in the capture time between two cameras.

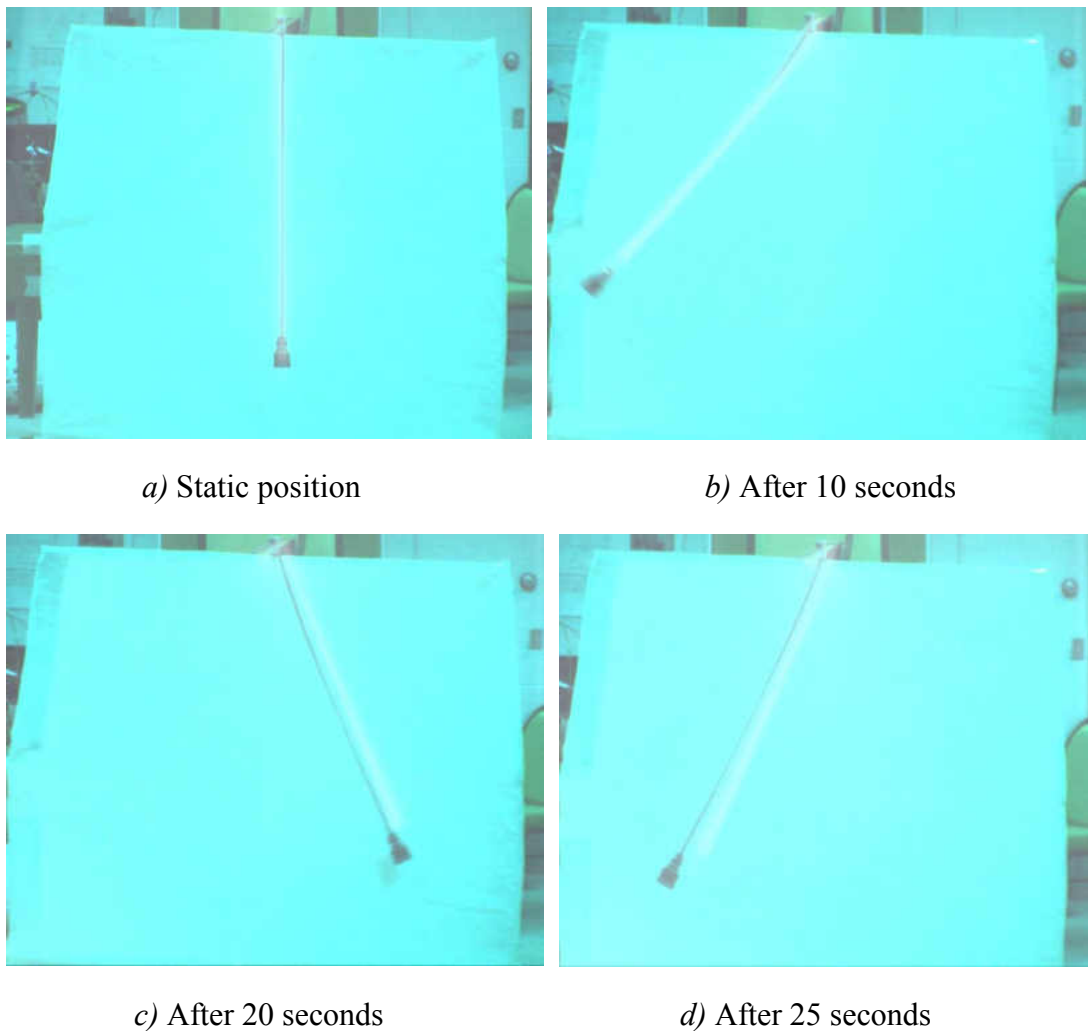


Figure 50. Capture time experiment images. *a)* Image, when the pendulum is static *b)* image after 10 seconds *c)* Image after 20 seconds *d)* image after 25 seconds after the starting of continuous capture mode.

No matter how the cameras are aligned and calibrated for the static scene, the camera without proper synchronization will behave differently for the moving object [66]. In the past studies, there were discrepancies in the continuous capture timing of Tetracam operation [27]. Dvorak implemented LED voltage to mark when the Tetracam images were captured in the autopilot log file. He found that there was 0.960 seconds delay when first trigger command was sent [27]. To synchronize the multiple camera systems, the software based synchronized image capture with error checking has been proposed by many researchers [67, 68]. Using this method the discrepancy in the synchronization is solved by calculating the time for sending the data over the camera network. The test data are sent to the camera network and the network time is calculated for stimulation and response. The calculated delay time is added to the reference time of other cameras thereby synchronizing the clock stamp [67, 68].

Sousa et al. demonstrated the technique to synchronize up to 8 individual self-timed cameras with minimal error using a four wire interface in a master-slave configuration [69]. The slave cameras are interfaced directly with the master camera control module. The synchronization is solved by adaptively regulating the power supply for each camera. The control core was created to monitor the operating frequency of the individual camera by measuring the line period signal of each frame. The frequency of each slave cameras is adjusted by varying the voltage level applied to the sensor, based on the error between measured and desired line period signal [69].

#### Data Collection

Data collection from the payload includes the major steps that must be followed strictly to gather all necessary information in right order. Once the payload system is flown

with the UAV we cannot control the system. And it should work on its own so it totally depends on how we set up the payload before the flight.

### *Tetracam Spectral Calibration Image*

For the precise data collection from the Tetracam ADC lite the spectral intensities must be calibrated for the environment [22]. Calibration process consists of capturing the image of a Teflon calibration tag included in the Tetracam camera supplies under the same lighting condition, location and time of the experiment. This Teflon tag image provides the spectral balance of the sunlight at the time and location of the study. The calibration image should be taken within an hour or two at the time of the study. Any delay will cause the inaccurate calculation of the vegetation indices [22]. The Teflon tag image should be taken so that it covers the entire frame of the camera, but we need to make sure it is illuminated by the sun but not reflecting sunlight directly to the camera. We also need to make sure the image is not over saturated. To fix the overexposed and high saturated calibration image we need to manually decrease the aperture of the Tetracam ADC lite and keep taking pictures until we have less saturated calibration image. Figure 51 shows the calibration images of the Teflon tags, the image on the left is overexposed to the sunlight while the right one is less exposed and less saturated. Later on, the Teflon tag image is used to find out the ratio of NIR to red and NIR to green at the time of data capture using Pixel Wrench 2 Software.

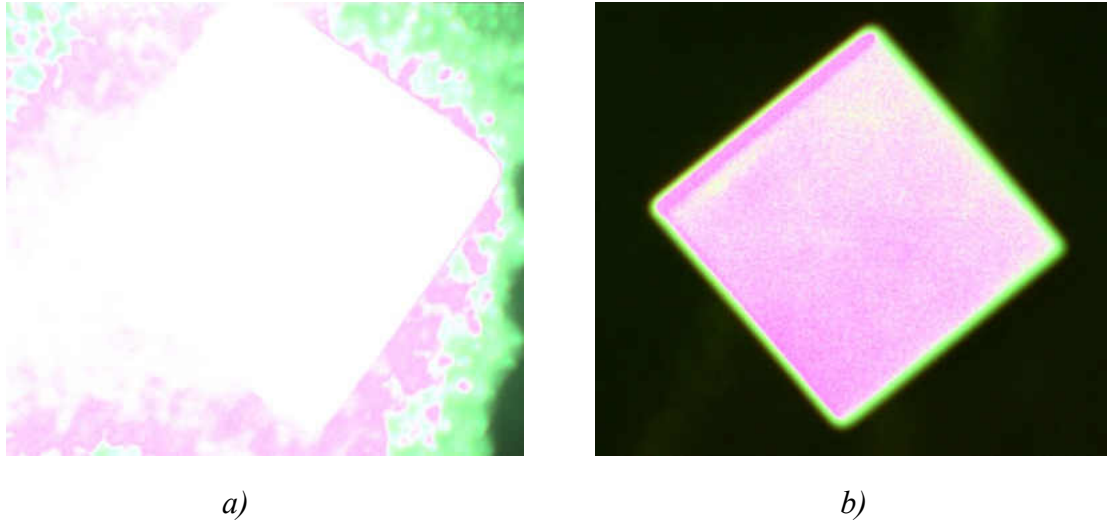


Figure 51. Teflon tag calibration images *a)* highly saturated image *b)* less saturated image

#### *Continuous Capture Configuration*

The Tetracam ADC lite needs to be set in the continuous capture mode through its configuration menu to make it triggering continuously. The continuous capture configuration mode causes the Tetracam ADC lite to start capturing images when the trigger switch is pressed and keeps capturing until the trigger switch is pressed again [22]. So this configuration provides the opportunity for autonomous data capture method in UAVs operation.

The Sabrent USB video adaptor can be used with Tetracam RCA video out port to preview its menu on the computer screen with any webcam display software. Figure 52 shows the preview of the Tetracam ADC lite configuration menu. Tetracam can be set to the various time elapsed triggering from 1 second to 60 seconds [22]. Tetracam offers three different image formats DCM, RAW 10 and RAW8. Typical complete data capture interval for DCM format is 7 seconds, RAW 10 is 4 seconds and RAW8 is 3 seconds. So, we need to set up the time delays according to image formats.

CAPTURE METHOD	
SAVE MODE	DCM 10
FIXED EXP	OFF
AUTO EXP METHOD	AVERAGE
CONT. CAPTURE	OFF
CONT. DELAY	5.0
LOG EVENTS	OFF
DONE	

Figure 52. Preview of Tetracam ADC lite configuration menu [22]

We also need to consider the UAV ground speed for setting the delays for continuous capture. Setting up high delay time for the high-speed aircraft at low altitude can miss out area coverage due to rapid change in the field of view relative to data capture speed as shown in Figure 53. The minimum continuous delay of 3 seconds with RAW 8 image format is compatible for the maximum area overlap of 60% with the aircraft speed 10 m/s and elevation of 500ft for the system designed in this study.

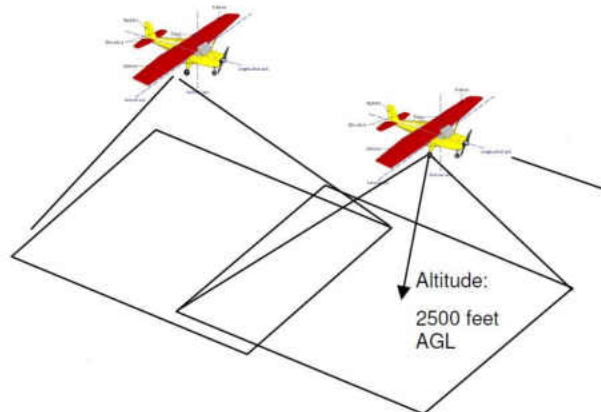


Figure 53. Aircraft ground area coverage with flight speed [22].

### *Payload Operation Setup*

To set up the integrated camera payload we need to start up the whole system before the takeoff of UAV from the ground. The remote laptop is used to configure and start up the operation of the payload at the beginning of the data collection. The remote laptop is used to connect the Odroid U3 through the Ethernet cable to run the data capture script remotely using a terminal window. The Odroid U3 is powered on, after finishing booting process the Ethernet cable is connected to interface both computer systems. The Odroid U3 is remotely accessed through its static IP address. The Odroid U3 now can be controlled through the remote laptop. The data capture script for the FLIR Photon 320 is run from the remote laptop. After running the script in the Odroid U3, the continuous data capture process can be started by pressing the Tetracam trigger button. Once the trigger button is pressed in the Tetracam multispectral camera, the computer saves the current still image from the FLIR Photon 320. The data capture process can also be viewed from the terminal window of the host laptop. After running the script and making sure the data collection is taking place the Ethernet cable can be removed. The payload system keeps on capturing the data autonomously until the Tetracam storage is full or the trigger button is pressed again. At this time, we can take off the UAV for autonomous aerial data collection.

### *Data Retrieval*

After finishing the flight, the captured images from the FLIR Photon 320 infrared camera, stored in the SD card of the Odroid U3 is retrieved by copying to the flash drive through Odroid U3 USB port. Multiple executions of the script will overwrite the image files and replaces the old ones with the new images so, failing to copy the data from the Odroid U3 right away can cause loss of the data.

CHAPTER VI  
POST PROCESSING  
Raw Image Processing

Once the captured data is recovered from the both cameras the raw images are transferred to the computer for initial processing. Raw images from the Tetracam need to be color processed to viewable useful format. The raw images of the Tetracam ADC lite are color processed using the Tetracam Inc. Pixel Wrench 2 software, which is included with the purchase of the camera. The preprocessing of the images can be done individually for a single image or all images in a batch. The processed images can be saved to different formats such as TIFF, JPEG, BMP etc.

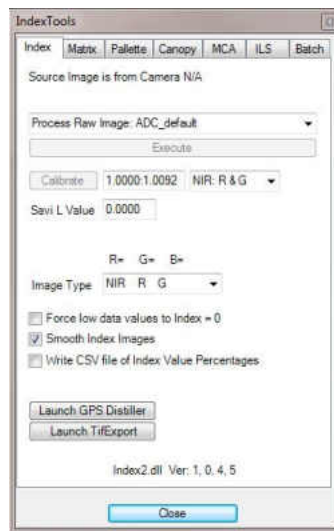


Figure 54. Snapshot of the Index Tools menu of the Pixel Wrench 2 software showing calibrate button and raw image processing options [22].

The Teflon tag image taken at the time of data collection is loaded on the Pixel Wrench 2 software and in the Index Tools, the calibrate button is pressed. Now this Teflon



tag image gives the ratio of near infrared to red and green bands to calibrate spectral intensities in any vegetation index extraction such as NDVI, SAVI, and Green NDVI etc. [22]. The color processed Tetracam images are rectified using the camera parameters obtained in Chapter IV from camera calibration process. This will correct any distortion induced due to the poor lens quality and misalignment of the lens with the sensor. The FLIR Photon 320 infrared camera was set up in the grayscale representing white as high infrared intensity and black as low infrared intensity.

### Spectral Image Analysis

Tetracam ADC Lite image is separated into three single band images from a single composite original image. Each band of the image consists of its own spectral information. Now in total, we have four image bands near infrared, red and green band from the Tetracam multispectral camera and the infrared band from the FLIR Photon 320 infrared camera. Figure 55 shows the infrared image from the FLIR Photon 320 infrared camera and three separated near infrared, red and green bands images from Tetracam ADC lite. We captured the image data set with 4 different temperature and three different orientation of the warm-blooded target in the scene. The images captured at a temperature of 74 °F and warm-blooded target hiding behind the vegetation is used in this chapter to show the image processing method applied to extract the useful information and experiment the enhanced visualization.

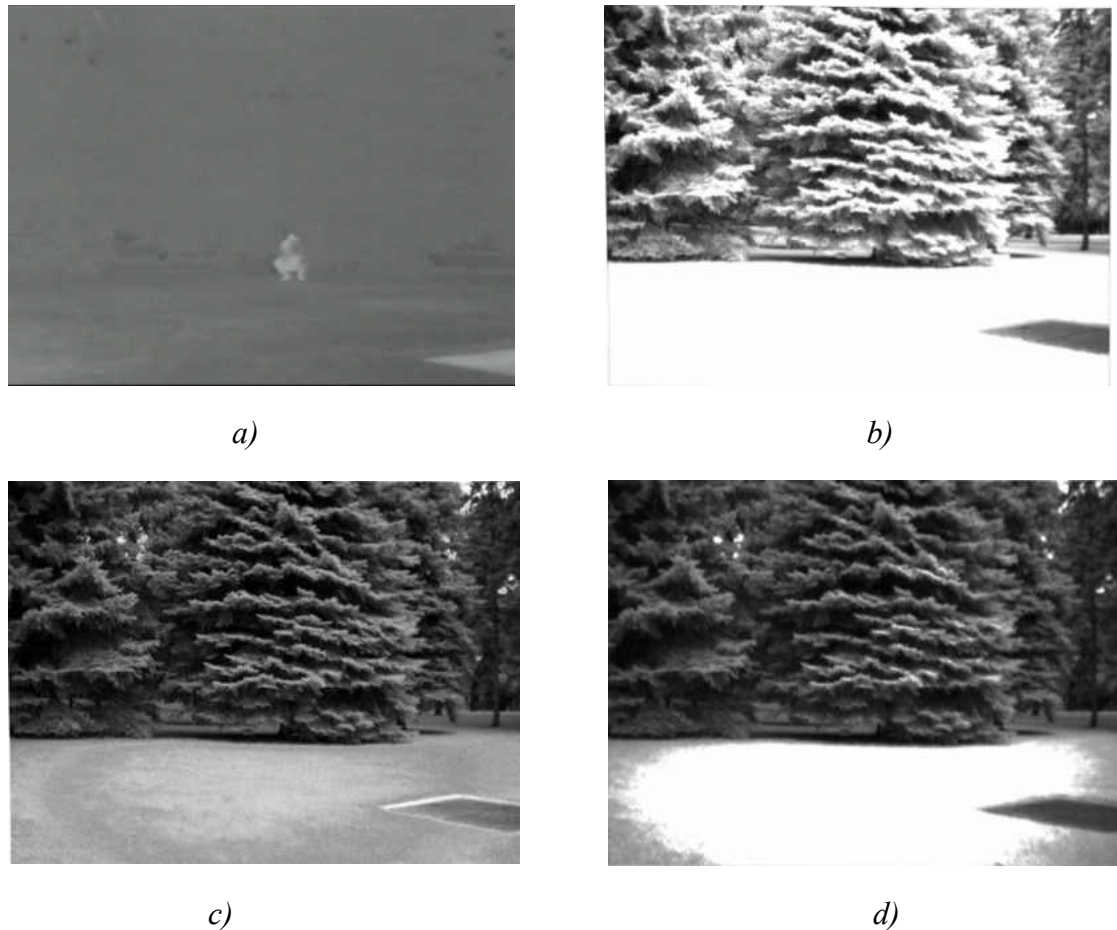


Figure 55. Separation of Multispectral image from Tetracam ADC lite a) Infrared band image b) Near Infrared band image c) Red band image and d) Green band image.

### *Normalized Difference Vegetation Index (NDVI)*

Normalized Difference Vegetation Index (NDVI) is the well-known vegetation index used to detect the healthy and unhealthy vegetation. The healthy plant highly absorbs the red light for the photosynthesis process and highly reflects the near infrared. Whereas the stressed plant highly reflects the red band and reflects significantly low near infrared than the healthy vegetation [7, 29]. Figure 56 shows the spectral reflectance signature of the healthy and unhealthy vegetation.

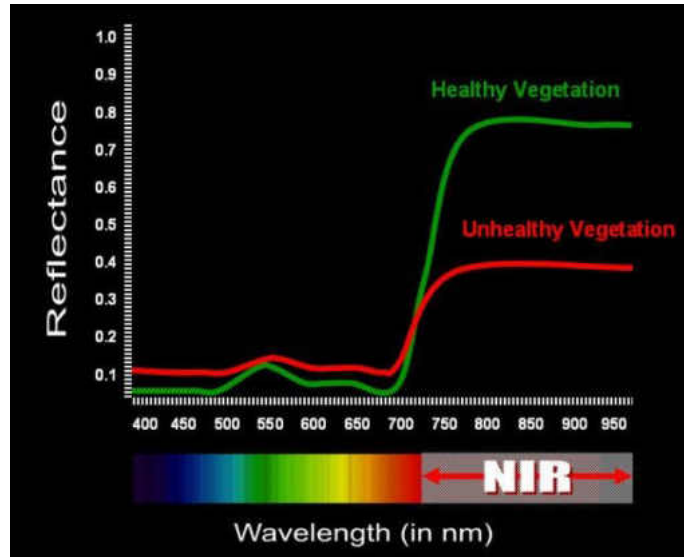


Figure 56. Spectral reflectance signature of the healthy and unhealthy vegetation in visible through near infrared spectrum [32].

As we can see in the reflection vs wavelength (spectral signature) plot in Figure 56. The healthy vegetation has a very low reflectance in the visible region as compared to the unhealthy vegetation. Conversely, the healthy vegetation has a very high reflectance in near infrared region of electromagnetic spectrum. Such anomaly in the different spectral band helps to detect the healthy and unhealthy vegetation. From this spectral signature of healthy and unhealthy plants, we can classify them by calculating Normalized Difference Vegetation Index (NDVI) using near infrared and red bands as given by Equation 20 [31, 70].

$$NDVI = \frac{NIR-RED}{NIR+RED} \quad (20)$$

The NDVI value varies from -1 to +1 representing +1 as the presence of healthy vegetation and -1 representing no vegetation [31, 70-71]. Figure 57 shows the NDVI image of Figure 55 with the color bar representing its indices. As we can see that there were very few spots which represent the index value of 1 which is very healthy vegetation represented in red color. The ground portion of the image is composed of the stressed grass which

represents the value of 0. The image has most of light blue, yellow and orange spots ranging the index value from 0.4 to 0.8. The blue spots at some part of the leaves of the tree shown in the image are irrelevant since they are supposed to behave as high vegetation part.

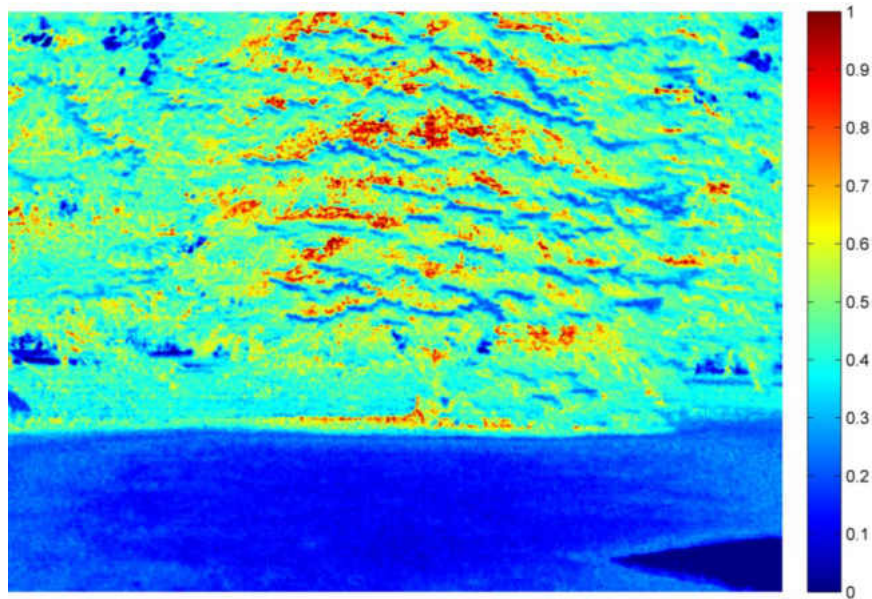


Figure 57. Color mapped NDVI using separated band images in Figure 55

The image used to calculate the NDVI in Figure 57 was captured from ground, sensor facing the vegetation from the side of the canopy. There are many factors such as view angle, atmospheric effects, soil background noise, solar angle and canopy architecture which affects the estimation of the NDVI [71-75]. The estimation of the NDVI changes with changing these factors while capturing the images. Over the top of vegetation canopies near infrared band is scattered mostly than the red band. This effect increases the spectral contrast between red and near infrared band, which leads to higher values of NDVI for shaded canopy than in direct sunlight [71]. View and solar angle are the most dominant factors which affect the estimation of vegetation indices [71]. With changing the zenith sun angle the illumination varies over the canopy. NDVI increases as view zenith angle

increases [71-75]. The low sun angles will result in low NDVI, it has low values at Nadir view [74].

In areas with low vegetation, the variation in the reflectance of the red light from the difference in the soil reflectance due to the presence of moisture and different soil types changes the NDVI independent of vegetation cover [74]. Sun angle is more prominent in the less dense vegetation whereas view angle is most dominant in the highly vegetated sites [71]. The solar irradiance varies with atmospheric condition, which changes the reflectance of the spectral bands so the spectral response obtained by the sensor will vary depending upon the atmospheric condition [72, 74].

Besides detecting healthy vegetation with the spectral bands produced from the Tetracam ADC lite multispectral camera, the one of the research objective is to study the visual enhancement of warm-blooded animals living at same locations. We studied the different combination of the images taken at variable temperature with different scenes including vegetation and warm-blooded animal as a target. The final goal of the spectral image combination experiment is to observe the visual enhancement of the warm-blooded targets. In total, we have images of 4 spectral bands infrared, near infrared, red and green. We tested these four bands to observe the visual enhancement using two methods. The first method used was a combination of spectral bands to develop the composite image with false color representation and the second method was taking the normalized difference ratios. MATLAB software was used as the main tool for image processing.

### *Spectral False Color Combinations*

The three image bands from the Tetracam ADC lite multispectral camera were separated and stored as single grayscale images along with the warped infrared image from the FLIR Photon 320 infrared camera. The infrared image was combined with all three bands from the Tetracam ADC lite to experiment enhance visualization of vegetation and warm-blooded target. Among the four image bands shown in Figure 55 near infrared, red and green image were not able to show the person hiding behind the tree branches but the infrared images show the person hiding behind the tree, whereas the less information about the vegetation is present in the infrared image alone. The false-color combination is a simple tool to create a composite image from three different image bands and displays each band in false color respective to red, green and blue channel depending on the placement order.



Figure 58. False color combination image (R, G, B) = (IR, NIR, Green) at 74 °F



Figure 59. False color combination image (R, G, B) = (IR, NIR, Red) at 74 °F



Figure 60. False color combination image (R, G, B) = (IR, Red, Green) at 74 °F

The above three false color composite images in Figure 58 through Figure 60 were able to show the vegetation as well as a person (warm-blooded animal) hiding behind the

tree at 74 °F. The combination of these bands at different temperature and warm-blooded animal at a different location are shown in results and discussion chapter.

*Normalized Difference Ratio of Image bands*

The three different normalized difference band ratios were computed using the infrared band with near infrared, red and green band respectively to observe the visualization of the targeted objects. The resulting images were color mapped with a color bar showing the values of the ratio in the image.

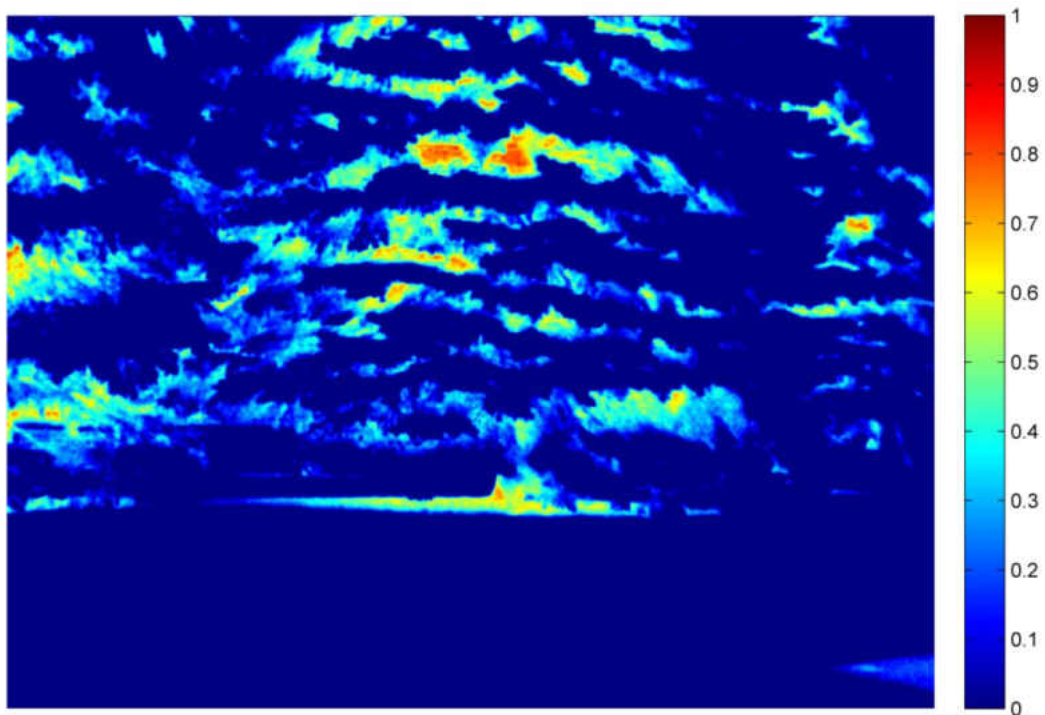


Figure 61. Normalized Difference band ratio of  $(IR-NIR) / (IR+NIR)$  at 74 °F



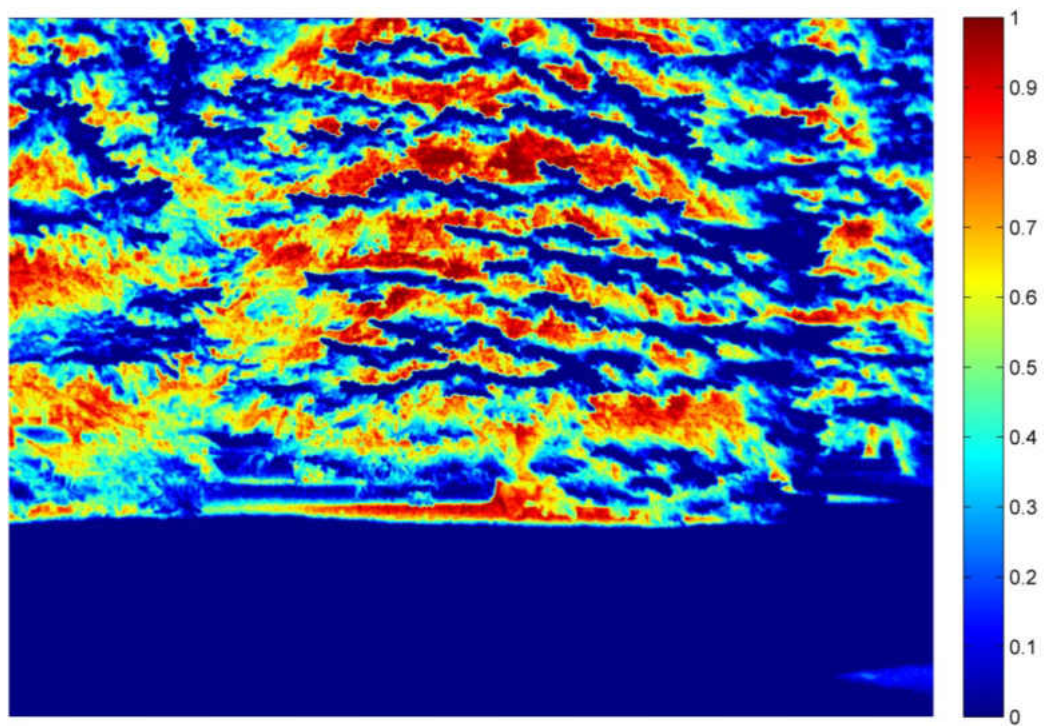


Figure 62. Normalized Difference band ratio of (IR-Red) / (IR+Red) at 74 °F

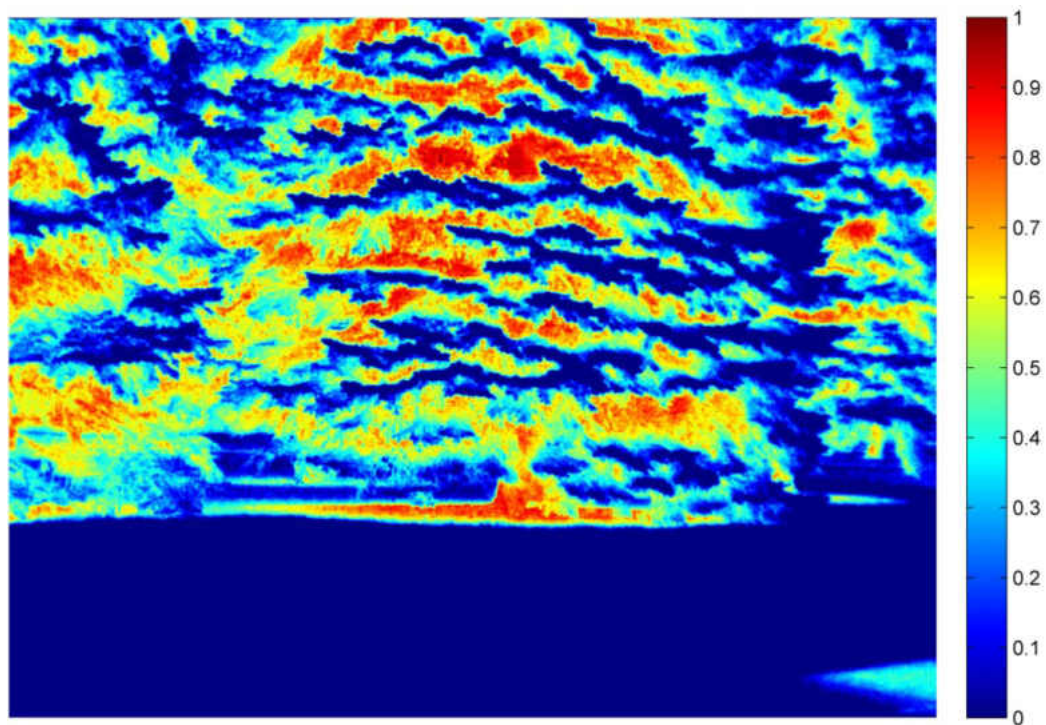


Figure 63. Normalized Difference band ratio of (IR-Green) / (IR+Green) at 74 °F

From Figure 61, 62 and 63 we can see that the normalized band ratio images were not able to enhance the visualization of the warm-blooded animal hiding behind the tree. The figures shown above are for the single temperature image. We studied four different temperature condition with three different target location. The post processing was done for all images and observations were made to draw a final conclusion.

#### *Registration of Infrared Image on NDVI*

The infrared image was segmented to separate the warm-blooded object from the background using the Otsu's threshold method implemented in MATLAB [76, 77]. To display the vegetation health and detected a warm-blooded target in the same scene, the segmented infrared image was overlapped on top of NDVI image with false color representation.

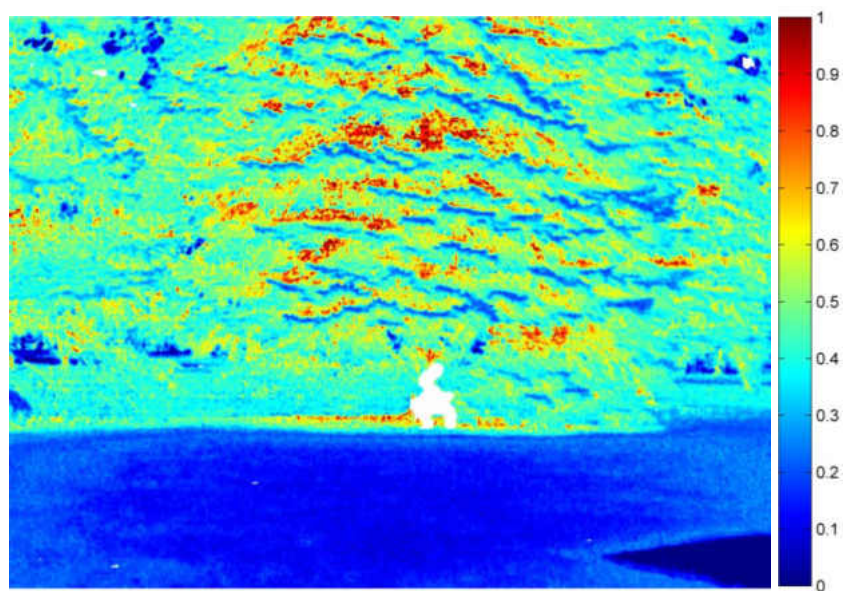


Figure 64. Adding segmented infrared on top of NDVI

As we can see in Figure 64 the warm-blooded target in the segmented infrared image is displayed in white color with the color mapped NDVI image. It also displays the

color bar corresponding to the NDVI index values in the image. The color corresponding to higher index represents the healthy vegetation.

## CHAPTER VII

### RESULTS & DISCUSSION

The Tetracam ADC lite multispectral camera and the FLIR Photon 320 infrared camera system was successfully integrated and tested in a lab environment to produce spatially aligned images. The mechanical alignment, digital image processing and timed data capture system enhanced the spatial registration of the images from two different camera sensor.

The test image data sets were collected with the combinations of three different orientations of the warm-blooded animal with respect to the vegetation at four different temperatures to observe the visibility of warm-blooded target. The first set of images was collected for the warm-blooded target present in front of the vegetation, the second set consists of warm-blooded target partially hiding behind the vegetation and third image set was collected for the warm-blooded target completely hiding behind the vegetation at four different temperatures. The set of test images for the different temperature and location are shown in Figure 65 through Figure 76. The images on the left are from Tetracam ADC lite and the right image is from FLIR Photon 320 in the image pair. The image sets were observed to check visibility of the warm-blooded target.

## 1. Warm-blooded target in front of the vegetation

The first data set consists of the warm-blooded animal located in front of the vegetation at different temperature 50 °F, 74 °F, 85 °F and 95 °F. The raw images are compared to check the visibility of the warm-blooded target through the Tetracam multispectral camera and the FLIR Photon 320 infrared camera without any image processing.



Figure 65. Warm-blooded target in front of the vegetation at 50 °F

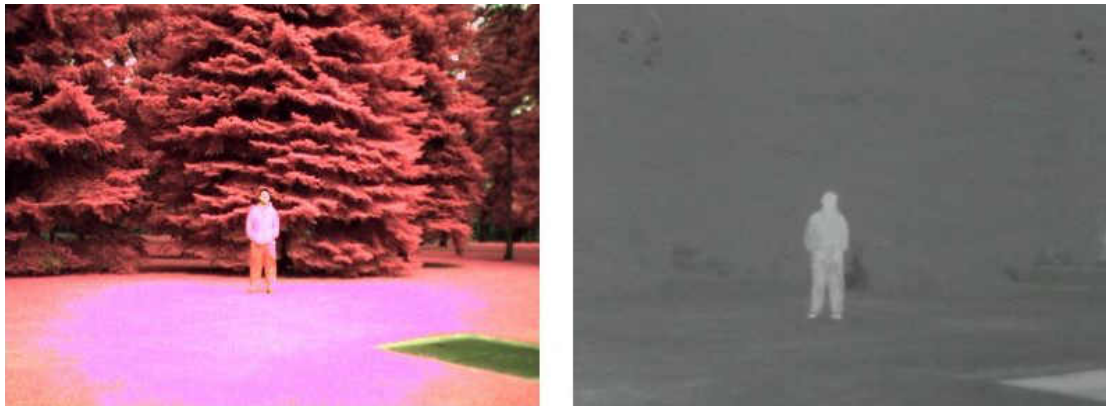


Figure 66. Warm-blooded target in front of the vegetation at 74 °F

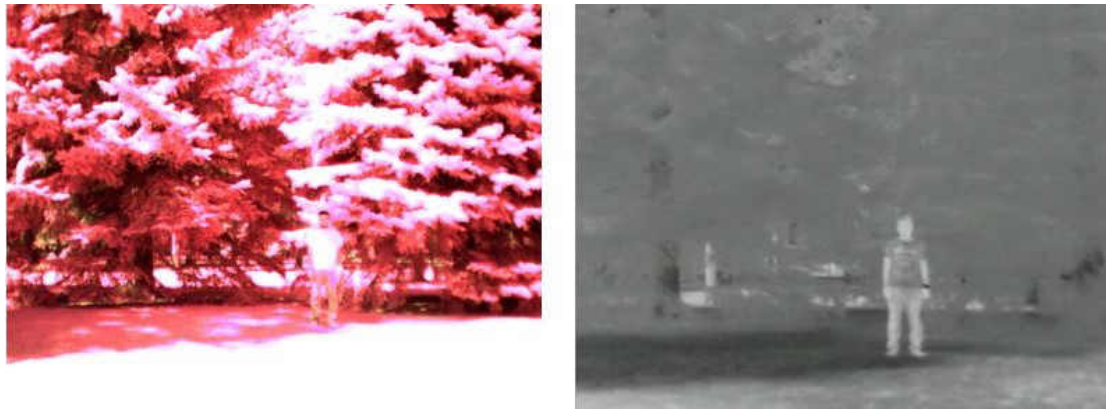


Figure 67. Warm-blooded target in front of the vegetation at 85 °F

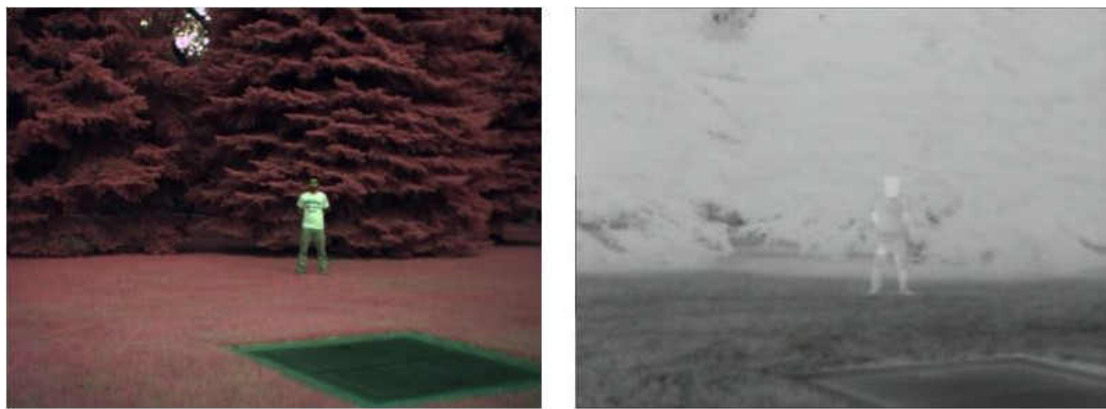


Figure 68. Warm-blooded target in front of the vegetation at 92 °F

When comparing the images for the warm-blooded target located in front of the vegetation shown in Figure 65 through Figure 68, the infrared image showed that the warm-blooded target visibility fades away with an increase in the environment temperature. At 50 °F, 74 °F in Figure 65 and Figure 66 the infrared image shows highly contrast warm-blooded target with respect to the surrounding environment. The infrared image at 92 °F in Figure 68 is partially visible since the temperature of the warm-blooded target (human being) is around 98 °F which caused low-temperature difference with the environment. When observing the Tetracam image the open target is clearly visible at 74 °F and 92 °F. On the other hand at 50 °F in Figure 65 the warm-blooded target looks dim due to lack of

illumination from the sun and at 85 °F the target is highly saturated due to high reflection of sunlight.

## 2. Warm-blooded target partially hiding behind the vegetation

For the second set of the data, the warm-blooded target is placed near the vegetation so that some part of the warm-blooded animal is covered by the vegetation. The image data was captured at the 50 °F, 74 °F, 85 °F and 92 °F. The image sets were compared to check the visibility of warm-blooded target in different temperature.



Figure 69. Warm-blooded target partially behind the vegetation at 50 °F

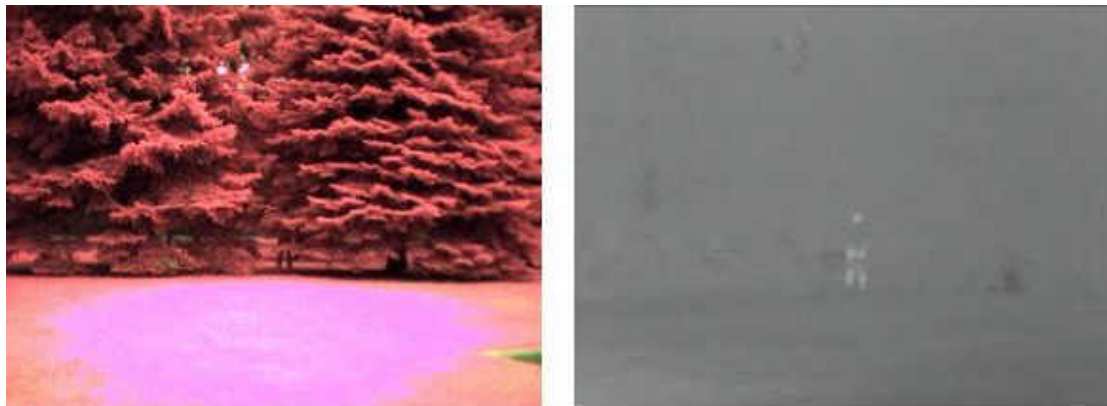


Figure 70. Warm-blooded target partially behind the vegetation at 74 °F

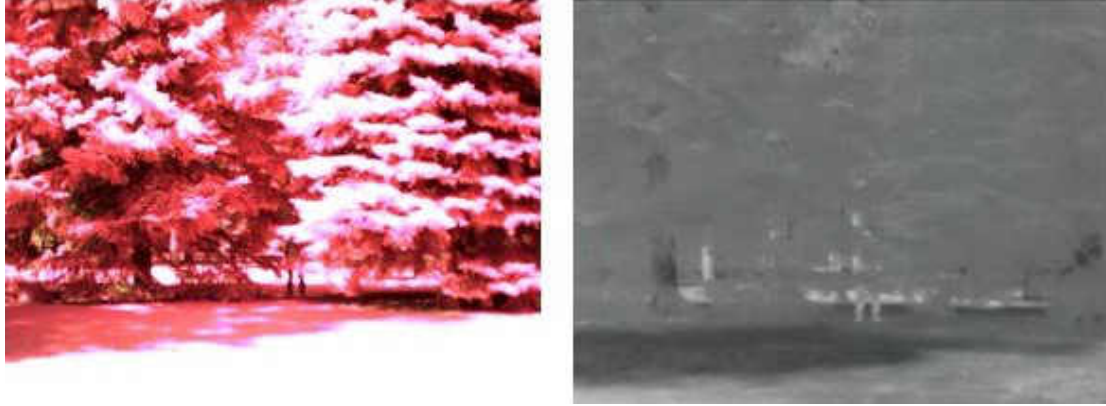


Figure 71. Warm-blooded target partially behind the vegetation at 85 °F



Figure 72. Warm-blooded target partially behind the vegetation at 92 °F

For the warm-blooded target partially hiding behind the vegetation in Figure 69 through 72, at 74 °F and 85 °F in Figure 70 and Figure 71 we cannot see the warm-blooded target clearly through the Tetracam image while the infrared images showed some highly improved sight of the warm-blooded target. The image at 50 °F in Figure 69 is dark and less illuminated by the sunlight but the warm-blooded target is visible in the infrared image with high contrast.

### 3. Warm-blooded target hiding behind the vegetation

The third image data set was collected by placing the warm-blooded target behind the vegetation at the same temperature 50 °F, 74 °F, 85 °F and 92°F. This data set was



collected to observe the visibility performance of infrared image when warm-blooded target hides inside the vegetation.



Figure 73. Warm-blooded target hiding behind the vegetation at 50 °F

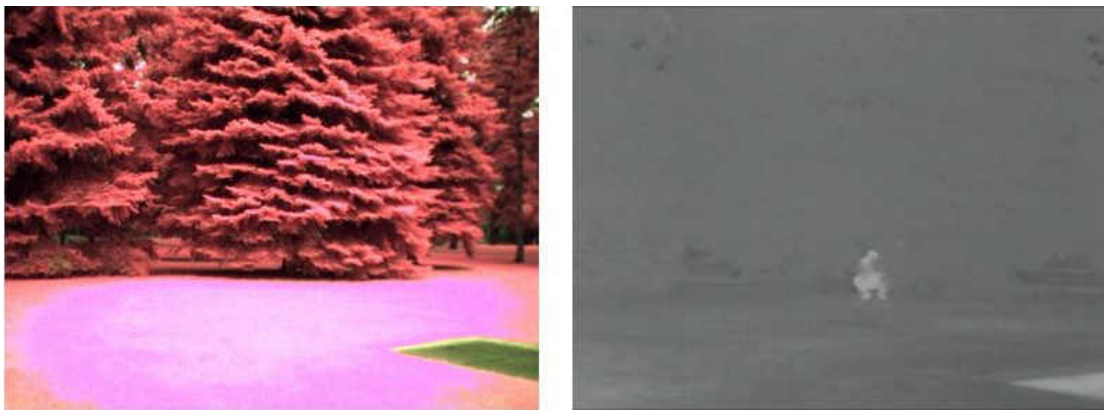


Figure 74. Warm-blooded target hiding behind the vegetation at 74 °F

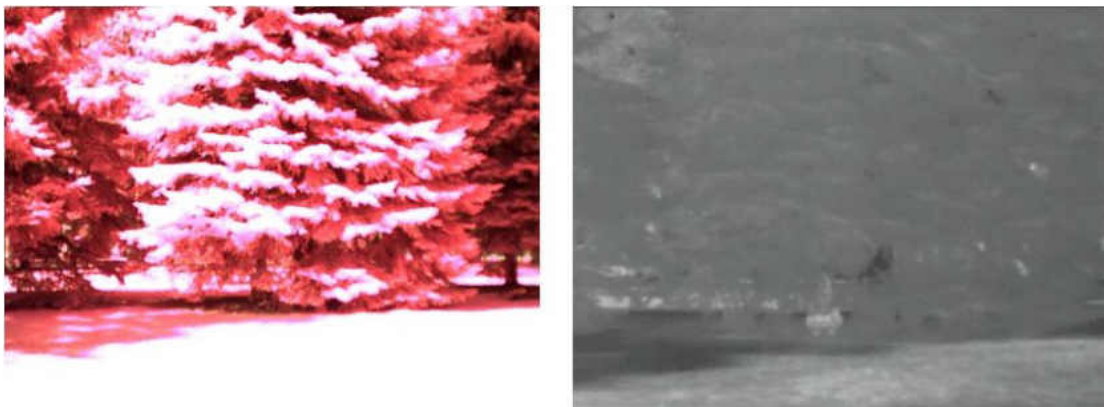


Figure 75. Warm-blooded target hiding behind the vegetation at 85 °F

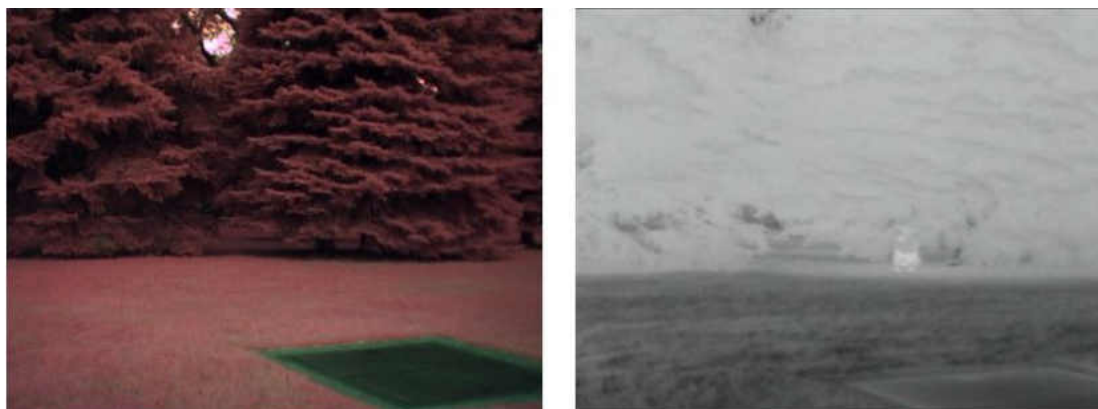


Figure 76. Warm-blooded target hiding behind the vegetation at 92 °F

When observing the warm-blooded target hiding behind the vegetation in Figure 73 through Figure 76 the Tetracam images was not able to show any trace of the warm-blooded target. Whereas the FLIR Photon 320 infrared images were able to detect the warm-blooded target at 50°F in Figure 73 and at 74°F in Figure 74 with high contrast and the fades away with increasing the temperature as observed at 85 °F in Figure 75 and at 92 °F in Figure 76. This raw image comparison concludes that infrared image is the best candidate to display the warm-blooded target information in all the test conditions.

From the direct comparison of the unprocessed image, we found that infrared image has a high tendency to enhance the visibility of the warm-blooded animals in all tested cases. So the infrared band was combined with the near infrared, red and green band to observe the visibility enhancement of warm-blooded animal with added information of the vegetation environment. The false-color combination represents the infrared band as red, near infrared, red and green represents the two of the remaining green and blue false color consecutively. The spectral false color image was generated for the two cases one is a warm-blooded target in front of the vegetation shown in Figure 77 and another one is warm-blooded target hiding behind the vegetation shown in Figure 78.

At 50 °F



( R, G, B) = (IR,NIR,Green)



( R, G, B) = (IR,NIR,Red)



( R, G, B) = (IR, Red, Green)

At 74 °F



( R, G, B) = (IR,NIR,Green)

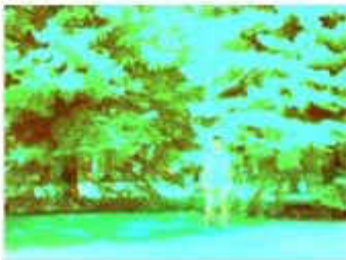


( R, G, B) = (IR,NIR,Red)

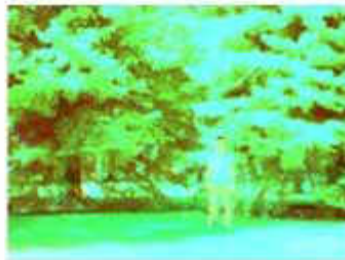


( R, G, B) = (IR, Red, Green)

At 85 °F



( R, G, B) = (IR,NIR,Green)



( R, G, B) = (IR,NIR,Red)



( R, G, B) = (IR, Red, Green)

At 92 °F



( R, G, B) = (IR,NIR,Green)



( R, G, B) = (IR,NIR,Red)



( R, G, B) = (IR, Red, Green)

Figure 77. False color combination for the warm-blooded target in front of the vegetation.

At 50 °F



( R, G, B) = (IR,NIR,Green)

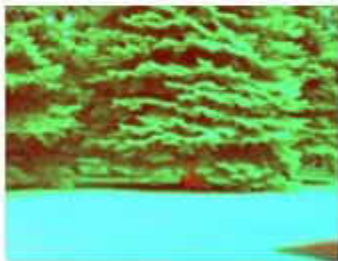


( R, G, B) = (IR,NIR,Red)



( R, G, B) = (IR, Red, Green)

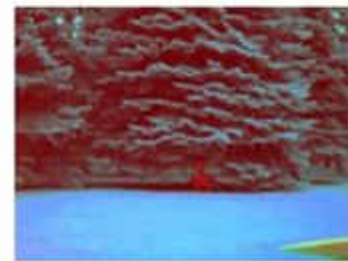
At 74 °F



( R, G, B) = (IR,NIR,Green)

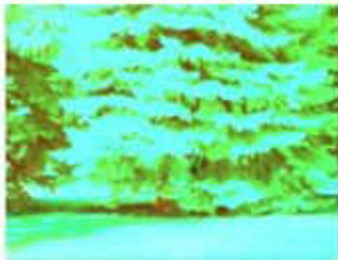


( R, G, B) = (IR,NIR,Red)

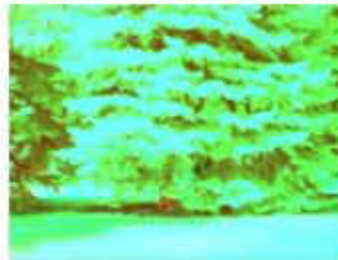


( R, G, B) = (IR, Red, Green)

At 85 °F



( R, G, B) = (IR,NIR,Green)



( R, G, B) = (IR,NIR,Red)



( R, G, B) = (IR, Red, Green)

At 92 °F



( R, G, B) = (IR,NIR,Green)



( R, G, B) = (IR,NIR,Red)



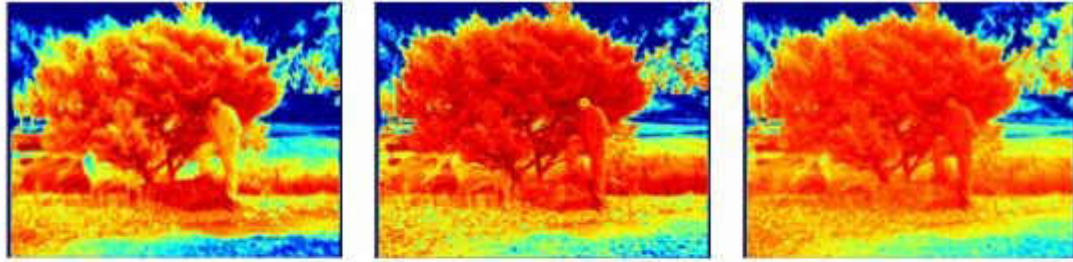
( R, G, B) = (IR, Red, Green)

Figure 78. False color combination for the warm-blooded target hiding behind the vegetation.

From the spectral false color images, we can see that the false-color combination of (IR, Red, Green) displays the warm-blooded target with high contrast among all other combinations. In the (IR, Red, Green) false color image, the infrared band was able to display warm-blooded target with red and green displaying the environment information more clearly. This combination was able to show the warm-blooded target even at the highly saturated image at 85 °F. The other two false-color combinations (IR, NIR, Green) and (IR, NIR, Red) showed an almost similar pattern like (IR, Red, Green) at 50 °F and 92 °F. But the visibility of warm-blooded target in these false-color images was reduced at saturated images at 85 °F and 74 °F when compared to the combination of (IR, Red, Green).

Normalized difference band ratio was also experimented as another visibility enhancement test based upon the essence of the spectral signature of the materials. The normalized difference band ratios were calculated using infrared, near infrared, red and green band to observe any significant visibility enhancement of the target with response to the surrounding vegetation. If vegetation and warm-blooded target have a significant difference in absorption and reflection of energy in certain spectral bands, we might be able to see a significant change in the normalized difference band ratio images [7]. The normalized difference band ratios images are color mapped with red being the highest ratio and blue being lowest. The normalized difference band ratios were shown for the data sets of the target in front of the vegetation and target hiding behind the vegetation in Figure 79 and Figure 80. In this way, we might observe any existing significant pattern of the warm-blooded target with respect to spectral bands when the target is extremely visible and invisible.

At 50 °F

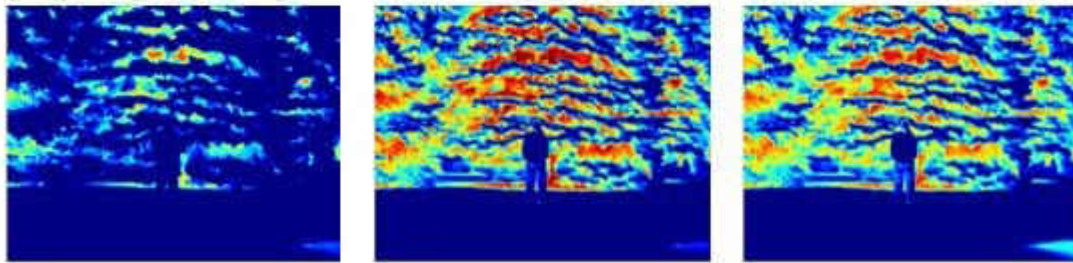


(IR-NIR)/(IR+NIR)

(IR-Red)/(IR+Red)

(IR-Green)/(IR+Green)

At 74 °F

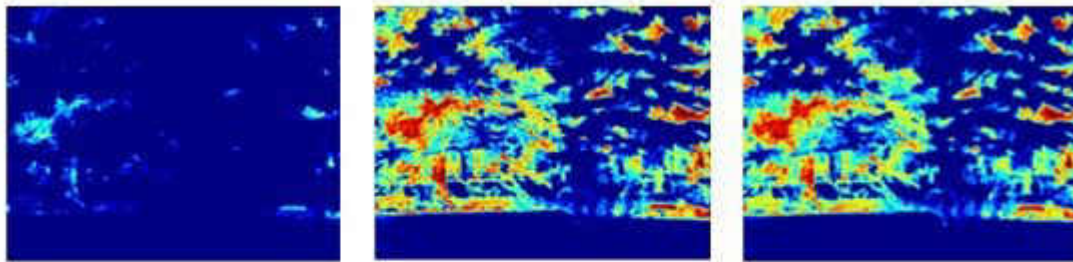


(IR-NIR)/(IR+NIR)

(IR-Red)/(IR+Red)

(IR-Green)/(IR+Green)

At 85 °F

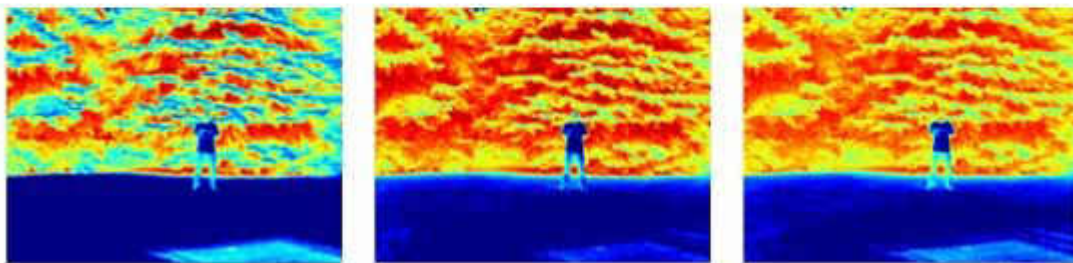


(IR-NIR)/(IR+NIR)

(IR-Red)/(IR+Red)

(IR-Green)/(IR+Green)

At 92 °F



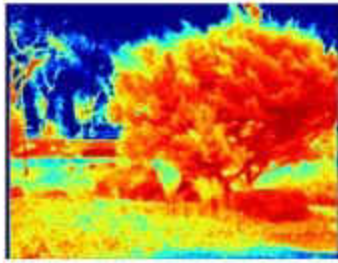
(IR-NIR)/(IR+NIR)

(IR-Red)/(IR+Red)

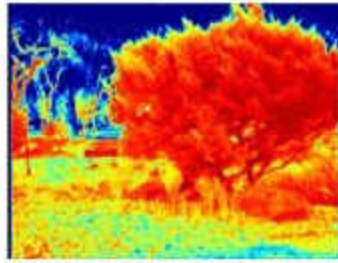
(IR-Green)/(IR+Green)

Figure 79. Normalized band ratios for the warm-blooded target in front of the vegetation

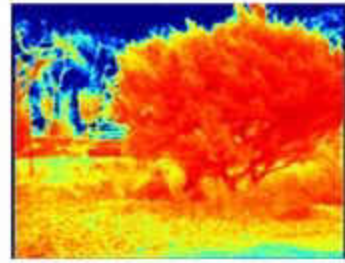
At 50 °F



$(IR-NIR)/(IR+NIR)$

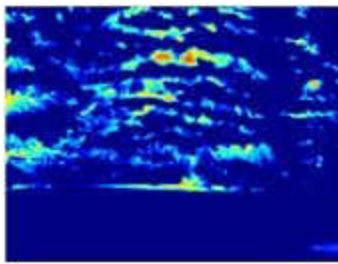


$(IR-Red)/(IR+Red)$

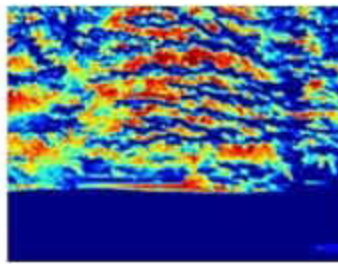


$(IR-Green)/(IR+Green)$

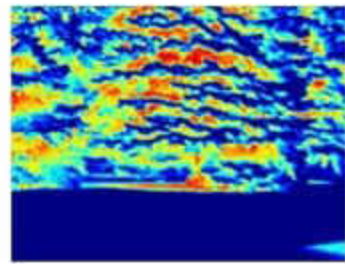
At 74 °F



$(IR-NIR)/(IR+NIR)$

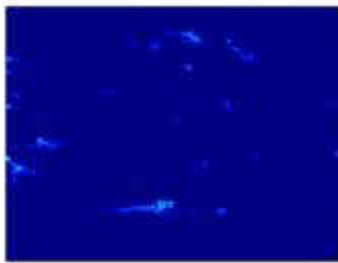


$(IR-Red)/(IR+Red)$

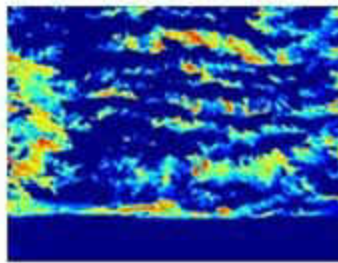


$(IR-Green)/(IR+Green)$

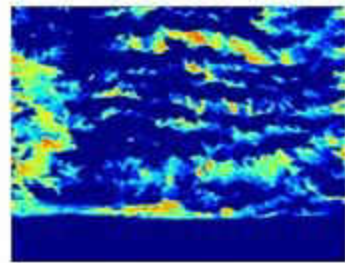
At 85 °F



$(IR-NIR)/(IR+NIR)$

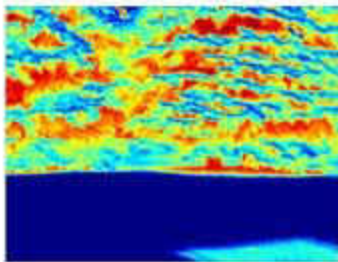


$(IR-Red)/(IR+Red)$

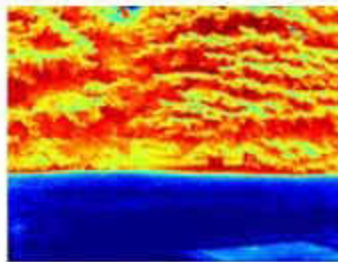


$(IR-Green)/(IR+Green)$

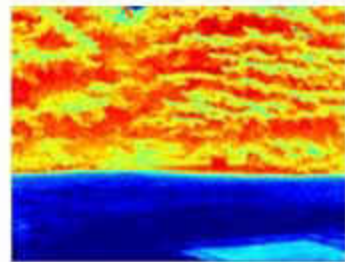
At 92 °F



$(IR-NIR)/(IR+NIR)$



$(IR-Red)/(IR+Red)$



$(IR-Green)/(IR+Green)$

Figure 80. Normalized band ratio for the warm-blooded target hiding behind the vegetation.

From Figure 79 we can observe that the normalized difference band ratio of  $(IR-NIR)/(IR+NIR)$  showed some interesting behavior on the images at 74 °F and 85 °F. The ratio is almost 0 all over the image pixels. These images were taken at the sunny time of the day. Which reveals that reflection of the near infrared and infrared radiation from both warm-blooded target and vegetation is almost equal at that time. On the other hand, the image at 50 °F was captured at dark gloomy day and 92 °F were taken during the less gloomy day. The  $(IR-NIR)/(IR+NIR)$  normalized difference band ratio showed some distribution range in color mapped image with a visible warm-blooded target at 92 °F. At 50 °F, the ratio seems almost 1 for the warm-blooded target and vegetation since the infrared band dominance was the higher due to the presence of low reflection of near infrared band. But it was able to show the warm-blooded target due to its high infrared radiation compared to vegetation.

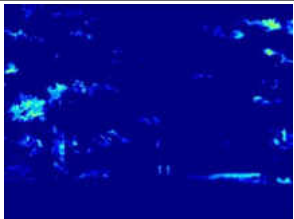
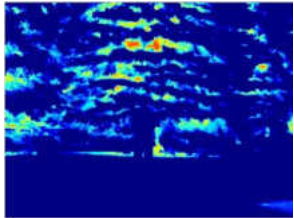

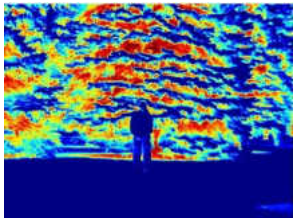

The other two normalized difference band ratios  $(IR-Red)/(IR+Red)$  and  $(IR-Green)/(IR+Green)$  showed similar pattern at all temperatures. These band ratios were able to show the warm-blooded target at 50 °F, 74°F and 92 °F. But they were unable to identify the target at 85 °F. It shows that these band ratios is not feasible for high saturated images.

For the warm-blooded target hiding behind the vegetation shown in Figure 80, the color mapped normalized band ratio images were not able to show the target clearly compared to the individual infrared image. Since the experimented image results are qualitative and quality depends on how the target is visible in the image as perceived with the aid of eye. So in order to quantify how processed image enhanced the visibility, the image data is categorized to rank the visibility of warm-blooded animal in the scene based on a scale of 1 to 5. Where 1 means invisible and 5 indicates perfectly visible of a warm-



blooded animal in the scene. The ranking rubric is totally based upon the contrast at the edges of the warm-blooded target with respect to the surrounding. Table 9 explains the ranking description and shows reference picture used to rank the processed image. Figure 81, Figure 82 and Figure 83 shows the bar graph representation of the ranking of the images based upon the Table 9 image descriptions.

Table 9. Ranking rubric for visibility of warm-blooded target.

Rank	Image	Description
1		<ul style="list-style-type: none"> <li>• Very Dim image with no contrast and visibility</li> <li>• No sign of presence of warm-blooded targets</li> </ul>
2		<ul style="list-style-type: none"> <li>• Dim image with little contrast at the edges of warm-blooded animal</li> <li>• Presence of hue on the background and small change in intensity at outline of the warm-blooded target</li> </ul>
3		<ul style="list-style-type: none"> <li>• Visibility of warm-blooded target</li> <li>• Little contrast around the outline of the warm-blooded target</li> <li>• Little difference in intensity between warm blooded target and background</li> </ul>
4		<ul style="list-style-type: none"> <li>• Clear view of the warm-blooded target</li> <li>• High contrast outline of the warm-blooded target</li> </ul>
5		<ul style="list-style-type: none"> <li>• Complete visibility of the warm-blooded target</li> <li>• Highly contrast of warm-blooded target relative to the background.</li> </ul>

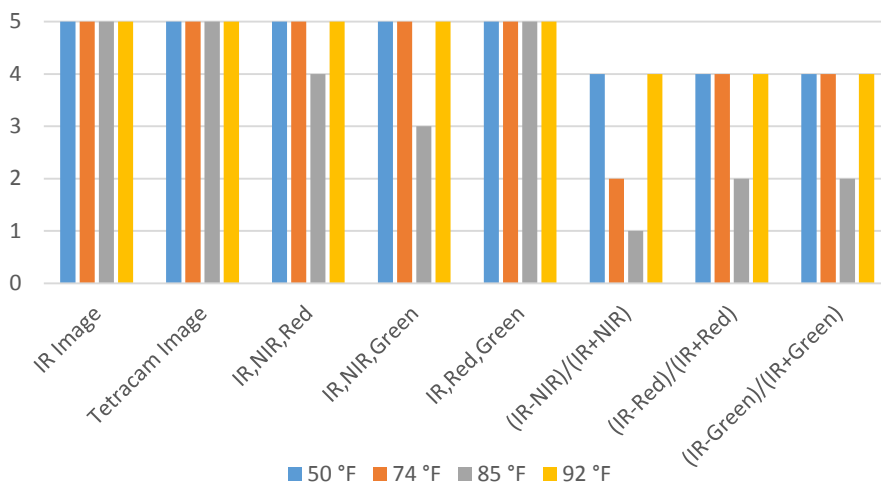


Figure 81. Bar graph representing visibility ranking for the warm-blooded target in front of vegetation

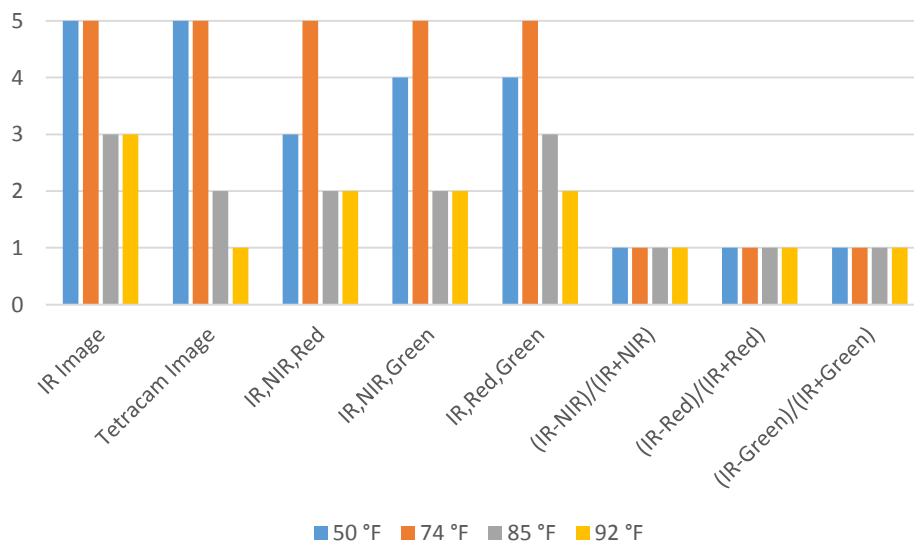


Figure 82. Bar graph representing visibility ranking for the warm-blooded target partially behind the vegetation

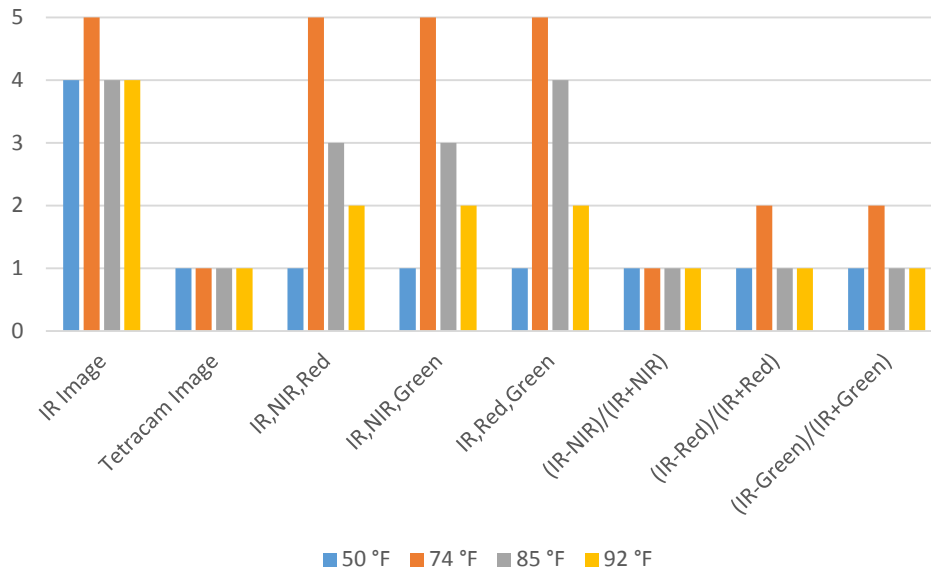


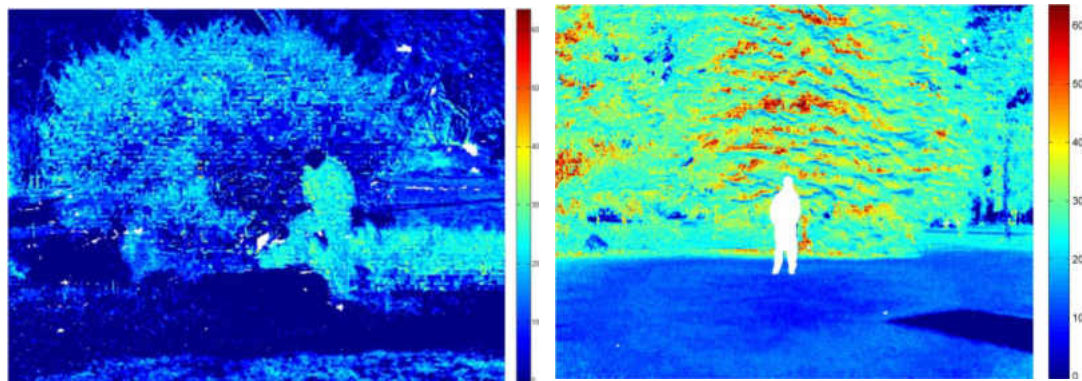
Figure 83. Bar graph representing visibility ranking for the warm-blooded target hiding behind vegetation

The bar graph in Figure 81, Figure 82 and Figure 83 shows that infrared image identifies the warm-blooded target in all temperature in all three cases compared to raw Tetracam and processed images. The normalized difference band ratios often detected the warm-blooded targets in images which were already visible by the Tetracam image alone except at high saturated images.

The spectral image processing for the visibility enhancement test performed such as false color combination and normalized difference band ratio didn't improve the visibility of the warm-blooded target. The infrared image alone was able to show the warm-blooded target independently with high contrast. To display the vegetation health and warm-blooded target in a single image we decided to use the registration of the segmented infrared image on top of NDVI image. The NDVI image will show the health condition of the vegetation and infrared image will show the presence of the warm-blooded target in the scene. All the infrared image sets are segmented using Otsu's threshold method

implemented in MATLAB as discussed in Chapter VI. The segmented infrared red images were overlaid on top of NDVI images with white color to represent the presence of warm-blooded target. Figure 84 through Figure 89 shows the registration of the warm-blooded target on top of NDVI for different temperatures and locations of the warm-blooded target.

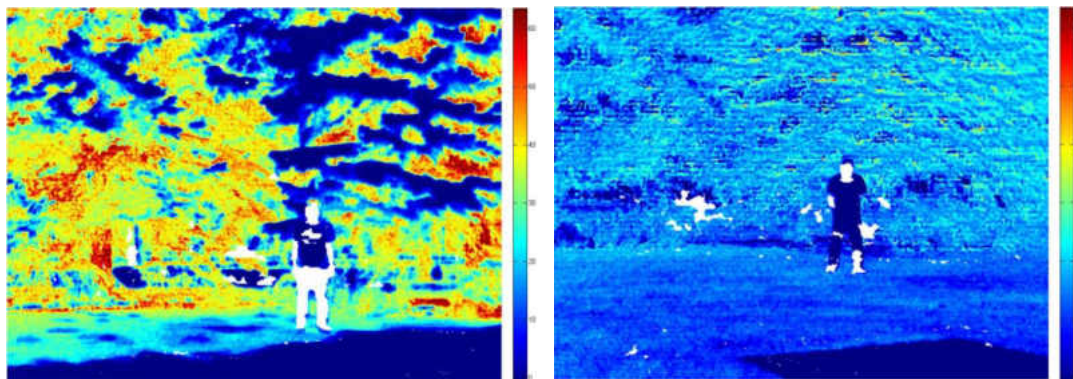
1. Warm-blooded target in front of vegetation



*a) At 50 °F*

*b) At 74 °F*

Figure 84. Registration of segmented infrared image on top of NDVI warm-blooded target in front of vegetation *a) At 50 °F* and *b) At 74 °*



*a) At 85 °F*

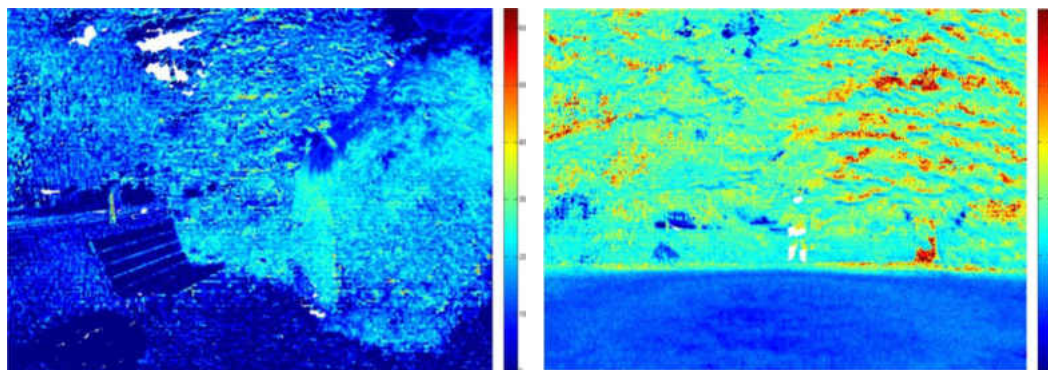
*b) At 92 °F*

Figure 85. Registration of segmented infrared image on top of NDVI warm-blooded target in front of vegetation *a) At 85 °F* and *b) At 92 °F*

When observing the images for the warm-blooded target in front of the vegetation the proposed registration of segmented infrared image was able to truly represent the warm-

blooded target at 74 °F and 85 °F precisely. The images at 50 °F and 92 °F showed that the segmentation method segmented the warm-blooded target along with some false segmented portion including other objects. So, these images have the presence of false targets in the image which was not present in the real scene. When comparing the NDVI portion of the image the image at 50 °F and 85°F showed the presence of healthy and unhealthy vegetation variation. The image at 50 °F showed overall NDVI values almost zero. This image was taken at the end of October, most of the plants were stressed and dead at this time of year. The image at 92 °F also showed the overall NDVI values equal to zero. This image was taken at the evening time when the sun was less illuminated. So the plants were reflecting the nominal amount of near infrared band as compared to the red band.

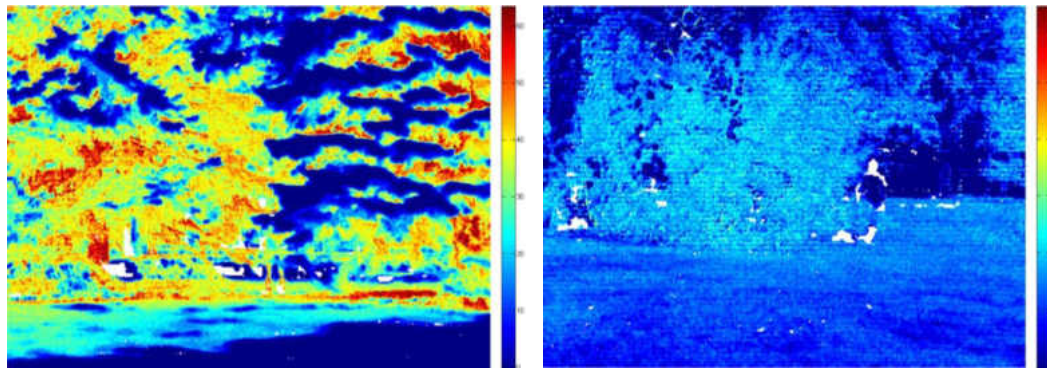
## 2. Warm-blooded target partially covered by vegetation



*a)* At 50 °F

*b)* At 74 °F

Figure 86. Registration of segmented infrared image on top of NDVI for warm-blooded target partially covered by vegetation *a)* At 50 °F and *b)* At 74 °F



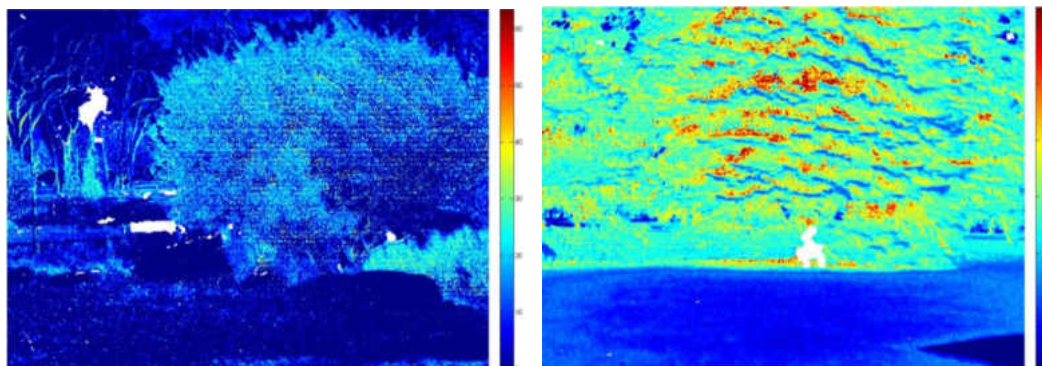
*a) At 85 °F*

*b) At 92 °F*

Figure 87. Registration of segmented infrared image on top of NDVI warm-blooded target partially covered by vegetation *a) At 85 °F* and *b) At 92 °F*

When observing the images for the warm-blooded target partially covered by the vegetation, the Otsu threshold segmentation method was only able to segment truly for the image at 74°F. The image at 50 °F shows the false segmentation of the warm-blooded target. The image at 85 °F which was originally highly saturated has lots of false segmentation compared to all other images. At 92 °F, there are few false segmented images. The NDVI information is same as described for the warm-blooded target in front of the vegetation.

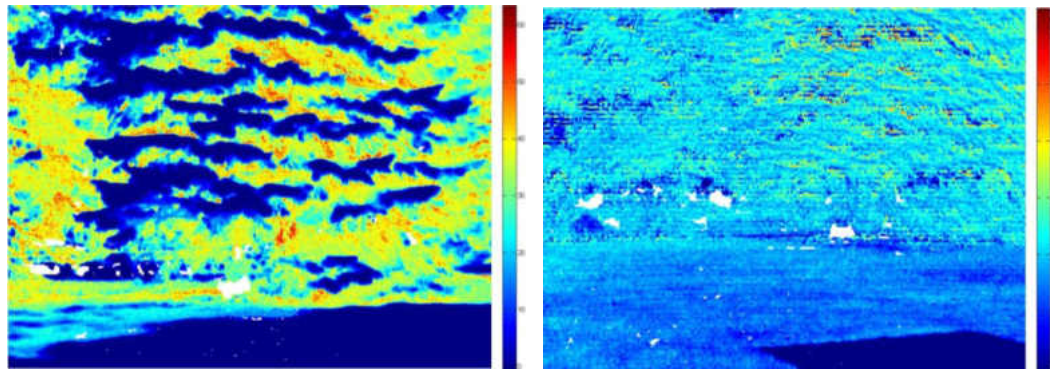
### 3. Warm-blooded target hiding behind the vegetation



*a) At 50 °F*

*b) At 74 °F*

Figure 88. Registration of segmented infrared image on top of NDVI warm-blooded target hiding behind the vegetation *a) At 50 °F* and *b) At 74 °F*



*a) At 85 °F*

*b) At 92 °F*

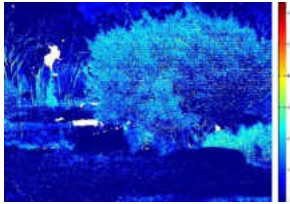
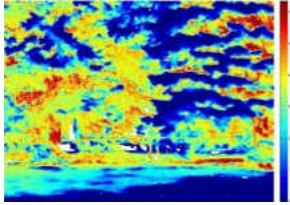
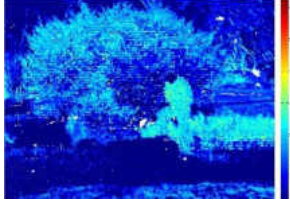
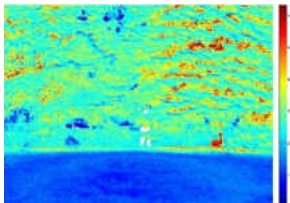
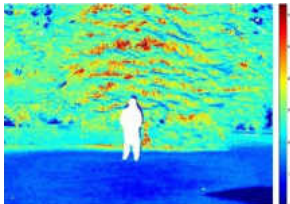
Figure 89. Registration of segmented infrared image on top of NDVI for warm-blooded target hiding behind the vegetation *a) At 85 °F* and *b) At 92 °F*

In the case of warm-blooded target hiding behind the vegetation, the Otsu threshold segmentation method was able to segment the warm-blooded target truly for the image at 74°F and image at 85 °F. The image at 50 °F shows the false segmentation of the warm-blooded target. Which means the segmentation was performed where the warm-blooded animal was not present in the real scene. At 92 °F, there are few false segmented areas along with the true warm-blooded target. The NDVI information is independent of the warm-blooded target location since the infrared image has no interaction in the calculation of the NDVI image. Some part of the NDVI image might be covered by segmented infrared image.

The performance of the registration of segmented infrared image on NDVI method is evaluated based upon how well the segmented area overlapped exactly with the warm-blooded target in the same spatial location. The registration of the false segmented patches is also considered as the criterion for deciding the quality of the image. The images were categorized to rank based on a scale of 1 to 5. Where 1 means the absence of truly segmented area and 5 indicates perfectly segmented warm-blooded target and overlapped

on same spatial location. The 2 scale represents the some patches of the segmented area around the target. The scale of 3 indicates the presence of many segmented patches located at the same spatial location of the target and scale of 4 represents segmented target with the absence of false segmented patches.

Table 10. Ranking rubric for registration of segmented infrared image on top of NDVI.

Rank	Image	Description
1		<ul style="list-style-type: none"> <li>• Absence of segmented warm-blooded animal</li> <li>• False representation of warm-blooded animal</li> </ul>
2		<ul style="list-style-type: none"> <li>• Less false representation of segmented warm-blooded target</li> <li>• Few spots of segmented area corresponding to the location of the warm-blooded animal</li> </ul>
3		<ul style="list-style-type: none"> <li>• Clear view of the warm-blooded target</li> <li>• Few spots of the segmented area which match with the location of warm-blooded animal</li> </ul>
4		<ul style="list-style-type: none"> <li>• Distinct view of the segmented warm-blooded target with less contrast relative to background</li> <li>• Precise location of the segmented warm-blooded target from infrared image on top of NDVI</li> </ul>
5		<ul style="list-style-type: none"> <li>• Distinct view of a warm-blooded animal with high contrast relative to the background.</li> <li>• Precise registration of the warm-blooded target on the same location of NDVI image.</li> </ul>



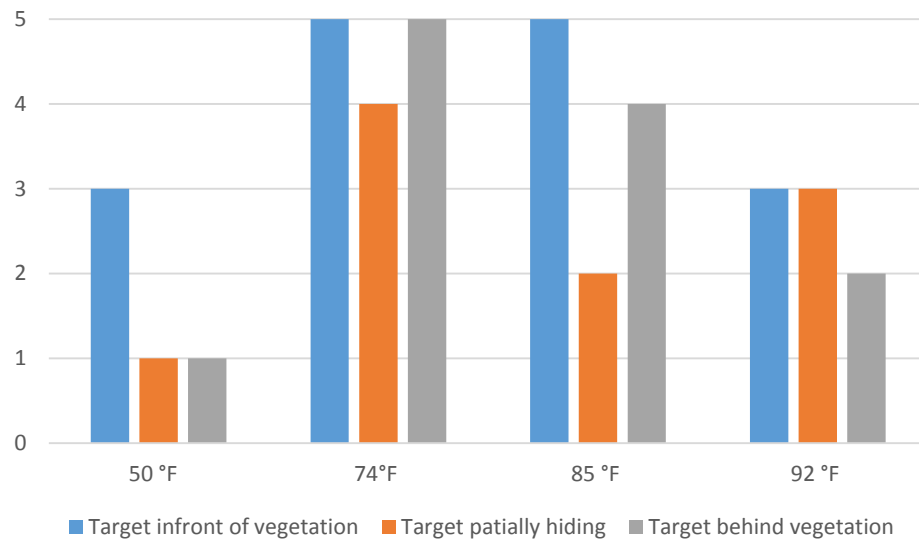


Figure 90. Bar graph representing the ranking of the segmented warm-blooded target registered on top of NDVI.

The bar graph at Figure 90 displays the overall ranking of the proposed image integration method for displaying warm-blooded target and vegetation health in a single image. The bar graph shows that the test data at temperature 74 °F has the highest ranking for the proposed method. At 50 °F, the segmentation method failed to segment the real warm blooded animal in the infrared image with high success. Most of the time the warm-blooded target in front of the vegetation was segmented with high accuracy compared to other test conditions. True registration of the warm-blooded target at the same spatial location in the same NDVI image is highly affected by the segmentation method used. The registration performs well if the warm-blooded target is segmented with high accuracy. The proposed segmentation method tends to extract some the false segmented patches along with warm-blooded targets. To increase the accuracy of the proposed method the better segmentation method should be tested in future work.

## CHAPTER VIII

### CONCLUSIONS & RECOMMENDATIONS

In overall when observing the different processed images for different temperature we found that the visibility of the warm-blooded animal is feasible using just only infrared band image. The visible band is also effective in the low vegetation areas to detect the warm-blooded animals. But in most cases due to nature of defense and self-protection, the animal tends to locate in camouflage environment. For example detection of white bears in the snow using the visible band won't produce a significant result due to camouflage. In very low temperature the infrared band created highly contrast images of the warm-blooded targets but it showed the minimal contrast for the plants and other objects. On the other hand, the single infrared imagery was not able to capture all information from the environment. It needed visible bands assistance to obtain complete information about the vegetation environment.

During days when the temperature reaches around the nominal body temperature of targeted animals. Infrared was not able to capture visible target distinctly image due to the uniform temperature distribution between surrounding and animal body temperature. In these cases if the target is in front of the scene the visible band red was able to detect the target successfully. On high sunlight exposure day times the Tetracam ADC lite multispectral camera couldn't identify the openly exposed warm-blooded target clearly. The cotton fabric was found to be highly reflecting near infrared spectral waves as

compared to the green vegetation [78]. In these cases, the infrared image is required to view the open target more clearly.

The normalized band ratios of the different band didn't enhance the visualization of a warm-blooded animal. The spectral signature of the different animals is strictly necessary to decide which band to pick depending upon the reflectance of the certain species. This might extend the detection abilities based on spectral analysis. On the other hand, there was less spectral anomaly of the warm-blooded animal in the range of the visible to long-wave infrared spectrum. Improving spectral resolution by including more bands in a system and analyzing its behavior over the narrow spectral region might help to get a good understanding of enhancing the visibility based upon spectral image analysis.

Registration of the segmented target from the infrared image on top of the NDVI image was found to be the most efficient image combination tool tested in this research. The plant and animal have a direct relationship in the ecosystem. From this combined image we can locate the green healthy vegetation and also detect the animal and their habitat around this vegetation in a single image. This helps biologists to study the activity of animal with relation to green vegetation.

Overall the ability to integrate multispectral and infrared camera for capturing image data around the same time with same spatial location with minimal disparity is demonstrated successfully in the lab and field operation condition. However, there is a certain limitation on the registration method, the images from two sensors must have some similar landmarks. The simultaneous capture timing of both cameras was tested to confirm the precision. The test showed there is the presence of minimal time lag less than a second.

The more precise quantitative test for capture time is recommended for capturing moving targets. The integrated camera system was able to detect the healthy vegetation as well as a warm-blooded animal at the same location. The visibility of the warm-blooded target was found to be dependent on its location in the vegetated area, illumination from sun, temperature and spectral resolution of the imaging system. Observing the results from the direct raw image comparison, false color combinations and normalized difference band ratios, the optimal condition to collect the data is found to be at moderate sun illumination during low temperature.

The image data used in this research were all collected at ground. In order to collect the aerial data using UAVs. We must consider the limitation of flight time, flight speed of UAV and adjust the elevation for desired resolution of the payload. To improve the spatial alignment of two images the precise calibration of the infrared camera is highly recommended to produce rectified images. The internal integration of the camera systems is complex due to lens and sensor characteristics. But the external integration can be improved by using the camera systems having same sensor size, resolution and field of view. Using infrared camera with the same resolution, same sensor size and field of view compared to multispectral camera will improve the performance of the integrated system. The use of hyperspectral imaging system with many narrow bands is recommended to enhance the detection of the target based on spectral signature.

In conclusion, the integration of two different imaging systems is possible for UAV applications using the procedure described to produce highly aligned imagery. Combination of different spectral sensor together elevates the biological study using UAS.

The future research on spectral behavior of the warm-blooded animal and different vegetation species will uplift the enhanced visualization biological study using UAS.

## APPENDICES


## Appendix A

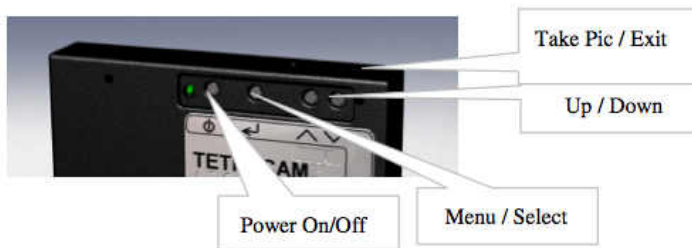
### Payload Operational Manual

#### 1. Tetracam ADC lite continuous capture settings

- i. Connect the Sabrent USB frame grabber to the host laptop through USB interface.
- ii. Connect the Tetracam composite video port to Sabrent USB frame grabber composite video port through RCA cable.



- iii. Turn on the Movavi software and click  icon to view the Tetracam ADC lite preview on the laptop screen.
- iv. Tetracam in video mode press Menu/Select button.



- v. You will see the black screen with the main menu.
- vi. Scroll down to the CAPTURE METHOD and press Menu/Select button.



- vii. Select the SAVE MODE and scroll to choose image format and press Menu/Select button again to come back to the previous menu



- viii. Scroll down to CONT CAPTURE and press Menu/Select button.

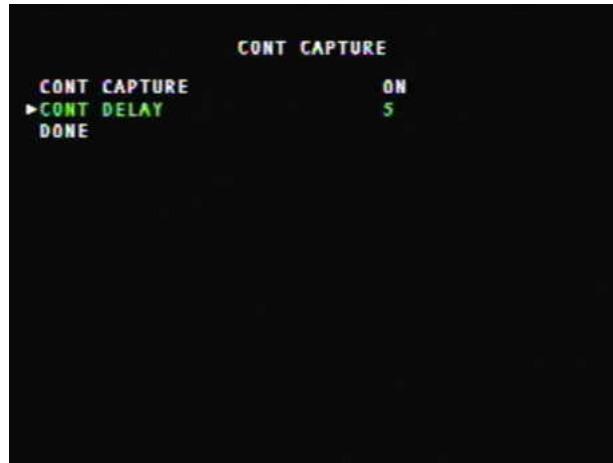


- ix. Select the CONT CAPTURE and scroll to On then press Menu/Select button again to come back to the previous menu



- x. Scroll to CONT DELAY and press Menu/Select button and set the desired delay. The selection can go from 0 to 60 seconds.

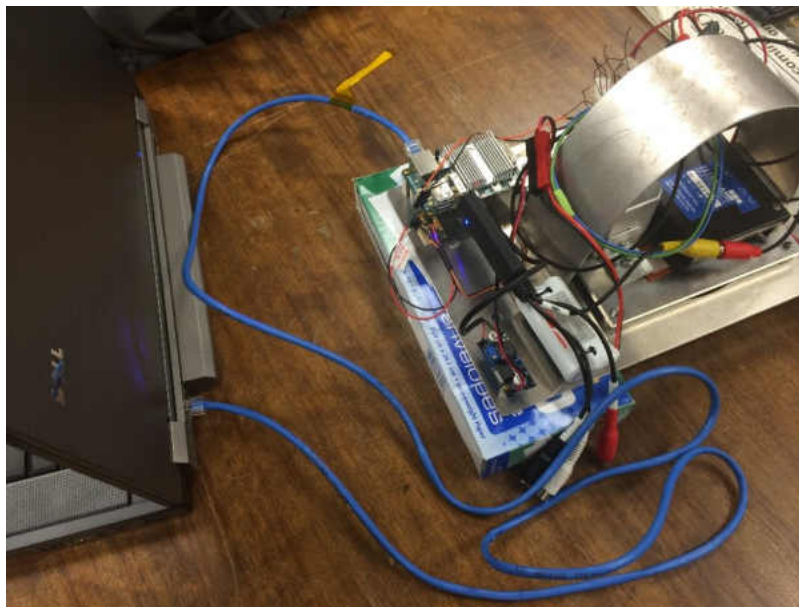




- xii. When you ready to take pictures press the Take pic/Exit button at the top of the camera it will start capturing the continuous RAW format images in given time interval. The process can be stopped by pressing the same button again. Otherwise, it will keep on taking a picture until the CF card space is filled.
- xiii. The pics data will be saved in the camera CF card. Pull off the card and plug into the computer to access the data.

## 2. Connecting Odroid U3 remotely with the host Laptop

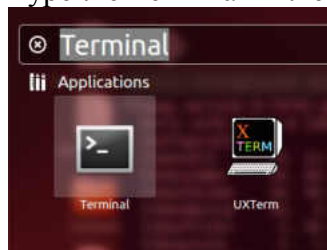
- I. Disconnect the Sabrent frame grabber from the host laptop and connect it to the USB port of the Odroid U3.
- II. Connect the batteries to power up the Tetracam ADC lite, FLIR Photon 320 and Odroid U3.
- III. Connect the RCA cable of the FLIR Photon 320 to the frame grabber yellow female RCA jack.
- IV. After finishing boot process connect the Odroid U3 with the host laptop (Linux operating system) through Ethernet cable.



V. Open the Terminal window on the host laptop.



Click the menu icon on the top left corner of the desktop. Type the Terminal in the search box and select the terminal icon.



- VI. In the Terminal window type  
ssh odroid@192.168.1.11 [Enter]  
For the password type “odroid” without comma and press [Enter]
- VII. The terminal window will show up odroid@odroid as the root directory.

```

odroid@odroid: ~
subin@subin-desktop:~$ ssh odroid@192.168.1.11
odroid@192.168.1.11's password:
Welcome to Ubuntu 14.04.2 LTS (GNU/Linux 3.8.13.30 armv7l)

 * Documentation:  https://help.ubuntu.com/

Last login: Sat Jan  1 11:31:36 2000 from 192.168.1.10
odroid@odroid:~$

```

### 3. Configuring the GPIO (General Purpose Input Output) pins of the Odroid U3

- I. In the root directory type
- II. `cd /sys/class/gpio` [Enter]
- III. `echo 204 > export` [Enter]
- IV. `ls` [Enter] (to see if the gpio 204 is exported)

```

odroid@odroid: /sys/class/gpio
odroid@odroid:~/Desktop$ ls
button.sh      images          ODDROID Utility.desktop  test
capture.sh     ledtest.c      out.mp4             value.sh
commandvar.sh ledtest.sh     README FIRST        while.sh
export         october7.sh   singletest.sh       workedcode
odroid@odroid:~/Desktop$ cd /sys/class/gpio
odroid@odroid:/sys/class/gpio$ ls
export      gpiochip144  gpiochip190  gpiochip245  gpiochip37  gpiochip87
gpiochip0  gpiochip152  gpiochip199  gpiochip25   gpiochip42  gpiochip9
gpiochip105 gpiochip16   gpiochip208  gpiochip254  gpiochip47  gpiochip96
gpiochip114 gpiochip160  gpiochip217  gpiochip263  gpiochip53  unexport
gpiochip121 gpiochip168  gpiochip226  gpiochip272  gpiochip62
gpiochip130 gpiochip177  gpiochip233  gpiochip281  gpiochip69
gpiochip136 gpiochip181  gpiochip238  gpiochip31   gpiochip78
odroid@odroid:/sys/class/gpio$ echo 204 > export
odroid@odroid:/sys/class/gpio$ ls
export      gpiochip136  gpiochip181  gpiochip238  gpiochip31  gpiochip78
gpio204    gpiochip144  gpiochip190  gpiochip245  gpiochip37  gpiochip87
gpiochip0  gpiochip152  gpiochip199  gpiochip25   gpiochip42  gpiochip9
gpiochip105 gpiochip16   gpiochip208  gpiochip254  gpiochip47  gpiochip96
gpiochip114 gpiochip160  gpiochip217  gpiochip263  gpiochip53  unexport
gpiochip121 gpiochip168  gpiochip226  gpiochip272  gpiochip62
gpiochip130 gpiochip177  gpiochip233  gpiochip281  gpiochip69
odroid@odroid:/sys/class/gpio$

```

### 4. Running the Capture Script

Type the following command sequentially

- I. `cd` [Enter] to go to the root directory
- I. `cd Desktop` [Enter] (Takes you to the desktop folder)

- II. ls [Enter] (displays the list of files inside the desktop, you will see capture.sh file in the list)
- III. ./october7.sh [Enter] (runs the capture script)

```

odroid@odroid: ~/Desktop
gpiochip0  gpiochip152  gpiochip199  gpiochip225  gpiochip42  gpiochip9
gpiochip105  gpiochip16  gpiochip208  gpiochip254  gpiochip47  gpiochip96
gpiochip114  gpiochip160  gpiochip217  gpiochip263  gpiochip53  unexport
gpiochip121  gpiochip168  gpiochip226  gpiochip272  gpiochip62
gpiochip130  gpiochip177  gpiochip233  gpiochip281  gpiochip69
gpiochip136  gpiochip181  gpiochip238  gpiochip31  gpiochip78
odroid@odroid:/sys/class/gpio$ echo 204 > export
odroid@odroid:/sys/class/gpio$ ls
export      gpiochip136  gpiochip181  gpiochip238  gpiochip31  gpiochip78
gpio204     gpiochip144  gpiochip190  gpiochip245  gpiochip37  gpiochip87
gpiochip0  gpiochip152  gpiochip199  gpiochip25  gpiochip42  gpiochip9
gpiochip105  gpiochip16  gpiochip208  gpiochip254  gpiochip47  gpiochip96
gpiochip114  gpiochip160  gpiochip217  gpiochip263  gpiochip53  unexport
gpiochip121  gpiochip168  gpiochip226  gpiochip272  gpiochip62
gpiochip130  gpiochip177  gpiochip233  gpiochip281  gpiochip69
odroid@odroid:/sys/class/gpio$ cd
odroid@odroid:~$ cd Desktop
odroid@odroid:~/Desktop$ ls
button.sh  images  ODROID Utility.desktop  test
capture.sh  ledtest.c  out.mp4  value.sh
commandvar.sh  ledtest.sh  README FIRST  while.sh
export      october7.sh  singletest.sh  workedcode
odroid@odroid:~/Desktop$ ./october7.sh

```

## 5. Activating the data capture process

- I. Press the Tetracam ADC lite trigger button to start the data capture process
- II. When the data is captured the screen will fill up with data information as shown in Figure.

```

odroid@odroid: ~/Desktop
ffmpeg version N-74791-g95010d4 Copyright (c) 2000-2015 the FFmpeg developers
built with gcc 4.8 (Ubuntu/Linaro 4.8.2-19ubuntu1)
configuration:
libavutil      54. 31.100 / 54. 31.100
libavcodec     56. 60.100 / 56. 60.100
libavformat    56. 40.101 / 56. 40.101
libavdevice    56.  4.100 / 56.  4.100
libavfilter     5. 40.101 /  5. 40.101
libswscale      3.  1.101 /  3.  1.101
libswresample  1.  2.101 /  1.  2.101
[video4linux2,v4l2 @ 0x100f260] The driver does not permit changing the time per
frame
Input #0, video4linux2,v4l2, from '/dev/video0':
Duration: N/A, start: 946689024.482264, bitrate: 165722 kb/s
Stream #0:0: Video: rawvideo (UYVY / 0x59565955), uyvy422, 720x480, 165722 k
b/s, 29.97 fps, 29.97 tbr, 1000k tbn, 1000k tbc
[swscaler @ 0x1014d40] deprecated pixel format used, make sure you did set range
correctly
Output #0, image2, to '/home/odroid/Desktop/images/image_1.jpg':
Metadata:
encoder      : Lavf56.40.101
Stream #0:0: Video: mjpeg, yuvj422p(pc), 640x480, q=2-31, 200 kb/s, 29.97 fp
s, 29.97 tbn, 29.97 tbc
Metadata:

```

- III. When the data capture is confirmed remove the Ethernet cable.
- IV. The payload is ready for autonomous operation.

## 6. Data transfer from Odroid U3

- I. After finishing the data capture process connect the Ethernet cable again and press ctrl+c to kill the data capture script.
- II. Go to images directory in the Odroid U3 desktop  
cd/Desktop/images [Enter]  
ls [Enter]
- III. You will see the list of images popping up with filenames image\_1. jpg, image\_2.jpg

```

odroid@odroid: ~/Desktop/images
[video4linux2,v4l2 @ 0x100f260] The driver does not permit changing the time per
frame
Input #0, video4linux2,v4l2, from '/dev/video0':
  Duration: N/A, start: 946688805.791876, bitrate: 165722 kb/s
  Stream #0:0: Video: rawvideo (UYVY / 0x59565955), uyvy422, 720x480, 165722 k
b/s, 29.97 fps, 29.97 tbr, 1000k tbn, 1000k tbc
File '/home/odroid/Desktop/images/image_1.jpg' already exists. Overwrite ? [y/N]

Not overwriting - exiting
y
^C
odroid@odroid:~/Desktop$ cd desktop
-bash: cd: desktop: No such file or directory
odroid@odroid:~/Desktop$ ls
button.sh      images          ODROID Utility.desktop  test
capture.sh     ledtest.c      out.mp4                 value.sh
commandvar.sh ledtest.sh     README FIRST           while.sh
export        october7.sh   singletest.sh          workedcode
odroid@odroid:~/Desktop$ cd images
odroid@odroid:~/Desktop/images$ ls
image_10.jpg  image_13.jpg  image_2.jpg  image_5.jpg  image_8.jpg
image_11.jpg  image_14.jpg  image_3.jpg  image_6.jpg  image_9.jpg
image_12.jpg  image_1.jpg   image_4.jpg  image_7.jpg
odroid@odroid:~/Desktop/images$

```

- IV. Shut down the Odroid U3.  
sudo shutdown now [Enter]  
Type the password “odroid” [Enter]
- V. The captured FLIR Photon 320 images are saved in the image folder of the Odroid U3 desktop.
- VI. Connect the Odroid U3 to the monitor with the micro HDMI cable also connect the mouse and keyboard to operate as a stand-alone system.
- VII. Connect the USB flash drive and copy the images folder from the Odroid U3 desktop.

#### 7. Data transfer from Tetracam ADC lite

- I. Remove the CF card from the camera.
- II. Insert the CF card to the computer card reader.
- III. Copy the RAW files to the computer.

## Appendix B

### Software Configuration for Odroid U3

#### 1. Install FFMPEG

- I. Go to the FFmpeg Website and copy the gitclone address
- II. Paste the address in Linux terminal [Enter]
- III. `cd ffmpeg` [Enter]
- IV. `./configure` [Enter]
- V. `make` [Enter]
- VI. `sudo make install`

#### 2. Checking the USB Camera image capture test

- I. Open the Terminal command window
- II. `lsusb` [Enter]
- III. Checking for video device
  - a. `ls /dev/video*` [Enter]
- IV. Installing v4l2
  - a. `sudo apt-get install v4l-utils` [Enter]
- V. Using ffmpeg to capture video
  - a. `ffmpeg -f v4l2 -framerate 10 -i /dev/video0 out.avi`

#### 3. Configuration to connect host laptop with Odroid U3 through Ethernet cable

- I. Set Static IP in odroid U3
  - a) Open the Terminal command window
  - b) Go to directory  
`cd /etc/network` [Enter]
  - c) Edit the file name *interfaces*  
`sudo nano interfaces` [enter]  
add following lines in the text documents  
auto lo  
iface lo inet loopback  
auto eth0  
iface eth0 inet static  
address 192.168.1.11  
gateway 192.168.1.1  
netmask 255.255.255.0

Save and exit

- II. Change the Ethernet IP address of laptop to 192.168.1.10
- III. Connecting Odroid with host laptop using ssh command  
`ssh odroid@192.168.1.11` [Enter]

#### 4. Running VNC server to view the remote desktop using Ethernet cable

- I. Open the Terminal command window
- II. Install vncviewer in laptop  
sudo apt-get install xtightvncviewer [Enter]
- III. Install vnc server in Odroid U3  
sudo apt-get install tightvncserver [Enter]
- IV. Run tightvncserver in Odroid  
tightvncserver [Enter]
- V. Give password and set up the remote desktop parameters  
vncserver :1 -geometry 1280x1080 -depth 24 -dpi96 [Enter]
- VI. Connect odroid remotely using ssh  
ssh odroid@192.168.1.11 [Enter]
- VII. Run tight xtightvncviewer in laptop
- VIII. Give IP address 192.168.1.11:1
- IX. Enter the password bestofluck
- X. After entering the password you will see remote desktop of Odroid in the laptop

#### 5. Linux Shell Script for capturing still images from Flir Photon 320 infrared camera with triggering of Tetracam ADC lite

```
#!/bin/bash
cd /sys/class/gpio
cd gpio204
echo in > direction
count=1
while true
do
output=$(cat /sys/class/gpio/gpio204/value)
if test $output == 1
then
ffmpeg -f v4l2 -framerate 25 -i /dev/video0 -vf scale= 640:480
/home/odorid/Desktop/images/image_ $count.jpg
while (( $output == 1))
do
output=$(cat /sys/class/gpio/gpio204/value)
done
count=$((count+1))
fi
done
```

## Appendix C

### Tuning Mechanical Alignment

#### Tuning Mechanical Alignment

After finishing all the connection, set up the target board at a known distance and warm up the heating wire by connecting the cable to the wall plug.



1. Use Movavi Video Editor 8 SE software to take the still Image

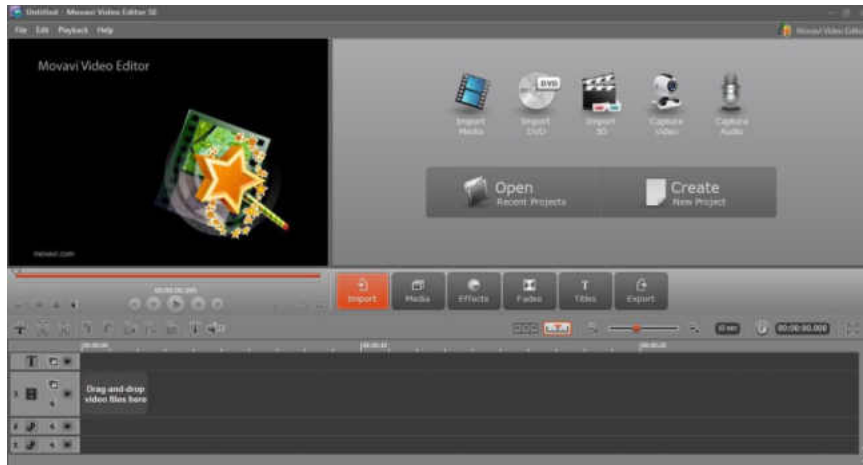
I. Insert the Sabrent USB 2.0 frame grabber into the laptop USB port.




II. Double Click the Movavi Video Editor 8SE icon located on Desktop

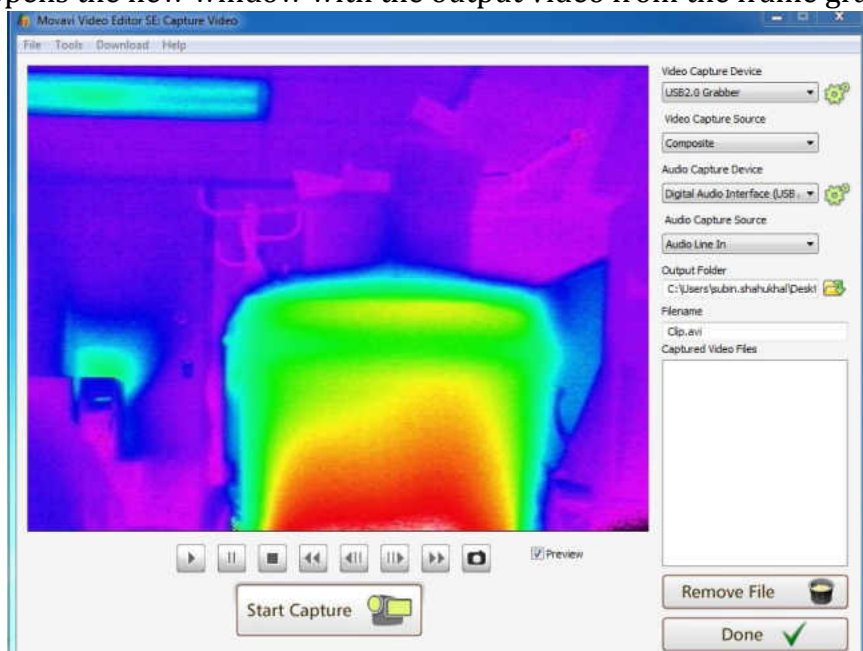
III. When the Movavi launches it shows the following screen

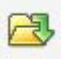


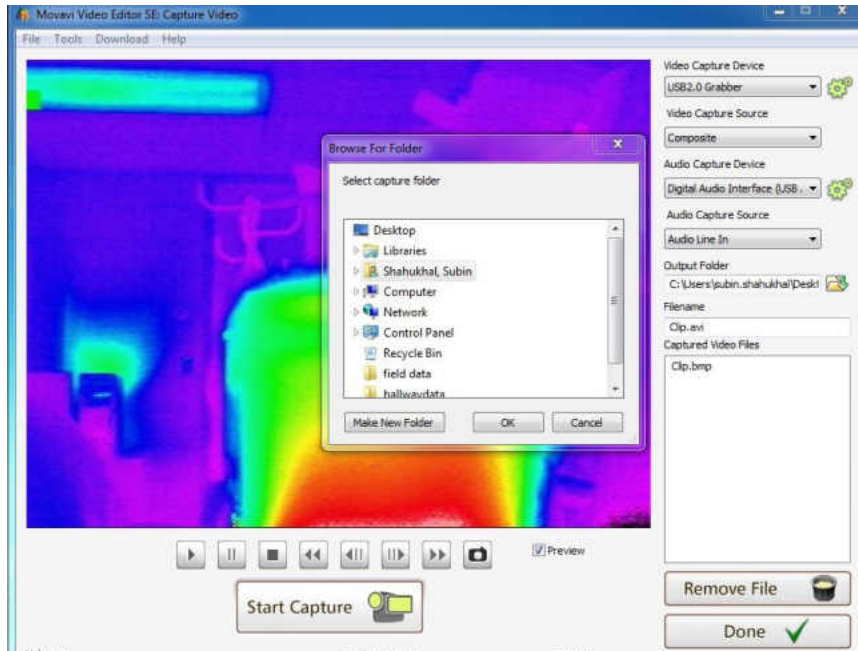



IV. Double click the  Capture Video icon on the left

V. It opens the new window with the output video from the frame grabber.



VI. Click the  button to browse the folder where you want to save the image or video



- VII. Click the  button to take the still image of the current preview. It will automatically save the still images in the BMP format in the selected folder with a clip as default filename.
- VIII. Without moving the camera tripod press the trigger button of the Tetracam ADC lite.
- IX. Transfer the Tetracam image from CF memory card to computer and color process from RAW format to jpeg format.

## 2. Image processing using MATLAB to find the pixel offset.

- I. Open up the MATLAB software.
- II. Put the picture files to be compared in the same folder and use the following command to overlap the images. **NOTE:** (the images must be of same sizes if not, you need to scale either one to match the size)

Example:

If you want to compare 2 images tetra1.jpg and flir1.jpg taken from Tetracam ADC lite and FLIR Photon 320 respectively and find the pixel offset.

- a) Save the both picture in the same folder.
- b) Now type the following command in command window as shown in picture.
 

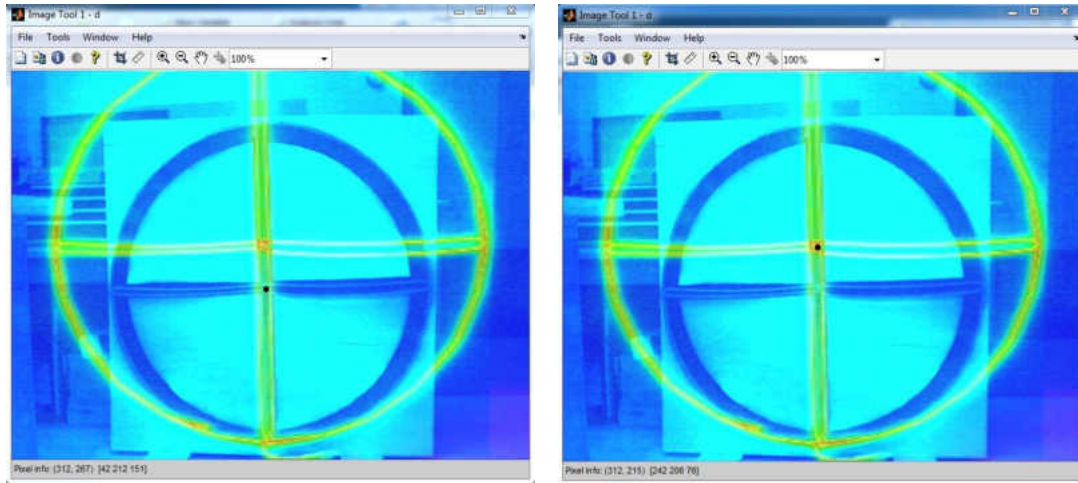
```
>> Tetracam_image= imread('tetra1.jpg');
```

```

>> b=imread('flir1.jpg');
>> Flir_image=imresize(b, 3.2);
>> Added_image= imadd(Tetracam_image,Flir_image);
>> imtool(Added_image);

```

III. Hit enter, the new window named Image Tool appear with overlapped image.



- IV. In Image tool window point the mouse cursor at the vertical line at the center of the board as a reference in Tetracam image and list the pixel coordinate displayed at the bottom of the window. Pixel info: (312, 267) [42 212 151]
- V. Now point the mouse cursor at center of target board in Flir image and list the pixel coordinate. Pixel info: (312, 215) [242 206 76]
- VI. Subtract the pixel coordinates to get the pixel offset in the image. In this example, we have same x pixel coordinate and different y pixel coordinate. Subtracting those two numbers we get  $(267-215=52)$  pixel offset) in the y direction. If the pixel value is same for the X coordinate on both image for the vertical line and center point then tuning is complete.

## Mounting Plate Deflection Analysis results

1g Acceleration										
Plate Thickness	F1 (inch)	F2 (inch)	T1 (inch)	T2 (inch)	Net Flir deflection	Net Tetra Deflection	Flir offset	Tetraoffset	Net offset	
0.08	1.28E-04	1.63E-04	1.20E-04	2.41E-04	3.53E-05	1.21E-04	0.0460845	0.311227419	0.357311917	
0.1	6.69E-05	8.52E-05	6.29E-05	1.25E-04	1.83E-05	6.24E-05	0.0238843	0.161117042	0.185001345	
0.125	3.52E-05	4.47E-05	3.31E-05	6.55E-05	9.51E-06	3.24E-05	0.01241932	0.083636722	0.096056037	
0.16	1.75E-05	2.21E-05	1.64E-05	3.22E-05	4.64E-06	1.58E-05	0.00605365	0.040678717	0.046732366	
0.19	1.08E-05	1.36E-05	1.01E-05	1.97E-05	2.82E-06	9.57E-06	0.00368154	0.024697885	0.028379422	
3g Acceleration										
Plate Thickness	F1 (inch)	F2 (inch)	T1 (inch)	T2 (inch)	Net Flir deflection	Net Tetra Deflection	Flir offset	Tetra offset	Net offset	
0.08	3.81E-04	4.86E-04	3.60E-04	7.19E-04	1.05E-04	3.59E-04	0.13767907	0.926867623	1.064546692	
0.1	1.99E-04	2.54E-04	1.88E-04	3.74E-04	5.47E-05	1.86E-04	0.07137222	0.479786351	0.551158575	
0.125	1.05E-04	1.33E-04	9.91E-05	1.96E-04	2.84E-05	9.65E-05	0.03710259	0.249074862	0.286177452	
0.16	5.20E-05	6.58E-05	4.91E-05	9.60E-05	1.39E-05	4.69E-05	0.01808131	0.121091395	0.139172706	
0.19	3.21E-05	4.05E-05	3.03E-05	5.88E-05	8.42E-06	2.85E-05	0.01099631	0.073515442	0.084511752	
5g Acceleration										
Plate Thickness	F1 (inch)	F2 (inch)	T1 (inch)	T2 (inch)	Net Flir deflection	Net Tetra Deflection	Flir Offset	Tetra offset	Net offset	
0.08	6.35E-04	8.10E-04	6.00E-04	1.20E-03	1.76E-04	5.98E-04	0.2292867	1.544263111	1.773549807	
0.1	3.32E-04	4.23E-04	3.14E-04	6.23E-04	9.10E-05	3.10E-04	0.11885362	0.799402997	0.918256614	
0.125	1.75E-04	2.22E-04	1.65E-04	3.26E-04	4.73E-05	1.61E-04	0.06180284	0.414995705	0.476798541	
0.16	8.66E-05	1.10E-04	8.18E-05	1.60E-04	2.31E-05	7.82E-05	0.03011289	0.201751877	0.231864767	
0.19	5.34E-05	6.75E-05	5.05E-05	9.79E-05	1.40E-05	4.75E-05	0.01831239	0.122487878	0.140800265	

## Appendix D

### MATLAB Image Processing Codes

#### 1. Image registration

```
source = imread('source.bmp'); % Reads Flir Image as a source image
target = imread('target.jpg'); % Reads Tetracam Image as a destination
image

cpselect(source,target)% Opens up window to select control points

% Computation of affine transformation matrix using control points
tform= fitgeotrans(movingPoints,fixedPoints,'affine');

% Warping of image using affine transformation matrix
registered = imwarp(source,tform,'OutputView',imref2d(size(target)));

falsecolorOverlay = imfuse(target,registered); % Overlays two images
figure
imshow(falsecolorOverlay,'InitialMagnification','fit');
```

#### 2. False color combinations and Normalized Difference Band Ratios

```
%% Reads Tetracam Image and warped FLIR image.

Tetra=im2double(Tetra1.jpg);
NIR=Tetra(:,:,1); % NIR channel of Tetra cam
Red=Tetra(:,:,2); % Red channel of Tetra cam
Green=Tetra(:,:,3); % Green channel of Tetra cam
Flir=rgb2gray(Flir1.jpg);
IR=im2double(Flir);

%% 1. False color combination of IR, NIR and Red
Comb1=cat(3,IR,NIR,Red);
figure, imshow(Comb1)
print('IR,NIR,RED','-djpeg','-r600')

%% 2. False color combination of IR, NIR and Green
Comb2=cat(3,IR,NIR,Green);
figure, imshow(Comb2)
print('IR,NIR,Green','-djpeg','-r600')

%% 3. False color combination of IR,RED,Green
Comb3=cat(3,IR,Red,Green);
figure, imshow(Comb3)
print('IR,RED,Green','-djpeg','-r600')

%%Calculation of Image Indices

%% Index 1. Calculation of NDVI
Num1= NIR-Red;
```

```

Den1= NIR+Red;
NDVI=(Num1./Den1);
figure, imshow(NDVI);
colormap(jet)
colorbar
print('NDVI', '-djpeg', '-r600')

%% Index2. (IR-NIR/IR+NIR)
Num2=IR-NIR;
Den2=IR+NIR;
Ratio2=(Num2./Den2);
figure, imshow(Ratio2);
colormap(jet)
colorbar
print('Index2IR-NIR', '-djpeg', '-r600')

%% Index3 (IR-Red/IR+Red)
Num3=IR-Red;
Den3=IR+Red;
Ratio3=(Num3./Den3);
figure, imshow(Ratio3);
colormap(jet)
colorbar
print('Index3IR-RED', '-djpeg', '-r600')

%% Index4 (IR-Green/IR+Green)
Num4=IR-Green;
Den4=IR+Green;
Ratio4=(Num4./Den4);
figure, imshow(Ratio4);
colormap(jet)
colorbar
print('Index4IR-Green', '-djpeg', '-r600')

%% Index5 (Red-Green/Red+Green)
Num5=IR-Green;
Den5=IR+Green;
Ratio5=(Num5./Den5);
figure, imshow(Ratio5);
colormap(jet)
colorbar
print('Index5RED-Green', '-djpeg', '-r600')

%% Index6 (NIR-Green/NIR+Green)
Num6=NIR-Green;
Den6=NIR+Green;
Ratio5=(Num6./Den6);
figure, imshow(Ratio5);
colormap(jet)
colorbar
print('Index6NIR-Green', '-djpeg', '-r600')

```

### 3. Segmentation of Infrared Image and registering on top of NDVI

%% This section segments the target in the infrared image from background Using Otsu Threshold method from MATLAB Example

```
clear all;
close all;
clc
a= imread ('Flir1.jpg');
I=rgb2gray(a);
figure, imshow(I), title('original image');
[~, threshold] = edge(I, 'sobel');
fudgeFactor = .5;
BWs = edge(I, 'sobel', threshold * fudgeFactor);
figure, imshow(BWs), title('binary gradient mask');
se90 = strel('line', 3, 90);
se0 = strel('line', 3, 0);
BWsdil = imdilate(BWs, [se90 se0]);
figure, imshow(BWsdil), title('dilated gradient mask');
BWdfill = imfill(BWsdil, 'holes');
figure, imshow(BWdfill);
title('binary image with filled holes');
BWnobord = imclearborder(BWdfill, 4);
figure, imshow(BWnobord), title('cleared border image');
seD = strel('diamond',1);
BWfinal = imerode(BWnobord,seD);
BWfinal = imerode(BWfinal,seD);
figure, imshow(BWfinal)
```

%% This Section reads Tetracam Image and segmented Flir image

```
IR=im2double(BWfinal); % Read segmented infrared image
Tetra =imread('Tetra1.jpg'); %Read Tetracam image
Tetra_sep=im2double(Tetra);
NIR=Tetra_sep(:,:,1); % NIR channel of Tetra cam
Red=Tetra_sep(:,:,2); % Red channel of Tetra cam
Green=Tetra_sep(:,:,3); % Green channel of Tetra cam
```

%% Overlays the Infrared Image on Top of NDVI as Red color

```
Blank=zeros(1536,2048);
Num1= NIR-Red;
Den1= NIR+Red;
NDVI=(Num1./Den1);
b=NDVI+IR;
figure, imshow(b)
colormap jet
colorbar
```

%% Overlays Infrared Image on Top of NDVI as white color

```
I1=im2uint8(NDVI);
I2=im2uint8(IR);
imwrite(I1,jet,'mylast.jpg')
imwrite(I2,gray,'mylastir.jpg')
NDVI_P=imread('mylast.jpg');
IR_P=imread('mylastir.jpg');
b=NDVI_P+IR_P;
figure, imshow(b)
```

```
colorbar
```

#### 4. Straight line test for the undistortion applied to the Flir Photon 320 image

```
clear all;
close all;
clc
a=imread('original_image.jpg'); % Reads the Flir Photon 320 image
b = rgb2gray(a); % Converts to grayscale
cannyedge=edge(b, 'canny',0.62361); % canny edge detection
imtool(cannyedge)
cropped=cannyedge(15:25,96:523); % Cropping of interested region of
line
imshow(cropped);

[m,n] = size(cropped);

pixels=[];

for ii=1:11
    for jj=1:428
        if (cropped(ii,jj)==1)
            pixels=[pixels;ii+14 jj+95];
        end
    end
end

x=pixels(:,2);
Xsort=sort(x);
X=[ones(length(pixels),1) pixels(:,2)];
y=pixels(:,1);
b = X\y
yCalc2=X*b;
Error= (y-yCalc2);
Maxerror= max(Error)
Rsqr = 1 - sum((y - yCalc2).^2)/sum((y - mean(y)).^2) % coefficient of
determination
```



## REFERENCES

- [1] Haarbrink, R. "UAS for geo-information: current status and perspectives." *ISPRS–Int.Arch. Photogramm. Remote Sens. Spatial Inform. Sci* 38.1 (2011): C22.
- [2] Argrow, Brian, Dale Lawrence, and Erik Rasmussen. "UAV systems for sensor dispersal, telemetry, and visualization in hazardous environments." *43rd Aerospace Sciences Meeting and Exhibit*. Vol. 4. 2005.
- [3] Johnson, Andrew, James Montgomery, and Larry Matthies. "Vision guided landing of an autonomous helicopter in hazardous terrain." *Robotics and automation, 2005. ICRA 2005. Proceedings of the 2005 IEEE international conference on*. IEEE, 2005.
- [4] Hinkley, Everett A., et al. "Small UAS Demonstration for Wildfire Surveillance." (2007).
- [5] Frew, Eric W., and Timothy X. Brown. "Networking issues for small unmanned aircraft systems." *Journal of Intelligent and Robotic Systems* 54.1-3 (2009): 21-37.
- [6] Hill, Samuel, and Peter Clemens. "Miniaturization of sub-meter resolution hyperspectral imagers on unmanned aerial systems." *SPIE Sensing Technology+ Applications*. International Society for Optics and Photonics, 2014.
- [7] Smith, Randall B. "Introduction to remote sensing of environment (RSE)." *MicroImages, Inc., 11th Floor, Sharp Tower* 206 (2001): 68508-2010.
- [8] Blackwell, Bradley F., et al. "Use of infrared technology in wildlife surveys." *Proceedings of the 22nd Vertebrate Pest Conference*. Vol. 22. 2006.
- [9] Christiansen, Peter, et al. "Automated detection and recognition of wildlife using thermal cameras." *Sensors* 14.8 (2014): 13778-13793.
- [10] Haschberger, Peter, Michael Bundschuh, and Volker Tank. "Infrared sensor for the detection and protection of wildlife." *Optical Engineering* 35.3 (1996): 882-889.
- [11] Gade, Rikke, and Thomas B. Moeslund. "Thermal cameras and applications: A survey." *Machine vision and applications* 25.1 (2014): 245-262.
- [12] van Gemert, Jan C., et al. "Nature Conservation Drones for Automatic Localization and Counting of Animals." *Computer Vision-ECCV 2014 Workshops*. Springer International Publishing, 2014.

- [13] Chrétien, L. P., J. Théau, and P. Ménard. "Wildlife Multispecies Remote Sensing Using Visible and Thermal Infrared Imagery Acquired from AN Unmanned Aerial Vehicle (uav)." *ISPRS-International Archives of the Photogrammetry, Remote Sensing and Spatial Information Sciences* 1 (2015): 241-248.
- [14] Nebiker, S., et al. "A light-weight multispectral sensor for micro UAV—Opportunities for very high resolution airborne remote sensing." *The international archives of the photogrammetry, remote sensing and spatial information sciences* 37 (2008): 1193-1200.
- [15] Stagakis, S., et al. "Monitoring water stress and fruit quality in an orange orchard under regulated deficit irrigation using narrow-band structural and physiological remote sensing indices." *ISPRS Journal of Photogrammetry and Remote Sensing* 71 (2012): 47-61.
- [16] Panigada, C., et al. "Remote sensing of vegetation status using hyperspectral data." *Proceedings of Hyperspectral 2010 Workshop*. 2010.
- [17] Baldeck, C. A., et al. "Landscape-scale variation in plant community composition of an African savanna from airborne species mapping." *Ecological Applications* 24.1 (2014): 84-93.
- [18] Torres-Sánchez, Jorge, et al. "Configuration and specifications of an unmanned aerial vehicle (UAV) for early site-specific weed management." (2013): e58210.
- [19] Berni, Jose AJ, et al. "Thermal and narrowband multispectral remote sensing for vegetation monitoring from an unmanned aerial vehicle." *Geoscience and Remote Sensing, IEEE Transactions on* 47.3 (2009): 722-738.
- [20] Bendig, Juliane, Andreas Bolten, and G. Bareth. "Introducing a low-cost mini-UAV for thermal-and multispectral-imaging." *Int. Arch. Photogramm. Remote Sens. Spat. Inf. Sci* 39 (2012): 345-349.
- [21] Turner, Darren, et al. "Spatial co-registration of ultra-high resolution visible, multispectral and thermal images acquired with a micro-UAV over Antarctic Moss Beds." *Remote Sensing* 6.5 (2014): 4003-4024.
- [22] Heinold, S. "Tetracam ADC Installation and Operation," rev. 1.7, Tetracam Inc, 2008.
- [23] FLIR Systems, Inc. "Photon User's Manual" 2008
- [24] "Landsat 8." Landsat Science. NASA. Web. 25 Nov. 2015.  
<<http://landsat.gsfc.nasa.gov/?p=3186>>
- [25] Eastman, J. Ronald. "Guide to GIS and Image Processing Volume." *Clark University. USA* (2001).
- [26] FLIR Systems, Inc. "The Ultimate Infrared Handbook for R&D Professionals"

- [27] Dvorak, David. "Development and Demonstration of an Unmanned Aircraft Based Precision Agriculture Imaging System," M.S. thesis. University of North Dakota, 2011. Print.
- [28] Sheng, Yunlong, et al. "Real-world multisensor image alignment using edge focusing and Hausdorff distances." *AeroSense'99*. International Society for Optics and Photonics, 1999.
- [29] Shaw, Gary A., and Hsiao-hua K. Burke. "Spectral imaging for remote sensing." *Lincoln Laboratory Journal* 14.1 (2003): 3-28.
- [30] Gates, David M., et al. "Spectral properties of plants." *Applied optics* 4.1 (1965): 11-20.
- [31] Govaerts, Bram, and Nele Verhulst. "The normalized difference vegetation index (NDVI) GreenSeekerTM handheld sensor." (2010).
- [32] "An Introduction to Multispectral Imaging and How Growers and Other Users Benefit from This Technology." Tetracam Multispectral Application Notes. Tetracam Inc. Web. 26 Nov. 2015. <<http://www.tetracam.com/MS Database.htm>>.
- [33] "Tetracam ADC - Frequently Asked Questions." Tetracam Inc. Web. 25 Nov. 2015. <<http://www.tetracam.com/PDFs/ADC FAQ.pdf>>.
- [34] "Frequently Asked Questions about the Landsat Missions." What Are the Band Designations for the Landsat Satellites? U.S. Geological Survey, 19 June 2014. Web. 25 Nov. 2015. <[http://landsat.usgs.gov/band\\_designations\\_landsat\\_satellites.php](http://landsat.usgs.gov/band_designations_landsat_satellites.php)>.
- [35] Bhan, R. K., et al. "Uncooled Infrared Microbolometer Arrays and their Characterisation Techniques (Review Paper)." *Defence Science Journal* 59.6 (2009): 580-589.
- [36] "Tau 2 Uncooled Cores." Tau 2 LWIR Camera Cores. FLIR Systems, Inc. Web. 26 Nov. 2015. <<http://www.flir.com/cores/display/?id=54717>>.
- [37] "ODROID Platforms." ODROID. Hardkernel Co., Ltd. Web. 26 Nov. 2015. <[http://www.hardkernel.com/main/products/prdt\\_info.php?g\\_code=g138745696275&tab\\_idx=1](http://www.hardkernel.com/main/products/prdt_info.php?g_code=g138745696275&tab_idx=1)>.
- [38] USB 2.0 VIDEO & AUDIO CAPTURE DVD MAKER. Sabrent. Web. 26 Nov. 2015. <<http://www.sabrent.com/category/video-converters/USB-AVCPT/>>.
- [39] RioRand Advanced Technology. Web. 26 Nov. 2015. <<http://www.riorand.com/riorand-lm2596-dc-dc-buck-converter-step-down-module-power-supply-output-1-23v-30v-1pcs-lm2596.html>>.
- [40] Bosak, Krzysztof. Secrets of UAV photomapping. Technical report, Pteryx UAV by Trigger Composites, 2012

- [41] Soderstrom, Neil. *Deer-resistant Landscaping: Proven Advice and Strategies for Outwitting Deer and 20 Other Pesky Mammals*. Rodale, 2009.
- [42] "Choosing a Digital Camera - Mac-Forums Blog." MacForums Blog. 24 May 2012. Web. 26 Nov. 2015. <<http://www.mac-forums.com/blog/choosing-a-digital-camera-2/>>.
- [43] Fullerton, Eric. "A Step-by-step Guide to Lens Parameters and Calculations for Video Surveillance Cameras." *Lens Calculations – Do the Math*. Milestone Systems, 2009. Web. 29 Nov. 2015. <<http://vdss.ca/milestone/12.pdf>>.
- [44] Paine, David P., and James D. Kiser. *Aerial photography and image interpretation*. John Wiley & Sons, 2012.
- [45] Crum, William R., Thomas Hartkens, and D. L. G. Hill. "Non-rigid image registration: theory and practice." *The British Journal of Radiology* (2014).
- [46] Zitova, Barbara, and Jan Flusser. "Image registration methods: a survey." *Image and vision computing* 21.11 (2003): 977-1000.
- [47] Cabani, Cristina. *Implementation of an Affine-Invariant Feature Detector in Field-Programmable Gate Arrays*. Diss. University of Toronto, 2006.
- [48] Szeliski, Richard. *Computer vision: algorithms and applications*. Springer Science & Business Media, 2010.
- [49] Bouguet, Jean-Yves. "Camera calibration toolbox for matlab." (2004).
- [50] Heikkila, Janne, and Olli Silvén. "A four-step camera calibration procedure with implicit image correction." *Computer Vision and Pattern Recognition, 1997. Proceedings., 1997 IEEE Computer Society Conference on*. IEEE, 1997.
- [51] Zhang, Zhengyou. "Flexible camera calibration by viewing a plane from unknown orientations." *Computer Vision, 1999. The Proceedings of the Seventh IEEE International Conference on*. Vol. 1. IEEE, 1999.
- [52] Tsai, R. Y. (1987) A versatile camera calibration technique for high-accuracy 3D machine vision metrology using off the-shelf TV cameras and lenses. *IEEE Journal of Robotics and Automation* RA-3(4): 323-344.
- [53] Zhang, Lizi. *Camera calibration*. Aalborg University. Department of Communication Technology, 2001.
- [54] Abdel-Aziz, Y. I., and H. M. Karara. "Direct Linear Transformation from Comparator Coordinates into Object Space Coordinates in Close-Range Photogrammetry." *Photogrammetric Engineering & Remote Sensing* 81.2 (2015): 103-107.

- [55] Duane, C. BROWN. "Close-range camera calibration." *Photogram. Eng. Remote Sens* 37 (1971): 855-866.
- [56] Wei, Guo-Qing, and Song De Ma. "Implicit and explicit camera calibration: Theory and experiments." *Pattern Analysis and Machine Intelligence, IEEE Transactions on* 16.5 (1994): 469-480.
- [57] Slama, Chester C., Charles Theurer, and Soren W. Henriksen. *Manual of photogrammetry*. No. Ed. 4. American Society of photogrammetry, 1980.
- [58] "Thermal Conductivity of Materials and Gases." The Engineering Toolbox. Web. 26 Nov. 2015.
- [59] Canny, John. "A computational approach to edge detection." *Pattern Analysis and Machine Intelligence, IEEE Transactions on* 6 (1986): 679-698.
- [60] Datta, Ankur, Jun-Sik Kim, and Takeo Kanade. "Accurate camera calibration using iterative refinement of control points." Computer Vision Workshops (ICCV Workshops), 2009 IEEE 12th International Conference on. IEEE, 2009.
- [61] Rudakova, Victoria, and Pascal Monasse. "Camera matrix calibration using circular control points and separate correction of the geometric distortion field." Computer and Robot Vision (CRV), 2014 Canadian Conference on. IEEE, 2014.
- [62] Mallon, John, and Paul F. Whelan. "Which pattern? biasing aspects of planar calibration patterns and detection methods." *Pattern recognition letters* 28.8 (2007): 921-930.
- [63] "Tetracam Multi-IO Cables and Connectors." Tetracam Inc. Web. 26 Nov. 2015. <[http://www.tetracam.com/Multi-IO Connections.htm](http://www.tetracam.com/Multi-IO%20Connections.htm)>.
- [64] Lee, Edward Ashford, and Sanjit Arunkumar Seshia. *Introduction to embedded systems: A cyber-physical systems approach*. Lee & Seshia, 2011. 230-234. Print.
- [65] "Voltage Divider Calculator." Learning about Electronics. Web. 26 Nov. 2015. <<http://www.learningaboutelectronics.com/Articles/Voltage-divider-calculator.php>>.
- [66] Magnor, Marcus A., et al., eds. *Digital Representations of the Real World: How to Capture, Model, and Render Visual Reality*. CRC Press, 2015.
- [67] Svoboda, Tomáš, Hanspeter Hug, and Luc Van Gool. "ViRoom—low cost synchronized multicamera system and its self-calibration." *Pattern Recognition*. Springer Berlin Heidelberg, 2002. 515-522.
- [68] Rai, Piyush Kumar, et al. "A cost-effective multiple camera vision system using FireWire cameras and software synchronization." *Proceedings of the 10th International Conference on High Performance Computing, Hyderabad, India*. Vol. 1720. 2003.
- [69] Sousa, Ricardo M., et al. "Multi-camera synchronization core implemented on USB3 based FPGA platform." *IS&T/SPIE Electronic Imaging*. International Society for Optics and Photonics, 2015.

- [70] Pettoirelli, Nathalie, et al. "Using the satellite-derived NDVI to assess ecological responses to environmental change." *Trends in ecology & evolution* 20.9 (2005): 503-510.
- [71] Verrelst, J., et al. "Directional sensitivity analysis of vegetation indices from multi-angular Chris/PROBA data." ISPRS Commission VII Mid-term symposium. 2006.
- [72] Qi, J., et al. "Normalization of sun/view angle effects using spectral albedo-based vegetation indices." *Remote Sensing of Environment* 52.3 (1995): 207-217.
- [73] Qi, J., Y. Kerr, and A. Chehbouni. "External factor consideration in vegetation index development." *Proc. of Physical Measurements and Signatures in Remote Sensing, ISPRS* (1994): 723-730.
- [74] Jackson, Ray D., and Alfredo R. Huete. "Interpreting vegetation indices." *Preventive Veterinary Medicine* 11.3 (1991): 185-200.
- [75] Galvao, L. S., et al. "Sun and view angle effects on NDVI determination of land cover types in the Brazilian Amazon region with hyperspectral data." *International Journal of Remote Sensing* 25.10 (2004): 1861-1879.
- [76] Zhang, Jun, and Jinglu Hu. "Image segmentation based on 2D Otsu method with histogram analysis." *Computer Science and Software Engineering, 2008 International Conference on*. Vol. 6. IEEE, 2008.
- [77] "Correcting Nonuniform Illumination." MathWorks. The MathWorks, Inc. Web. 26 Nov. 2015. <<http://www.mathworks.com/help/images/examples/correcting-nonuniform-illumination.html?refresh=true>>.
- [78] Diaz, Christina. *Modification Of The Near-Infrared Signature Of Textile Fabrics Via Colloidal Self-Assembly*. Diss. 2009.